Princeton University

Department of
Mechanical and
Aerospace Engineering

ANNUAL STATUS REPORT

For the Period
1 April 1982 to 31 March 1983

NASA AMES RESEARCH CENTER GRANT NAG 2-109

AN EXPERIMENTAL STUDY OF THREE-DIMENSIONAL SHOCK WAVE/BOUNDARY LAYER INTERACTIONS GENERATED BY SHARP FINS

(Princeton University Report MAE 1584-T)

Author: Frank K. Lu
Principal Investigators: Gary S. Settles
Seymour M. Bogdonoff

Gas Dynamics Laboratory
Mechanical and Aerospace Engineering Department
Princeton University, Princeton, NJ 08544

March 1983

ACKNOWLEDGEMENTS

The author wishes to thank Professor S.M. Bogdonoff for his constant supervision and advice. Special thanks also go to Dr. G.S. Settles and Dr. D.S. Dolling for the numerous enlightening and useful discussions.

The author would also like to thank Bill Stokes, wind tunnel technician, who ably carried out a demanding task and to Bill Dix who made the models used in the experiments. The author is also grateful to the following for their help and cooperation: Bob Bogart, Dick Gilbert, Gary Katona and Sharon Matarese.

The research was sponsored by NASA under grant NAG 2109 monitored by Dr. C.C. Horstman.

This thesis carries No. 1584-T in the Records of the Department of Mechanical and Aerospace Engineering.

ABSTRACT

An experimental investigation of the interaction between a turbulent boundary layer and a shock wave generated by a sharp fin with leading edge sweepback was performed. The incoming flow was at Mach 2.96 and at a unit Reynolds number of 63×10^6 m^{-1}. The approximate incoming boundary layer thickness was either 4 mm or 17 mm. The fins used were at 5°, 9° and 15° incidence and had leading edge sweepback from 0° to 65°. The tests consisted of surface kerosene-lampblack streak visualization, surface pressure measurements, shock wave shape determination by shadowgraphs, and localized vapor-screen visualization. The upstream influence lengths of the fin interactions were correlated using viscous and inviscid flow parameters. The parameters affecting the surface features close to the fin and away from the fin were also identified. Essentially, the surface features in the farfield were found to be conical.

NOMENCLATURE

L_{incep}	length measured along the inviscid shock wave location on the test surface for inception of conical (or cylindrical) surface features
L_s	length measured along the inviscid shock wave on the test surface
L_u	upstream influence length measured from the inviscid shock wave location on the test surface in the freestream direction
L_{un}	upstream influence length measured from the inviscid shock wave location on the test surface normal to the shock wave
$(L_{un})_{incep}$	normal upstream influence length at the inception to conical symmetry
M, M_∞	incoming freestream Mach number
$M_n = M_\infty \sin \beta_o$	component of the incoming freestream Mach number normal to the inviscid shock wave location on the test surface
p, P	static pressure
p_o	stagnation pressure of the incoming flow
p_w	static pressure on the test surface
p_1, p_{FS}	static pressure of the incoming freestream flow
p_2/p_1	inviscid pressure rise across the shock wave
Re, Re_u	unit Reynolds number
$Re_{\delta_{av}}$	Reynolds number based on the average undisturbed boundary layer thickness through the interaction region
Re_{δ_o}	Reynolds number based on the incoming boundary layer thickness
x, y, z	Cartesian coordinate system for fins (see Figure 21) and delta wings (see Figure 20)

$x_s = x - y \cot \beta_o$	abscissa measured from the inviscid shock wave location on the test surface
α	fin or ramp angle of attack
α_f	fin angle measured perpendicular to the leading edge
α_f'	effective fin angle
α_r	ramp angle measured perpendicular to the leading edge
β_o	inviscid shock wave angle from the freestream direction on the test surface
$\hat{\beta}_o$	measured inviscid shock wave angle on the test surface
β_o'	inviscid shock wave angle as calculated from the perfect gas shock tables
δ	boundary layer thickness
δ_o, δ_1	boundary layer thickness at the beginning of the interaction
δ_{AV}	boundary layer thickness averaged over the free-stream extent of the interaction
δ_{local}	local boundary layer thickness
δ^*	boundary layer displacement thickness
$\Delta\alpha_f = (\alpha_f' - \alpha_f)$	difference between the effective fin angle of attack and the measured fin angle of attack
$\Delta\beta = (\beta_o - \beta_o')$	difference between the inviscid shock wave angle and the calculated inviscid shock wave angle
Δy	correction to the ordinate to locate the apparent origin for correlating quasi-conical surface flow features
θ	angle made between the y-axis and the shock wave on the test surface
λ	sweepback angle
λ_f	fin sweepback angle

λ_r	ramp sweepback angle
μ	Mach angle
ξ	streamwise direction measured from the nozzle throat of the wind tunnel
σ	angle made by the surface lampblack streaks with the freestream direction
ϕ	angle made by an inclined planar shock wave with the freestream direction

CONTENTS

FIGURES

Chapter 1

INTRODUCTION

The interaction of a shock wave with a boundary layer was first observed more than forty years ago. Subsequently, a large number of experiments have been done to study such an interaction. Examples of such interactions are those occurring at wing-fuselage junctions and deflected control surfaces of supersonic aircraft, those in supersonic engine inlets, and those on transonic wings and turbomachinery blades. These interactions can cause intense local heating and increased drag, or undesirable control and stability characteristics. Hence, these interactions need to be understood so that they can be predicted routinely and controlled. But there is yet no comprehensive theory to relate all aspects of the problem. The analytical methods and empirical rules that are available cannot even predict the interaction between a boundary layer and the shock wave generated by a simple geometry accurately. Therefore, research into shock wave boundary layer interactions is necessary for practical purposes and for understanding the underlying physical processes.

Shock wave boundary layer interactions are usually classified as two-dimensional and three-dimensional types in analytical and experimental studies although two-dimensional types can hardly be expected in reality. In experiments on two-dimensional interactions, the three-dimensional effects are found at the edges of the interact-

ion region. In instances encountered in aviation, three-dimensional effects occur at junctions or ends. An important exception to this is the shock wave interacting with the boundary layer on the upper surface of a transonic wing. In flowfield modeling, it is often assumed that a region exists between the root and the tip of the wing where the flowfield is two-dimensional in a plane normal to the leading edge.

1.1 TWO-DIMENSIONAL INTERACTIONS

More studies have been done on two-dimensional interactions than on three-dimensional ones and there is now a good understanding of the two-dimensional problem. Two-dimensional experiments have covered a wide range of parameters including the large Reynolds numbers approaching full-scale flight values. Recent experiments, making use of improved instrumentation techniques and data acquisition systems, have examined these interactions in detail and provided data to test analytical and numerical studies. The latest developments in analytical and numerical modeling have been reviewed recently by Adamson and Messiter (1980) and MacCormack and Lomax (1979).

Previous studies of two-dimensional interactions have identified some features which are relevant to the present study of a three-dimensional interaction. These features will now be discussed. In inviscid two-dimensional flow, an incident shock wave on a solid wall or a shock wave due to a disturbance on the wall produces a dis-

continuity in pressure at the surface. But in a viscous flow, the boundary layer interacts with the shock wave to spread out the pressure discontinuity. The wall static pressure starts to rise upstream of the theoretical location of the inviscid shock wave on the wall, eventually reaching the inviscid value some distance downstream of the shock wave location. The cause of the upstream effect is the self-sustaining interaction between the viscous layer close to the wall and the inviscid outer stream, according to Lighthill's theory (Lighthill (1953) and Stewartson and Williams (1969)).

The point upstream of the shock wave where the pressure rise is first detected is called the *upstream influence* of the shock wave. It is normally measured from the location of the shock wave at the wall assuming an inviscid flow. Since the interaction starts at the upstream influence, the upstream influence is an important quantity to be measured. The usual method of determining this is to find the intercept of the tangent to the maximum pressure gradient with the freestream pressure (Figure 1). The upstream influence can be determined from surface oil flow patterns as well. An oil flow pattern is formed when an oil-pigment mixture (such as kerosene-lampblack) which is painted on the test surface is driven by the wind tunnel flow. The upstream influence can be identified on the pattern as the first occurrence of disturbances from the interaction to the incoming oil flow.

By increasing the strength of the shock wave, the adverse pressure

gradient eventually causes the flow near the surface to stop. The boundary layer is then on the verge of *separation* when this happens and further increase of the shock wave strength causes the boundary layer to separate. A *separation bubble* is formed where the mean flow close to the surface is presumed to be reversed to the incoming freestream flow. Significant pressure losses and high heat transfer rates may occur in such a separated region. Therefore, there is practical interest in preventing separation. But prediction techniques which sometimes work well for attached flows cannot usually cope with separation. This is because, in general, the boundary layer equations are no longer valid in the region of the separation bubble since the assumptions in deriving these equations no longer apply.

There are many experimental techniques to detect incipient separation and the separation point. One that is commonly used is due to Kuehn (1959): separation occurs when a kink is observed in the surface static pressure distribution. An example is shown for a ramp at an incoming freestream Mach number, M_∞, of 2.95 in Figure 2 (Settles (1975)). With a small ramp angle (for example, 10^o), the shock wave was found to be weak and the boundary layer remained attached; the interaction region was small and localized. Using Kuehn's criterion, Settles found that incipient separation occurred when the ramp angle was between 15^o and 18^o. With larger ramp angles, for example, 20^o, the increased shock wave strength resulted in the formation of a separation bubble. There was then a kink in the surface pressure

distribution. Figure 2 also gives an indication of the effect of the shock wave strength on a two-dimensional interaction. Thus, the normalized upstream influence length, L_u/δ_o, had increased from $O(0.1)$ for a weak shock interaction to $O(1)$ for a strong shock interaction.

1.2 THREE-DIMENSIONAL INTERACTIONS

Compared with two-dimensional interactions, present knowledge of three-dimensional interactions is minimal. Only within the last decade were such studies performed in earnest. A difficulty in these studies is the variety of interactions that can occur in three-dimensional flow. Therefore, attempts to classify these interactions or to search systematically for the key parameters that govern them are difficult.

The lack of attention on three-dimensional interactions is not due to their unimportance but rather due to their supposed intractability. Most investigators pursued the traditional approach of first studying two-dimensional interactions under the presumption that an understanding of two-dimensional interactions must precede and will enhance the understanding of three-dimensional ones. Such attempts may be successful if the inviscid flowfield is geometrically degenerate, for example, if it is conical. In this case, the number of spatial dimensions is reduced from three to two so that the inviscid flowfield is two-dimensional.

An example of a three-dimensional interaction is one that is in-

duced by a sharp vertical fin (Oskam (1976)). Figure 3 shows the surface pressure distributions at a spanwise distance of 57 mm (2.25 in) from the apex of the fin for different fin angles of attack. Although the incoming freestream conditions were similar to those of the two-dimensional ramp experiments of Settles (1975), this pressure distribution differed from that of Figure 2. The normalized upstream influence length, L_u/δ, was approximately $O(10)$ and remained almost constant with increasing fin angle of attack (or, equivalently, with increasing shock strength). Dolling and Bogdonoff (1981) found that an appropriate scaling parameter for the upstream influence in such a swept interaction was the normal component of the incoming freestream Mach number to the freestream shock wave.* In addition, an important step in understanding three-dimensional interactions is the choice of a suitable coordinate system for plotting the data. Thus, Dolling and Bogdonoff measured the upstream influence normal to the inviscid shock wave extrapolated to the test surface.

1.2.1 Swept Shock Wave Boundary Layer Interactions

Three-dimensional interactions can be broadly divided into geometry-dominated interactions and non-geometry-dominated interactions. Examples of the former include those induced by blunt protuberances in supersonic flow and are not considered in the present study. Non-

*The freestream shock wave location could be either calculated from inviscid theory or determined experimentally by optical methods. For brevity, the shock wave determined by either of these methods will be called the *inviscid shock wave*.

geometry-dominated interactions have features which are affected by flow parameters only. An example is the interaction caused by a sharp fin in supersonic flow where the fin dimensions are large compared to a significant dimension of the interaction such as its boundary layer thickness. A non-geometry-dominated interaction will depend on, for instance, incoming Mach number, shock wave strength and orientation, Reynolds number and boundary layer thickness. The absence of geometrical parameters may afford some simplification to the non-geometry-dominated problem.

For some non-geometry-dominated interactions, the inviscid flow is conical in nature, that is, the flow properties are constant along a ray. The interaction region may also be conical so that the interaction grows with span (Green (1970)). Green distinguished, in addition, the possibility of cylindrical interactions. In this case, the interaction is affected by flow parameters normal to the inviscid shock wave only and the interaction remains constant along the span of the interaction. Further simplification in the theoretical analysis may then be possible.

1.3 SOME STUDIES OF SWEPT SHOCK WAVE INTERACTIONS

Some previous studies of the interaction between a swept shock wave and a turbulent boundary layer will now be discussed. These studies used geometries that induced inviscid flowfields which were either conical or cylindrical. A brief summary of the earlier, mostly exploratory

studies will be made followed by a detailed discussion of recent studies done at Princeton University.

Two points of caution need to be mentioned concerning the past studies. First, there was a tendency by some early investigators to infer the whole flowfield from the surface phenomena without a detailed flowfield exploration. For instance, based on the surface oil flow patterns of the shock wave boundary layer interaction caused by a sharp fin, Korkegi (1976) inferred that (depending on the fin angle of attack) one or two vortices existed in the interaction region. Since the basic physical processes of shock wave boundary layer interactions were, and still are, poorly understood, this was too general a conclusion to make.

Secondly, the documentation of flow conditions and wind tunnel interference was poor in some of these studies. The flow conditions must be stated precisely to enable comparisons to be made with other experiments under different conditions. Various claims of the nature of the interaction, be it conical or cylindrical, were suspect upon examining the data because of the limited width of the test section and the consequent tunnel wall interference. In particular, for fin-induced interactions, there were contradictory reports on whether the upstream influence or the entire interaction region grew with increasing distance measured along the inviscid shock wave location on the test surface. In some cases, the limited tunnel dimensions prevented the interaction region from developing sufficiently to deter-

mine if the interaction was conical or cylindrical.

Figure 4 summarizes some of the relevant details of three studies to illustrate this point. Stanbrook (1961) suggested that the interaction was still spreading at a spanwise distance of 10δ from the fin. But he also assumed (without evidence) that at further distances from the fin, the interaction approached a cylindrical form. McCabe (1966) found that the interaction tended towards cylindrical symmetry after 19δ along the shock. With the fin mounted at the centerline of a tunnel that was only 100 mm (4 in) or 28δ wide, tunnel wall interference had probably marred McCabe's results. Finally, Law's (1975) experiments with an incoming flow at Mach 5.9 showed that the interaction was conical as far as 30δ measured along the shock wave. Thus, based on these studies, no definite conclusions can be made on the farfield nature of the interaction.

An early study of a three-dimensional interaction was performed by Stanbrook (1961) who investigated interactions between a sharp fin-induced shock wave with a turbulent boundary layer at Mach numbers from 1.6 to 2.0. The experiments showed that there was a spanwise spread of the interaction and that, throughout most of the region, the interaction started further ahead of the freestream shock wave in contrast with a two-dimensional interaction with the same shock wave. The large upstream influence was assumed by Stanbrook to be partly due to disturbances propagating along the local Mach cones from the apex. These Mach cones became more obtuse close to the test surface as the

Mach number approached one. Therefore, the disturbances closest to the test surface would propagate more in the spanwise direction than those above. In addition, part of the cause was attributed to the propagation of disturbances within the subsonic portion of the boundary layer. Stanbrook noted that the interaction was three-dimensional up to 10δ from the shock generator. However, Stanbrook did not distinguish if the region studied was close to the fin where geometrical parameters were important or if the region was in the farfield where flow parameters were important. The distinction of a near field (geometry-dominated) and a farfield (non-geometry-dominated) is relevant in the study of three-dimensional interactions (Teng and Settles (1982)). From the surface oil flow, Stanbrook also found that when the freestream was deflected between 7.5° and 8°, the maximum deflection angle of the surface streak pattern was equal to the inviscid shock wave angle. Stanbrook defined this to be separation. At separation, the inviscid pressure ratio across the shock wave was found to be about 1.5.

Zubin and Ostapenko (1979) placed surface pressure tappings in arcs centered at the tip of a fin mounted vertically on a flat plate. The fin angles varied from 5° to 22.5°. At an incoming freestream Mach number of 2.95 and a unit Reynolds number of 0.16×10^{9} m^{-1} (4.0×10^{6}/in), the surface pressure along a ray from the apex was found to be constant except for a region near the apex. Zubin and Ostapenko considered that the size of the non-conical apex region depended on

the unit Reynolds number: with a large unit Reynolds number, this region was found to be small.

Zubin and Ostapenko also examined three-dimensional separation using Stanbrook's (1960) separation criterion. Separation was found to occur at a fin angle of attack of 6.5°. This was comparable to the value of 6° that McCabe (1963) obtained with an incoming flow at a Mach number of 2.96. At these angles, the inviscid pressure ratio across the shock wave was approximately 1.6. At larger fin angles (above 12.5°), a secondary separation line was observed which disappeared when the fin angle of attack reached 22.5°. Zubin and Ostapenko mentioned that this was also observed by Zheltovodov (1976) who, in addition, found that the secondary separation region reappeared at a higher strength (incoming Mach number = 3, fin angle of attack = 30°). At the moment, the features associated with the secondary separation line are not well understood.

Integral boundary layer methods, which assumed inviscid two-dimensional flow, have been formulated by Cousteix and Houdeville (1976) and Myring (1977) to analyze swept interactions. These authors assumed an inviscid two-dimensional flow to simplify the theoretical analysis. Integral methods are adequate as a means of characterizing the gross aspects of a boundary layer. The usual limitation of such methods is the lack of detail, especially when changes are occurring rapidly. On the other hand, they are simple and do not require the solution of a large set of equations.

In deriving the integral relationships, Cousteix and Houdeville (1976) assumed that the wall pressure distribution was determined beforehand by experiment. The continuity and momentum equations and a three-dimensional mixing length scheme (in which the effective turbulent stress was assumed to be in the same direction as the laminar stress) were used in the calculations. The coordinate system that was used for the momentum equations consisted of an axis in the shock wave direction and another in the freestream direction. Cousteix and Houdeville first verified their analysis with a two-dimensional interaction using experiments that they performed with an incident oblique shock wave at $M_\infty = 1.92$. Good agreement was found between the calculated and measured momentum thicknesses as long as the shock wave was not strong enough to cause (two-dimensional) separation. To apply the method to three-dimensional interactions, the derivatives parallel to the shock wave were assumed to be zero -- this is a two-dimensional assumption. Cousteix and Houdeville compared their three-dimensional analysis with experiments that they performed at $M_\infty = 2.3$ using a sharp fin as a shock generator. The predictions of the longitudinal and transverse momentum thicknesses and the form factor were good at small fin angles of attack, becoming worse when the angle of attack was 6°. At this angle, the flow was close to separating. Separation was defined as a convergence of surface streak lines in the surface oil flow patterns and not as an occurrence of a line of zero shear stress. Cousteix and Houdeville found that separation occurred when the fin

angle of attack was 7° at which angle the incoming Mach number normal to the freestream shock wave was 1.2.

In another study using integral methods, Myring (1977) analyzed the cylindrically symmetric interaction of an infinitely long swept shock wave with a boundary layer. A separation line was assumed to form which was parallel to the shock wave. The surface shear stress at the separation line was also assumed to be parallel to the shock wave. By taking advantage of the simplification afforded through the two-dimensional form of the interaction, Myring derived integral relations to predict the occurrence of separation. The analysis showed that, for interactions involving swept normal shocks, there was a relationship between the shock strength required to provoke separation and the shock sweep. Thus with a Mach 2 incoming flow, Myring agreed with the correlation proposed by Korkegi (1973) that separation occurred when the inviscid pressure rise through the shock wave was about 1.4. In other words, this was the same as the normal incoming freestream Mach number of 1.2 obtained by Cousteix and Houdeville.

At Princeton University, research is continuing on non-geometry-dominated interactions caused by swept ramps and fins. The original experiments of Settles (1975) using two-dimensional ramps were extended to include sweepback (Settles and Perkins (1980) and Settles *et al.* (1980 and 1981)). Settles *et al.*(1980) performed some preliminary studies on interactions at $M_{\infty} = 3$ using swept compression ramps. From surface flow visualization, the interaction region away from the up-

stream end of the corner was found to be cylindrical at small sweepback angles ($\lambda_r < 30^o$). Settles *et al.* (1980) also presented surface pressure distributions for a ramp with a streamwise compression angle of 16^o. The pressure distributions showed that the interaction was cylindrical for corners that were swept back less than 40^o. Settles and Perkins (1981) took additional surface pressure distributions of various swept ramps; some examples for a ramp at an angle of 24^o to the incoming freestream direction ($\alpha_r = 24^o$) are shown in Figure 5. The pressure distributions took on a different form (similar to that of three-dimensional interactions generated by fins) when the sweepback of the ramp increased. Thus, at a spanwise distance of 95 mm (3.75 in) from the tip of the ramp, the normalized upstream influence length, L_u/δ, was less than unity when the ramp was swept back from 0^o to 20^o. But $L_u/\delta \approx 3$ when the ramp was swept back to 60^o. These differences had been studied by Settles *et al.* (1980) who found that, away from the incipient region of the upstream edge of the ramp, either a cylindrical or a conical interaction region could arise depending on the ramp sweepback. Later experiments of Settles *et al.* (1981) were done with a boundary layer either 2.5 mm (0.1 in) or 15 mm (0.6 in) thick, and at two unit Reynolds numbers of 63×10^6 m^{-1} (1.7×10^6/in) and 187×10^6 m^{-1} (4.75×10^6/in). For fixed corner and sweepback angles (α_r and λ_r) and at a given incoming Mach number ($M_\infty = 3$), the upstream influence length measured from the leading edge of the ramp, L_u, was found to depend on the unit Reynolds number, Re, and the boundary layer

thickness, δ_o, only. In the first part of their study, Settles *et al.* found by dimensional analysis that for a two-dimensional interaction,

$$\frac{L_u \, Re^{1/3}}{\delta_o^{2/3}} = \text{const.} \quad \begin{matrix}\text{(two-dimensional;} \\ M_\infty \approx 3,\ \alpha_r \text{ fixed)}\end{matrix} \qquad \text{(1a)}$$

$$= 0.9 \exp\,(0.23\,\alpha_r). \qquad \text{(1b)}$$

They mentioned that the accuracy of this relation dropped with increasing α_r because the powers of Re and δ_o should not be constants in reality but should be weak functions of α_r. The values of the powers used were the averages obtained from experiments at Mach 3 and were not tested through a range of Mach numbers.

By similar dimensional arguments, Settles *et al.* found that for swept compression ramps,

$$\frac{L_u \, Re^{1/3}}{\delta_{local}^{2/3}} = f\left\{\frac{y\,Re^{1/3}}{\delta_{local}^{2/3}},\ \alpha_r,\ \lambda_r,\ M_\infty\right\} \qquad (2)$$

where y was the distance from the tip of the ramp in the spanwise direction. Since the interaction covered a large streamwise distance, the local undisturbed boundary layer thickness, δ_{local}, was used instead of a constant incoming undisturbed boundary layer thickness, δ. Equation (2) thus scaled the upstream influence length in both the streamwise and the spanwise directions for fixed α_r, λ_r and M_∞.

Prior to studies of interactions caused by swept ramps, Oskam

(1976) carried out extensive and detailed flowfield measurements of the three-dimensional interaction caused by sharp fins at $M_\infty = 3$. Oskam's study showed that the interaction extended for a large vertical distance measured from the test surface with the effects of viscosity confined close to the surface. Further, Oskam was unable to detect any vortices in his flowfield surveys. As mentioned previously, models based on the rolling up of a shear layer into one or more vortices had been proposed by some investigators. Based on his observations, Oskam concluded that most of the interaction region consisted of wave interference with only a thin layer of highly deflected secondary flow close to the wall. Oskam proposed, therefore, a flowfield model with four regions. The first region consisted of the incoming uniform flow and the two-dimensional boundary layer. The next region, which formed the major portion of the interaction, consisted of the upstream compression waves and the wave interaction with the oblique shock. This region was thought to be inviscid and rotational and to extend downstream of the oblique shock wave. The flow deflection in this region was not excessive with the deflection angle being less than the shock generator angle. The third region was relatively thin and closest to the wall; the flow here was deflected spanwise to angles above the shock generator angle resulting in a strong cross flow. Oskam found that viscosity was important in this region. Finally, the last region, which was above the main interaction, encompassed the weak waves generated by the inter-

action: this region then merged into the freestream flow.

Dolling and Bogdonoff (1981) considered shock sweepback, M_n, δ and Re effects on sharp fin interactions and devised a correlation scheme for the upstream influence lengths. The effect of the shock strength on the upstream influence was accounted for by using a coordinate system that changed with the sweepback of the shock wave and by measuring the upstream influence normal to the shock wave location, L_{un}. The upstream influence was assumed to be affected by the component of the pressure gradient normal to the shock wave. The correlation obtained by Dolling and Bogdonoff was

$$\frac{L_{un}}{M_n} = f(L_s), \tag{3}$$

where L_s was the distance measured along the inviscid shock wave location on the test surface from the apex of the fin. Equation (3) was used to correlate the upstream influence lengths of a large number of fins for an $M_\infty = 2.95$ incoming flow. But the correlation of Law's (1975) data at $M_\infty = 5.9$ was not good because there were insufficient data points at the upstream influence.

Besides sweepback and shock strength, Dolling and Bogdonoff also considered unit Reynolds number and boundary layer effects along the same lines as Settles *et al.* (1981). The upstream influence was correlated by

$$\frac{L_{un}\, Re^{1/3}}{\delta_{local}^{2/3}} = f\left\{\frac{L_s Re^{1/3}}{\delta_{local}^{2/3}}\right\}. \tag{4}$$

This correlation scheme was slightly different from that of Settles *et al.* Dolling and Bogdonoff measured L_{un} (the upstream influence normal to the shock wave location) instead of L_u (the upstream influence measured parallel to the x-axis), and L_s instead of y. These differences may not be significant at the small sweep angles (say, $\lambda_r < 30^o$) in the experiments of Settles *et al.* since at those angles, L_{un} and L_u were about the same, and so were L_s and y.

Although these schemes appeared to correlate the upstream influence data, some shortcomings need to be addressed if further efforts to relate the disparate swept interactions are to be undertaken. The upstream influence length used by Settles *et al.* (1981) was measured from the corner. This was suitable so long as the inviscid shock wave was attached. When this shock wave became detached, the upstream influence length measurements of Settles *et al.* could not be directly compared with the upstream influence lengths of other swept interactions because a portion of the measurements was then within the "downstream influence" of the shock wave. The upstream influence measurements have to be taken from the inviscid shock wave location as well and this has recently been done (Teng and Settles (1982)).

Limiting attention to cases where the inviscid solution yielded attached shock waves, the upstream influence data obtained by Settles *et al.* (1981) showed differences arising from the sweepback of the shock wave. The spanwise growth of the upstream influence for highly swept interactions (e.g., that due to an $\alpha_r = 10^o$, $\lambda_r = 50^o$ ramp) was

large and there was a tendency towards conical symmetry. On the other hand, the upstream influence data from less swept interactions showed a tendency towards cylindrical symmetry. These differences are also discussed by Teng and Settles (1982).

1.4 FEATURES IN THE SURFACE FLOW

Since the present study uses surface flow visualization, some of the features that have been observed in the surface flow will now be mentioned. As an illustration, Figure 6 is a sketch of the pattern due to the interaction of a turbulent boundary layer with a shock wave generated by a sharp fin of relatively large, say, 15^{o}, angle of attack. The upstream influence line marks the first disturbance to the incoming two-dimensional surface flow. The surface flow is then swept away from the fin and appears to converge at a line. In the literature, this is called the separation line; note that this is unlike the definition for a two-dimensional separation since it is not known if the surface shear stress is zero along this line. Feather-like lines appear in the surface flow downstream of the separation line and closer towards the fin, there is a faint delineation which is often called the reattachment line. For this interaction, a line (commonly called the secondary separation line) occurs in the region downstream of the first separation line. The secondary separation line is usually not found at smaller fin angles of attack. Besides, in a turbulent interaction, a secondary reattachment line is normally

not seen although it is visible in a laminar one (Cooper and Hankey (1974) and Zubin and Ostapenko (1979)). According to Korkegi (1976) and Zubin and Ostapenko (1979), the secondary reattachment line is close to the secondary separation line. Although these "separated" regions are seen in surface flow visualization, not much is known at present of their nature.

1.3 SCOPE OF THE PRESENT INVESTIGATION

The present investigation is an experimental study of the interaction between a shock wave generated by a sharp fin with leading edge sweepback and a turbulent boundary layer. In the case of supersonic flow past a fin of theoretically infinite height with leading edge sweepback, attached, inviscid, planar shock waves can exist for certain fin angles of attack (Figure 7a). Figure 7a shows that such a shock wave can be located using two angles, the sweepback angle, θ, measured from the y-axis, and the tiltback angle, ϕ, measured from the x-axis. In some instances, the same shock wave orientation can be obtained with a swept ramp of theoretically infinite span (Figure 7b). The planar shock wave orientations of either fins or ramps can be obtained from two-dimensional theory and the results of these calculations are shown in Figure 8 for an incoming flow at Mach 2.95. The figure shows how θ and ϕ change when a fin at a given angle of attack, α_f, has its leading edge swept back. Detached shock waves (which are curved) cannot be plotted in this figure. The figure also shows how θ and ϕ change

when the leading edge of a ramp at a fixed angle of attack, α_r, is swept back. By attaching a fin with leading edge sweepback to a flat plate (Figure 9), the mass continuity condition on the plate requires that the inviscid shock wave curves and impinges perpendicularly at the surface. For the moment this is ignored and it is simply assumed that the planar shock in the two-dimensional region can be extrapolated to the flat plate. Eventually, a better determination of the shock wave location on the flat plate will be necessary since this location is important in constructing an appropriate coordinate system (McCabe (1963), Peake (1975) and Dolling and Bogdonoff (1981)): Figure 8 is used only as a guide for the present investigation.

The present study builds on the recent work at Princeton University on swept interactions by examining a region in Figure 8 that was scarcely studied. The aims are:

1. Extend the study of the interaction between a turbulent boundary layer and a fin-generated shock wave by covering the range $50^\circ < \theta < 70^\circ$ and $20^\circ < \phi < 90^\circ$ (shown in solid lines in Figure 8). The study includes a determination of the inviscid shock wave location, the use of the upstream influence correlation of Dolling and Bogdonoff (1981), and a study of the surface phenomena through surface flow visualization and surface pressure measurements.
2. Conduct a preliminary investigation of the scaling of the upstream influence of sharp fin interactions and the upstream

influence of swept ramp interactions in the range $\theta_f = \theta_r$, $\phi_f = \phi_r$ (shown shaded in Figure 8). With the same incoming boundary layer, freestream and farfield conditions, the only differences are the local orientation of the shock wave at the test surface and the geometry of the fin and the ramp.

Chapter 2

EXPERIMENTAL METHODS

2.1 PROCEDURE

The present study was done with the same incoming conditions as those of Settles (1975), Oskam (1976), Settles and Perkins (1981), Settles *et al.* (1980 and 1981) and Dolling and Bogdonoff (1981). Thus it coincided with the parametric ranges that these authors considered. The procedure that was followed by the present study is summarized in Figure 10. The present study examined some of the surface phenomena of the interaction and the effect that sweeping back the fin leading edge had on the interaction. Incorporated were some of Oskam's suggestions, such as the use of a large interaction region (spanwise distance greater than 30δ) and the use of tracer injection into the interaction to examine the flowfield structure. A surface flow visualization was done first since this enabled the main features of the surface flow to be revealed conveniently. The shock wave location on the flat surface assuming an inviscid flow was determined next in order to construct the coordinate system used by Dolling and Bogdonoff (1981). To locate the shock wave, delta wings with half planforms similar to the fins and at the same angles of attack were placed in the same incoming flow. From the shadowgraphs obtained for each wing, the shape of the shock wave envelope from the plane of symmetry of the wing to one of the wing tips could be determined. The

shock wave envelope at the plane of symmetry of the wing will be called the *centerline shock wave* for short. The part of the shock wave envelope around a wing from the plane of symmetry to one of the wing tips was presumed to be similar to that around a fin (of similar half planform as the wing) mounted on a flat surface assuming that the boundary layer on the surface was absent. Pressure measurements provided additional information on the interaction and were also used for comparison with some of the features found in surface flow visualization. Finally, optical studies of the shock wave boundary layer interaction using vapor injection gave information on the interaction above the test surface. Although of a qualitative nature, these final studies nevertheless furnished insight into the behavior of a boundary layer interacting with a swept shock wave.

2.2 APPARATUS AND EQUIPMENT

2.2.1 Wind Tunnel and Test Section

The experiments were done in the high Reynolds number supersonic blowdown tunnel at the Gas Dynamics Laboratory of Princeton University. Tanks with a total capacity of 56.6 m^3 (2,000 ft^3) stored dried air at pressures up to 22 MN m^{-2} (3,200 psia). The stagnation pressure of the air entering the wind tunnel could be adjusted by a regulator from 0.4 MN m^{-2} (60 psia) to 3.4 MN m^{-2} (500 psia). A supersonic nozzle accelerated the air from the settling chamber upstream of the nozzle to a nominal value of Mach 2.95 in the test section which was just down-

stream of the nozzle. The air was then exhausted from the rear to the atmosphere. The test section, 0.2 m (8 in) square and 0.9 m (35.5 in) long, had two 230 mm (9 in) diameter windows in the walls for observation. There were also locations in the ceiling and the floor to accommodate instruments and the test model. A sting mechanism from the rear of the tunnel was used for mounting the fins. For a more detailed description of the wind tunnel, see the report by Vas and Bogdonoff (1971).

2.2.2 Fin Configurations

A number of sharp fins with 9° vertex angles were made out of 12.7 mm (0.5 in) thick aluminum plate. These fins had different leading edge sweepback angles, λ_f, from 0° to 65°. The lengths of the fins, l, were either 305 mm (12 in) or 254 mm (10 in), and the heights, h, were either 127 mm (5 in) or 100 mm (4 in) (Figure 11). These dimensions ensured that a large interaction region ($y/\delta > 30$) could be obtained without the tunnel stalling. Each of the fins could be connected to the sting from the rear of the wind tunnel by an adapter. Three adapters were available to set the angle of attack of the fin, α_f, at 5°, 9° or 15°. This fin-adapter arrangement allowed the fins and the adapters to be changed quickly. Some of the fins and adapters used are shown in Figure 12.

Figure 13 is a schematic view of a fin mounted on a flat plate. The fin and adapter could be cranked backward so that the kerosene-lampblack traces could be lifted off the test surface by transparent

adhesive tape easily. Since accurate measurements had to be taken from these traces, an airtight seal to prevent leakage between the fin and the test surface must be formed. The seal was obtained by applying glue at the location of the fin on the test surface before the fin was cranked into position.

Care was taken to ensure that the apex of the fin was always at the same spot in order that the incoming undisturbed boundary layer conditions were the same for every test. That spot was 230 mm (9 in) from the leading edge of the flat plate and 20 mm (0.75 in) from the sidewall of the tunnel and was sufficiently far from the sidewall boundary layer. In experiments done with the floor boundary layer, the apex of the fin was also 20 mm from the sidewall of the tunnel. Its streamwise location was referred to a known reference spot on the tunnel floor which was either 1.19 m (47 in) or 1.5 m (59 in) from the nozzle throat. Since the fins were all shorter than the tunnel height, each fin had a bolt on top which was tightened against the tunnel ceiling once the fin was in position. This ensured a tight seal at the base and also reduced vibrations. At $\alpha_f = 15^o$, the aerodynamic force was able to deflect the fin but this was prevented by a brass rod driven from the sidewall.

2.2.3 Test Conditions

The incoming freestream flow at the test section was nominally at Mach 2.95 and had a stagnation temperature which, depending on the ambient

temperature, varied from 250 K (450° R) to 270 K (485° R). The experiments were mostly done at a stagnation pressure of 0.69 MN m^{-2} (100 psia) which corresponded to a unit Reynolds number of 63 x 10^6 m^{-1} (1.7 x 10^6 /in). Some experiments were also done at a stagnation pressure of 2.07 MN m^{-2} (300 psia) which corresponded to a unit Reynolds number of 187 x 10^6 m^{-1} (5.05 x 10^6 /in). All tests were made under approximately adiabatic wall conditions. Typically, each run lasted less than one minute.

The experiments were done either on a flat plate or on the tunnel floor. The boundary layers over these test surfaces were surveyed by Settles (1975) and Oskam (1976). The undisturbed boundary layer on the flat plate at the fin location was considered by these authors to have a fully developed turbulent profile from fitting the velocity profile by the modified wall-wake similarity law of Sun and Childs (1973). The local boundary layer thickness was obtained by a curve-fit through the measured boundary layer thicknesses at different streamwise stations. For an incoming flow with a unit Reynolds number of 63 x 10^6 m^{-1},

$$\delta_{local} = 0.0512\ (228.6 + x)^{0.787} \qquad (5)$$

where δ_{local} and x were in mm. The velocity profile of the boundary layer on the tunnel floor at the test section also obeyed the wall-wake law of Sun and Childs. Again, curvefits through the measured boundary layer thicknesses were made to obtain δ_{local}. For an incoming flow with a unit Reynolds number of 63 x 10^6 m^{-1},

$$\delta_{local} = 0.0688\ (\xi - 305)^{0.796} \qquad (6)$$

where δ_{local} was in mm and ξ was the streamwise distance, in mm, measured from the nozzle throat of the wind tunnel. For an incoming flow with a unit Reynolds number of $187 \times 10^6\ m^{-1}$,

$$\delta_{local} = 0.0305\ \xi^{0.87} \qquad (7)$$

where δ_{local} and ξ were also in mm.

2.2.4 Delta Wing Configurations

The inviscid shock wave location is a reference line not only for two-dimensional interactions but for swept interactions as well (McCabe (1966), Peake (1975) and Dolling and Bogdonoff (1981)). In the present study, the shock wave location of the fin was determined from shadowgraphs of the shock wave formed on the windward side of delta wings at incidence. Each of the wings used had a span of 127 mm (5 in) and a length of 152 mm (6 in) so that the half planform was similar to the fins. Five sweepback angles of 0°, 20°, 40°, 55° and 65° were chosen to match the range of sweepback angles in the main experiment. Figure 14 is a photograph of a delta wing with a 40° leading edge sweep and a 15° incidence. The photograph shows how the wings were mounted in the wind tunnel. Each wing was mounted through an adapter on a vertical support in the same test section as the main experiment. The angle of attack of the wing could be changed by changing the adapter giving angles of attack of 5°, 9° and 15°.

One of the leading edges of every wing had twelve notches 0.8 mm

(1/32 in) deep spaced 4.76 mm (3/16 in) apart spanwise. These notches created wavelets which could be clearly seen in a shadowgraph. From the wavelets, the curved shock wave envelope could be traced.

2.3 EXPERIMENTAL MEASUREMENTS

2.3.1 Shock Wave Location

To obtain the shadowgraphs of the shock wave envelope around a delta wing, an optical system was set up which consisted of an intense spark source at the focus of a concave mirror. The beam of light from the mirror then passed through the windows of the test section to expose a sheet of photographic film on the other side. The light beam was adjusted to be perpendicular to the windows in order that the shadow of the model was of the same shape as the model itself.

Figure 15 is a sketch showing how light rays propagated through the test section when the tunnel was in operation; the view is along the upper surface of the wing towards the trailing edge. A ray such as Ray A, away from the shock wave envelope and through a uniform density field, would propagate in a straight line. The ray which was closest to the shock wave envelope and which just succeeded in propagating through in a straight line was Ray B. Within the shock wave envelope, the density of the flow (and thus the refractive index) decreased towards the wing surface. Consequently, light rays propagating through this nonuniform density field were refracted. For example, Rays C and D -- slightly nearer towards the wing surface than Ray B -- were

ORIGINAL PAGE IS
OF POOR QUALITY

refracted through the nonuniform density field which resulted in their being deflected towards the wing surface as they emerged through the shock wave envelope. The refracted light rays were recorded on photographic film as a dark line followed by a bright line because of the different amounts by which these rays were deflected. The different amounts of deflection, which meant that Rays C and D were no longer parallel after emerging from the shock wave envelope, resulted in a displacement of the dark and bright lines from the true position of the shock. Therefore, the thicknesses of the dark and bright lines depended on the location of the photographic film and could not be used to determine the centerline shock wave location. Only Ray B (which just skimmed the shock wave envelope at its centerline) would pass through parallel and unrefracted to mark the true location of the centerline shock wave.

Closer to the wing surface, Ray E propagated through the nonuniform density field but did not undergo any overall deflection. Next, Ray F was the ray furthest from the surface that just underwent refraction. Any ray closer to the wing surface, such as Ray G, would reflect off the surface. Since the surface was not a perfect reflector, the reflection was diffused. The net effect of the refraction of the light rays close to the wing surface was a displacement of the apparent surface towards the light beam. To locate the true surface of the delta wing, a shadowgraph of the test section without the wind tunnel running had to be taken for each of the wings tested. The true surface was then marked on the corresponding shadowgraphs obtained with the tunnel running.

2.3.2 Surface Oil Flow Patterns

The kerosene-lampblack surface flow visualization technique that was used in the present study evolved from studies by Settles (1975). This technique is particularly suited for supersonic flow because the kerosene vaporizes rapidly leaving only dried lampblack deposits. Hence, there is no smearing of the pattern when the tunnel is shut down. A 4:1 mixture of kerosene-lampblack was used in the present study to obtain the surface flow patterns. A thin coat was applied in a swath ahead of the fin and along its base. When the tunnel was started, the mixture was driven downstream and dark streaks of lampblack were deposited on the test surface. After the tunnel was stopped, the surface flow pattern was removed by using a large piece of transparent adhesive tape. Full-sized images could, therefore, be obtained in this manner.

The surface streak pattern provided a convenient way of determining the size of the interaction region and of locating features of interest. By choosing lampblack streaks that were not broken up as they curved past the fin, measurements were made of the upstream influence. The upstream influence was determined to be the location of the first detectable deflection of the lampblack streaks due to the interaction. Also measured was the surface streak deflection angle from the incoming free-stream direction, σ.

2.3.3 Surface Pressure Distributions

The floor section used by Oskam (1976) for surface pressure measurements was used in the present study as well. The present surface pressure distributions were taken parallel to the incoming freestream direction from upstream of the interaction rearwards for all fins except those with 65° sweepback. Pressure taps were located at three spanwise distances from the apex: 31.8 mm (1.25 in), 57.2 mm (2.25 in) and 82.6 mm (3.25 in).

The data were recorded automatically by a computerized system. Two 48-port Model 48J4 Scanivalves read the pressures alternately with each Scanivalve reading at a rate of four readings a second. Druck Model PDCR 22 strain gauge transducers converted these pressure readings into electrical signals which were digitized by a Preston GMAD-4 analog-digital converter and then stored in a HP-1000 minicomputer for further analysis. When the surface pressures were being read, the total pressure and the total temperature in the settling chamber of the wind tunnel were also recorded. These were measured each time the pair of Scanivalves was stepped.

2.3.4 Optical Studies Using Vapor Injection

Flow visualization using an acetone vapor tracer was done with fins mounted on the floor. For these studies, the fin surfaces were painted matt black to reduce reflections. Acetone was introduced either through a tube near the apex of the fin or through a static pressure

tap upstream of the interaction (Figure 16). The tube passed through a hole of 3.2 mm (1/8 in) diameter just to the rear of the apex of the fin and protruded only slightly from the fin surface to minimize disturbances to the interaction. To determine the effect of the acetone tube, kerosene-lampblack traces of the interaction were obtained for fins without sweepback at $\alpha_f = 5^o$, 9^o and 15^o. In all cases, the disturbances from the tube were confined to a distance of less than 25 mm (1 in) outboard from the fin. When the tap on the floor was used, it was usually at the centerline of the tunnel. But for tests with the $\alpha_f = 5^o$, $\lambda_f = 0^o$ fin, this tap (which was offset 19 mm (0.75 in) from the center of a 50 mm (2 in) diameter plug) was rotated so as to be closer to the fin. This was done to ensure that the interaction of the acetone-filled incoming boundary layer and the shock wave occurred within view. The acetone was sucked into the wind tunnel naturally from a bottle opened to the atmosphere because the static pressure in the test section during a run was lower than atmospheric. The acetone flow rate was controlled by a manually operated valve to achieve optimum seeding of the boundary layer. As the acetone entered the wind tunnel, it was vaporized because its saturation vapor pressure was near the static pressure.

The light sources used were a light sheet and a stroboscope (Figure 16). The light sheet, which was about 2 mm (0.1 in) thick, was obtained by refracting a pencil of light from an argon-ion laser through a cylindrical lens on the ceiling of the wind tunnel. The light sheet

was parallel to the freestream direction and could be shifted in the spanwise direction. It extended 150 mm (6 in), from upstream of the interaction region rearwards, to cover the region of interest. Usually, the light sheet was beamed 25 mm (1 in) away from the tunnel centerline and away from the fin. The stroboscope, which was the other light source, aided in the visual inspection of the flow and provided adequate illumination of the whole flowfield for stereo photography. The light from the stroboscope was shone into the test section from one of the windows of the wind tunnel.

The photographs were usually made on Polaroid High Speed film. When the laser sheet was used, the camera was aligned just above the floor and focused upon the light sheet with minimum depth of field to examine the "local" interaction. But when stroboscopic lighting was used, stereo photographs were taken with as large a depth of field as possible to record information on the whole interaction region.

2.4 ACCURACY

2.4.1 Equipment Accuracies

The fin angle of attack, α_f, was determined by adapters machined to the prerequisite angles. The leading edge sweepback, λ_f, was also machined precisely. The tolerance for both these angles was $\pm 0.1^{\circ}$. Similarly, the sweepback angles of the delta wings and the angles of incidence of their adapters were machined to $\pm 0.1^{\circ}$ tolerance.

The transducers and the thermocouple were calibrated at the start of

the daily test program. A Pace strain-gauge transducer was used to measure the stagnation pressure. This transducer was calibrated by a Heise pressure gauge which was accurate to 0.2 percent of 3.45 MN m^{-2} (500 psia) full-scale deflection. The transducers measuring the static pressures were calibrated by a Wallace and Tiernan pressure gauge which was accurate to 0.1 percent of 0.24 MN m^{-2} (35 psia) full-scale deflection. The chromel-alumel thermocouple was calibrated by feeding voltages corresponding to temperatures into a high-impedance Datel linear amplifier. The voltage-temperature correlation had been determined from tables issued by the U.S. National Bureau of Standards for chromel-alumel junctions. The calibrations were done through an automated data acquisition system and the calibration constants were stored in a computer. These constants were not determined for the full range of the transducers but were generally determined for ranges larger than those expected in the experiments. Thus, the static pressure transducers were calibrated from 13.8 kN m^{-2} (2 psia) to 166 kN m^{-2} (24 psia) with an rms error of less than one percent. The stagnation pressure transducer was calibrated from 0.55 MN m^{-2} (80 psia) to 0.83 MN m^{-2} (120 psia) with an rms error of less than one percent as well. Although the stagnation pressure transducer was not calibrated to 2.07 MN m^{-2} (300 psia), it measured that pressure with an rms error of less than one percent. The thermocouple was calibrated from 230 K (414° R) to 290 K (522° R) with an rms error of 0.2 percent.

2.4.2 Measurement Accuracies

The freestream Mach number of the flow was calculated using the isentropic perfect gas relationships for a compressible gas. An rms error estimate was made as well (Holman (1978)). For an incoming flow at a stagnation pressure of 0.69 MN m^{-2} (100 psia), M_∞ = 2.95 ± 0.5 percent whilst at a stagnation pressure of 2.07 MN m^{-2} (300 psia), M_∞ = 2.96 ± 0.5 percent. The Mach number in this study was therefore taken to be M_∞ = 2.95 with an error of one percent. The error of the computed value of the Mach number normal to the direction of the inviscid shock wave on the test surface,

$$M_n = M_\infty \sin \beta_o, \qquad (8)$$

was estimated to be 1.7 percent. The average stagnation temperature was measured as 260 ± 0.5 K and the static temperature was calculated to be 95 ± 0.6 K. The unit Reynolds number was then calculated knowing the properties of air at the static temperature and the incoming freestream Mach number. At p_o = 0.69 MN m^{-2}, Re = 63.6 x 10^6 m^{-1} ± 1.2 percent and at p_o = 2.07 MN m^{-2}, Re = 189 x 10^6 m^{-1} ± 1.6 percent.

The centerline of the shock wave envelope was examined by looking at the negatives of the shadowgraphs in a comparator. In all cases, the centerline was found to be straight barring small "wiggles" that could be attributed to weak disturbances from the ceiling of the tunnel. The angle made by the centerline shock wave with the freestream, $\hat{\beta}_o$, was estimated by trigonometry (from the negatives of the shadowgraphs) to an accuracy of ± 0.1° when α_f = 5° and α_f = 9°, and ± 0.2° when α_f =

15^{o}, corresponding to a fractional error of half a percent. The values of $\hat{\beta}_o$ are plotted in Figure 17. This figure shows a least squares fit through the estimated points at each of the three angles of attack. The curve-fit values of the centerline shock wave are called β_o. Interpolation gave the centerline shock angle for wings that were not tested. In Figure 18 is a summary of the estimated and the interpolated data. The maximum difference between $\hat{\beta}_o$ and β_o for the cases where actual tests were made was found to be one half percent. Since this difference was small, for consistency, only the curve fitted data were used in the main experiments. In addition, for the fins without sweepback (that is, $\lambda_f = 0^{o}$), the perfect gas shock tables gave calculated values of the shock wave angle, β_o'. Figure 18 shows that β_o is larger than β_o' by about one percent ($\Delta\beta/\beta_o' \simeq O(0.01)$). The slightly larger estimated values could be attributed to the boundary layer displacement, so that the flow was actually turning through an angle larger than that obtained assuming an inviscid flow. For example, at $\alpha_f = 15^{o}$, $\lambda_f = 0^{o}$, experiment gave $\beta_o = 33.1^{o}$ while inviscid theory gave $\beta_o' = 32.62^{o}$. In other words, $\beta_o = 33.1^{o}$ would correspond to a value of $\alpha_f = 15.46^{o}$ from inviscid theory, giving a boundary layer correction of 0.46^{o} when α_f was nominally 15^{o}.

The boundary layer correction for α_f of the fins should be approximately the same as that for the wings. But the correction was not made because β_o and not α_f was important in the analysis. An accurate estimate of β_o was necessary whereas only nominal values of α_f sufficed.

Thus, for the fin-generated shock waves, the inviscid shock wave angles from the freestream direction on the test surface were taken to be the same as β_o listed in Figure 18.

The deflection of the lampblack streaks from the incoming flow direction, σ, and the upstream influence were measured from the kerosene-lampblack traces. The streak deflection angle was measured by protractor to an accuracy of $\pm 0.5^{\circ}$. The upstream influence was determined visually and a curve was fitted through the data points. The upstream influence was then recorded in (x, y) coordinates. The scatter of the measurements about the curve-fit gave an estimate of the error. This error depended greatly on the curvature of the lampblack streaks. At the smallest fin angle ($\alpha_f = 5^{\circ}$), the curvature of these streaks decreased as the leading edge of the fin was swept back making the upstream influence measurement difficult. The resolution improved when the kerosene-lampblack traces obtained with fins at larger angles of attack were used. Similar problems beset the upstream influence measurement using surface pressure distributions because, when the shock strength was small, the initial pressure rise was gentle. This made it difficult to locate the tangent to the pressure gradient. By either method of determining the upstream influence, at $\alpha_f = 5^{\circ}$, the measurements of x and y had a six percent error. At $\alpha_f = 15^{\circ}$, this error decreased to two percent. Also, and especially for the $\alpha_f = 5^{\circ}$ fins, data toward the rear of the interaction region were difficult to measure and were not taken.

From the above angular and length measurements, some other lengths

were calculated (Section 3.2). The accuracies of these calculated lengths were estimated by an error analysis as follows:

1. x_s -- ± 0.2 mm at $\alpha_f = 15^o$ and ± 0.3 mm at $\alpha_f = 5^o$; and
2. L_u, L_{un} and L_s -- ± 0.1 mm throughout the range of β_o.

Chapter 3

DISCUSSION AND ANALYSIS

3.1 SHOCK WAVE ENVELOPE

In examples of shadowgraphs obtained of the flow past delta wings (Figure 19), the centerline shock wave could be seen as a bold black line followed by a white line. The wavelets caused by notches appeared as fainter lines since the notches were weaker disturbances. Each notch, in fact, caused a pair of dark and bright lines. One pair of dark and bright lines originated from the front of the notch and the other from the rear. The upstream edge of the dark line of the wavelet thrown off from the front of the notch was the true location of the shock wave envelope and was used to locate it. The cross section, normal to the wing surface, of the shock wave envelope is plotted in Figure 20. All distances are normalized by the semispan of the wing. This flow visualization could not be performed when the leading edges of the wing were subsonic. The only such case in these experiments was $\alpha_f = 15^\circ$, $\lambda_f = 65^\circ$.

At $\alpha_f = 5^\circ$ and $\lambda_f = 20^\circ$ (Figure 20a.i.), the shock wave envelope arched gently over the delta wing and reached a maximum of 0.13s, where s is the semispan of the delta wing. This shock wave envelope was shallow near the centerline, being closely parallel to the wing surface. In normalized coordinates, sweeping back the leading edge resulted in the shock wave envelope becoming progressively fuller. Thus,

at $\alpha_f = 5^o$, $\lambda_f = 65^o$, the shock wave envelope at the centerline was at a normalized distance, y/s, of 0.64 above the surface. Physically, of course, the shock wave would be closer to the fin as the sweepback increased (Figure 17). The present plots in normalized coordinates (Figure 20a) can be interpreted to mean that the shock wave envelope took on a more "conical" form as the fin became more swept back.

The same changes of the shock wave envelope with changes in λ_f when $\alpha_f = 9^o$ and $\alpha_f = 15^o$ were also observed (Figures 20b and 20c). On the other hand, at a fixed λ_f, the envelope became more arched at smaller α_f. This was because the reduction of α_f by a factor of three (from 15^o to 5^o) did not result in a corresponding decrease of $(\beta_o - \mu)$. In fact, the decrease of this difference was about 3.4 times (from 13.6^o to 4.1^o). In normalized coordinates, this means that the shock wave envelope became closer to the wing surface with increasing α_f. The significance of these changes in attempting to construct a coordinate system for the main study will be discussed next.

3.2 COORDINATE SYSTEM

Figure 21 shows the coordinate system that were used in the discussion. Data were recorded in a three-dimensional (x, y, z) Cartesian coordinate system with its origin at the apex of the fin. Some measurements, such as surface static pressure, were taken from the inviscid shock wave location on the flat surface parallel to the upstream flow direction. The abscissa was then x_s, where

$$x_s = x - y \cot \beta_o. \qquad (9)$$

Figure 21 also shows an intrinsic system that Dolling and Bogdonoff (1981) used to correlate upstream influence data. The upstream influence length normal to the inviscid shock wave location on the test surface, L_{un}, was measured at a distance L_s along the shock wave from the fin apex. Another upstream influence length, L_u, was measured in the incoming freestream direction from the shock wave location. This intrinsic coordinate system correlated the upstream influence data of Dolling and Bogdonoff because, by taking into account of the changes of the shock wave location, the number of parameters was reduced. Thus, the inviscid shock wave orientation was relevant but not the shock generator angle. To use the intrinsic system of Dolling and Bogdonoff in the present study, the raw upstream influence data were transformed by the following equations:

$$\begin{aligned} L_s &= x \cos \beta_o + y \sin \beta_o, \\ L_u &= x - y \cot \beta_o, \\ L_{un} &= - x \sin \beta_o + y \cos \beta_o. \end{aligned} \qquad (10)$$

3.3 SURFACE KEROSENE-LAMPBLACK PATTERNS

3.3.1 Description

Examples of the kerosene-lampblack patterns on the flat plate are shown in Figure 22 while other examples of the kerosene-lampblack patterns on the tunnel floor are shown in Figure 23. The size of the interaction on the test surface was about $x = 200$ mm (10 in) and $y = 150$ mm (6 in).

The overall size of the interaction (normalized by an avarage boundary layer thickness) was larger than those in the experiments of Oskam (1976) or Dolling and Bogdonoff (1981) as can be seen in Figure 24. Thus, this study could be used to determine if some of the observations of those investigators were also valid in an interaction region that extended further from the fin in non-dimensional terms.

Some spurious details (for example, pressure taps and sealed plugs) from past experiments could be seen in the kerosene-lampblack patterns (Figures 22 and 23). The effects of these details seemed localized and did not affect the interpretation of the surface flow patterns. The main features seen in these patterns will now be discussed using those formed on the flat plate as primary examples. Since the patterns formed on the tunnel floor were qualitatively similar, only important differences will be highlighted.

Figure 22a shows the streak pattern obtained with an $\alpha_f = 5^\circ$, $\lambda_f = 40^\circ$ fin. The streaks approached the interaction region parallel to the x-direction but became deflected laterally from the fin within the interaction region. The first detectable deflection -- the upstream influence -- was a key feature that could be identified.

In the streak pattern obtained with an $\alpha_f = 9^\circ$, $\lambda_f = 10^\circ$ fin (Figure 22b), another feature, called the separation line, could be seen downstream of the upstream influence. While performing the experiment, the surface flow upstream of the separation line was observed to approach that line before being swept away laterally. Similarly, the kerosene-

lampblack mixture painted at the base of the fin was swept laterally to form a pattern bounded upstream by the separation line. In effect, therefore, the separation line separated the limiting surface flow. But whether the incoming boundary layer was separated in the conventional (two-dimensional) sense is still a subject of current study. Closer to the fin, a faint delineation between the parallel flow close to the fin and the featherlike pattern in the interaction region could be seen. This is commonly called the reattachment line.

Figure 22c shows the streak pattern obtained with an $\alpha_f = 15^\circ$, $\lambda_f = 10^\circ$ fin. Under a stronger and less swept shock wave than the previous example, the interaction region was less swept and the lampblack streaks stood out more distinctly. Other than the features mentioned previously, another line (commonly called the secondary separation line) could be seen between the (primary) separation line and the reattachment line.

The same overall features as those obtained on the flat plate could be seen in the patterns obtained on the tunnel floor. Figure 23a shows the pattern obtained with an $\alpha_f = 5^\circ$, $\lambda_f = 30^\circ$ fin. The incoming streaks could be seen to deflect gently to angles below the angle of the inviscid shock wave on the test surface. An important feature of this pattern was the upstream influence. Next, in the streak pattern obtained with an $\alpha_f = 9^\circ$, $\lambda_f = 0^\circ$ fin (Figure 23b), the streaks were deflected above the shock wave angle so that in addition to the upstream influence, a prominent separation line was formed. Finally, Figure 23c shows the streak pattern obtained using an $\alpha_f = 15^\circ$, $\lambda_f = 55^\circ$ fin. Like the pre-

vious example, a prominent separation line was seen. But unlike Figure 22c, there was no secondary separation line. In fact, in interactions with the thicker boundary layer, the secondary separation line was found to be faint even for $\alpha_f = 15^\circ$ fins at smaller fin leading-edge sweepback.

3.3.2 The Upstream Influence

The upstream influence was de. ined by kerosene-lampblack visualization. A cross-check with the upstream influence measurements using surface pressure distributions showed that these two methods were equivalent and of the same order of accuracy. The present study was used to test the validity of the upstream influence correlation of Dolling and Bogdonoff (1981) by using a larger interaction region ($y/\delta > 30$) and by changing the shape of the impinging shock wave through sweeping back the fin leading edge (Figure 24). Discussion of the present measurements will be based mainly on fins with 9° angle of attack with illustrative examples from fins with 5° and 15° angles of attack.

In Figure 25a, the raw upstream influence data of $\alpha_f = 9^\circ$ fins at various leading-edge sweepback are plotted in a Cartesian coordinate system. The upstream influence line, and the inviscid shock wave reference line, became more swept back with fin leading-edge sweep. In addition, except for an inception region close to the fin -- $x_s \lesssim 40$ mm (1.6 in) -- the upstream influence line appeared to be straight and to intercept the fin surface upstream of the apex under extrapolation. The fact that the upstream influence line and the inviscid shock wave location were straight

but not parallel suggested that the region between the upstream influence and the shock wave may be conical. The upstream influence data for α_f = 9° fins mounted on the tunnel floor are also plotted in Figure 25a. The overall trend of the upstream influence becoming more swept with sweepback of the fin leading edge can be seen here as well. But, at a given λ_f, the upstream influence line obtained with the fin mounted on the floor was less swept than that obtained with the fin mounted on the flat plate. In addition, in experiments done with fins mounted on the tunnel floor, the upstream influence lines were found to be more swept at a larger unit Reynolds number (187 x 10^6 m^{-1}) compared to those at a smaller unit Reynolds number of 63 x 10^6 m^{-1}.

The upstream influence data for α_f = 15° and α_f = 5° fins (Figures 25b and 25c) showed the same trends as those for α_f = 9° fins. The sweep of the upstream influence was observed to change more readily with fin sweepback for α_f = 15° fins than for α_f = 5° fins. The sweep of the upstream influence also changed with the fin angle of attack, α_f, becoming more swept back as α_f decreased.

The functional dependence of the upstream influence on flow parameters -- Equations (3) and (4) -- could be combined so that

$$\frac{L_{un}\, Re^{1/3}}{M_n\, \delta_{local}^{2/3}} = f\left\{\frac{L_s\, Re^{1/3}}{\delta_{local}^{2/3}}\right\}. \qquad (11)$$

The upstream influence data were correlated by Equation (11) regardless of whether the leading edges of the fins were swept or not (Figure 26). The upstream influence lines obtained by experiments performed on the flat plate extended further in normalized coordinates than those obtained by experiments performed on the tunnel floor. In addition, the upstream influence in normalized coordinates extended further as the unit Reynolds number increased.

Except possibly at large fin leading-edge sweep, the data showed that the leading-edge sweep did not affect the upstream scaling of Equation (11). The reason may be because the inviscid shock wave envelope impinged perpendicularly onto the test surface. Near the surface, the shock wave would appear to be that generated by a fin without sweepback but at a smaller angle of attack. Although this hypothesis was not checked explicitly, the upstream influence data from Dolling (1982) for an $\alpha_f = 14^\circ$, $\lambda_f = 0^\circ$ fin were used to compare with the upstream influence data for an $\alpha_f = 15^\circ$, $\lambda_f = 20^\circ$ fin. The angle, β_o, was 31.69° and 31.59° respectively. The data, plotted in Cartesian coordinates (Figure 27a), showed that the upstream influence of interactions caused by these two fins fell closely together. When plotted in normalized coordinates (Figure 27b), the upstream influence data for the two cases also fell closely together. With the same incoming conditions, the upstream influence line did not appear to depend so much on α_f and λ_f as on β_o. For highly swept fin-generated interactions, therefore, the inviscid shock wave angle on the test surface, β_o, was important for correlating

upstream influence data; sweeping back the leading edge of the fins did not appear to affect the upstream influence correlation significantly.

3.4 SURFACE PRESSURE DISTRIBUTIONS

3.4.1 General Description

Besides oil flow visualization, surface static pressure readings were taken with fins mounted on the tunnel floor to further study the surface phenomena. Most of the tests were at a unit Reynolds number of 63×10^6 m^{-1}. For unswept fins, these experiments included one example at α_f = 15° which was at a higher angle of attack than those achieved by Oskam *et al.* (1975) under the same incoming conditions.

The data from the present experiments for unswept fins at α_f = 5°, 9° and 15° were compared with those obtained by Oskam *et al.* (Figure 28). Although the pressure readings of Oskam *et al.* were mostly taken 6.3 mm (0.25 in) further inboard than the present data, the general trend with increasing α_f was the same in both sets of experiments. Thus, the pressure gradient became steeper with increasing α_f.

Sweeping back the leading edges of α_f = 15° fins resulted in a slight reduction of the upstream influence length measured from the inviscid shock wave location. The surface pressure levels attained through the interaction were diminished (Figure 29a) with leading edge sweep. For all the fins, the pressure rose rapidly downstream of the upstream influence. At $x_s \gtrsim 70$ mm (2.8 in), the surface pressure ratio for the fins with 10° and 30° sweepback reached the level of 2.8 attained for the unswept fin

whereas that for the $\lambda_f = 55^\circ$ fin was lower, having reached a value of only 2.5. A feature found in the surface pressure distributions of all these fins was a dip in the pressure rise which occurred upstream of the inviscid shock wave location.

For the fins at $\alpha_f = 9^\circ$, the eventual downstream pressure ratio was 1.8 for $\lambda_f = 0^\circ$. This pressure ratio reduced progressively with sweepback (Figure 29b). Also, compared to the $\alpha_f = 15^\circ$ fins, there was no dip in the pressure distributions. Further, there was only a slight change of the upstream influence length with sweepback and the initial pressure gradient was comparatively gentler.

Finally, the $\alpha_f = 5^\circ$ fins generated the weakest interactions. This could be seen in the ultimate downstream pressure ratio of only about 1.4 for the unswept fin and about 1.3 for the $\lambda_f = 55^\circ$ fin (Figure 29c). The initial pressure rise was also considerably smaller.

3.4.2 Reynolds Number Effect

Another set of surface pressure distributions was obtained for $\alpha_f = 9^\circ$ fins at various λ_f and for $\alpha_f = 5^\circ$ and $\alpha_f = 15^\circ$ fins at $\lambda_f = 30^\circ$ with the incoming flow at a higher unit Reynolds number of 187×10^6 m^{-1}. These fins were all tested on the tunnel floor. At the lower unit Reynolds number of 63×10^6 m^{-1}, the Reynolds number based on the average undisturbed boundary layer thickness through the interaction region is $Re_{\delta_{av}} = 1.03 \times 10^6$ whilst at the higher unit Reynolds number of 187×10^6 m^{-1}, $Re_{\delta_{av}} = 2.32 \times 10^6$.

The data at these two Reynolds numbers enabled the Reynolds number effect to be studied. The Reynolds number effect appeared to be noticeable mostly downstream of the inviscid shock wave location on the test surface. For the $\alpha_f = 9^o$, $\lambda_f = 0^o$ fin, the surface pressure distributions at the first spanwise row, $y = 31.8$ mm (1.25 in), showed that the pressure ratio was higher at the downstream region for the higher Reynolds number flow (Figure 30a). At the second and third rows, the increased surface pressure ratio of the higher Reynolds number flow began at about $x_s = -25$ mm (- 1 in) (Figures 30b and 30c). Also clearly seen in these two figures was the slight reduction in the upstream influence as the Reynolds number increased. This was the same as in results obtained with the kerosene-lampblack surface visualization.

The same Reynolds number trend was observed when the fin leading edge was swept back to 30^o (Figure 31) and to 55^o (Figure 32). The ultimate downstream pressure ratios were, of course, smaller for these two cases since the interactions were weaker. But, once again, the pressure ratio for the higher Reynolds number flow was higher downstream of the inviscid shock wave and there was a slight decrease in the upstream influence as well when compared with the results for the lower Reynolds number flow. Thus, the surface pressure distribution approached the downstream inviscid value faster for the flow at the larger Reynolds number.

The surface pressure distribution for an $\alpha_f = 15^o$, $\lambda_f = 30^o$ fin at the three spanwise stations did not reveal a discernible Reynolds number effect (Figure 33). On the other hand, the surface pressure distribution

of the $\alpha_f = 5^\circ$, $\lambda_f = 30^\circ$ fin (Figure 34) showed the same Reynolds number effect as the $\alpha_f = 9^\circ$ fins, that is, there was a higher pressure ratio downstream of the inviscid shock wave location for the higher Reynolds number flow. From these, the Reynolds number effect was seen to be more pronounced at smaller fin angles of attack, or, in other words, with weaker interactions. Therefore, changes in the Reynolds number changes the upstream influence location and the pressure ratio (especially downstream of the inviscid shock wave location). The effect of the Reynolds number appear to be more important for fins with smaller angles of attack.

3.5 THE INTERACTION REGION

The previous discussion on the upstream influence scaling and the surface pressure distribution showed that although the upstream influence length could be measured accurately, the "downstream" influence of the shock wave could not be defined precisely. This was because the flow variables usually required a substantial distance to reach values predicted by inviscid theory. Past experiments showed that the surface pressure level rose to the inviscid value after about 50δ downstream of the inviscid shock wave location (Oskam *et al.* (1975)). The whole interaction region, comprising the upstream region and the poorly defined downstream region, could be subdivided into five regions according to Teng and Settles (1982). Figure 35 shows this for two cases of special interest in the present study: conical and cylindrical interactions. Region I was the incoming freestream region in both conical and cylindri-

cal interactions. The part of the surface flow affected by the apex of the fin was Region II. This was a fully three-dimensional region. Further out spanwise, Region III could be either conical or cylindrical. This was the upstream influence of the shock wave. By such a classification, two-dimensional and cylindrical flows were considered to be special cases. Perfectly conical flow, which developed right from the apex, was also a special case. Some parameters could be defined to characterize Region III (Teng and Settles (1982)). First, this region had a characteristic inception length, L_{incep}, measured from the apex. Next, the normal upstream influence at L_{incep} was $(L_{un})_{incep}$. For the case of a conical interaction, the intercept in the spanwise direction of the inviscid shock wave and the upstream influence line was Δy. In other words, for a conical flow in Region III, the apex of the fin was displaced to an "apparent origin" by a distance Δy. To the rear of Region III was Region IV which was downstream of the shock wave. Region IV then merged into Region V, the recovery region. Regions IV and V formed the downstream influence of the shock wave and are presently poorly defined. The emphasis of this discussion will, therefore, be on the upstream influence region instead.

The lampblack streak deflection angles and the surface pressure distributions supported the hypothesis that the upstream region of fin-generated interactions was quasi-conical. To avoid a lengthy discussion, examples will be drawn from the three fin angles of attack with $\lambda_f = 0^\circ$ and 55° only. The streak deflection angle, σ, for the $\alpha_f = 15^\circ$, $\lambda_f = 0^\circ$ fin

at three spanwise rows (Figure 36a) showed that there was a spanwise growth of the interaction. For this fin mounted on the flat-plate, the upstream influence increased from x_s = - 25 mm at y = 31.8 mm to x_s = - 50 mm at y = 82.5 mm. Other examples also showed a spanwise growth of the upstream influence and the upstream interaction region (Figure 36b to Figure 36f).

If the interaction region possessed cylindrical symmetry, there would not be a spanwise growth of the upstream influence measured from the inviscid shock wave location. On the other hand, if this region was perfectly conical, then the surface oil flow angles would be the same along rays subtended from the apex. Or, similarly, by dividing x_s by y, the data for different spanwise stations would collapse together. This procedure was done for an $\alpha_f = 15^\circ$, $\lambda_f = 0^\circ$ fin (Figure 37). Although the streak angles were closer together, the agreement was still not good. By examining the kerosene-lampblack trace itself, the upstream interaction region was seen to be not truly conical but only quasi-conical, that is, $\Delta y > 0$. Thus, by including an appropriate correction, Δy, the streak angles for the three spanwise stations could be collapsed satisfactorily. For example, Δy = 14 mm (0.55 in) for an $\alpha_f = 15^\circ$, $\lambda_f = 0^\circ$ fin (Figure 38a). See Figure 38b to Figure 38f for other examples.

Further evidence of the quasi-conical nature of the upstream interaction region was provided by surface pressure distributions. For $\alpha_f = 15^\circ$, the respective Δy values required to collapse the spanwise pressure distributions for the $\lambda_f = 0^\circ$ and the $\lambda_f = 55^\circ$ fins were 14 mm (0.55 in)

and 16 mm (0.63 in) (Figures 39a and 39b). These were the same values as those found using surface streak angles. Similarly, the Δy corrections to the spanwise distances for the surface pressure distributions for the $\alpha_f = 9^\circ$ and $\alpha_f = 5^\circ$ fins were found to be the same as those used for the streak angles (Figures 39c through 39f).

To summarize, the variation of Δy with α_f and λ_f (Figure 40) showed that for upright fins, Δy was not greatly affected by the four-fold change of the boundary layer thickness. But, Δy was affected more by the fin geometry, changing with α_f and λ_f. The change of Δy was lesser at $\alpha_f = 15^\circ$ than at $\alpha_f = 5^\circ$. This may be because the interaction tended towards conical symmetry at larger angles of attack. Thus, for the present study, the quasi-conical nature of the upstream interaction region implied that there was a region near the apex of the fin that was affected predominantly by the fin geometry. In addition, there was a region further out where the geometry was unimportant.

3.6 OPTICAL STUDIES

3.6.1 Stereoscopic Photography

The three-dimensional interaction region was examined qualitatively by stereoscopic photographs (Figure 41a) for an $\alpha_f = 15^\circ$, $\lambda_f = 0^\circ$ fin. The acetone that was fed in through a tube at the apex of the fin emerged as a white fog downstream of the so-called separation line (marked by white dots from the fin apex along the tunnel floor). Some large turbulent structures in the form of strands were also visible. Through a stereo-

scope, these were seen to be above the tunnel floor and appeared to originate from the separation line. The separation line itself was ragged when observed under stroboscopic lighting due to the unsteadiness of the flow.

In contrast to the above, the stereoscopic photograph of acetone injection through the apex of an $\alpha_f = 5^o$, $\lambda_f = 0^o$ fin (Figure 41b) did not show the same features. There was little spanwise streaming of the vapor which remained instead confined to the junction of the fin and the floor except for some diffusion downstream.

To determine if there was significant spanwise flow of the acetone vapor further away from the fin, acetone was injected through a static pressure orifice just upstream of the interaction (Figure 41c). This orifice was 63 mm (2.5 in) spanwise from the fin. In the photograph, the white dots marked the inviscid shock wave on the floor whereas in Figure 41a, they marked the separation line. The view through the stereoscope showed that the acetone vapor was diffused and was deflected slightly through the interaction. The streamwise growth of the vapor-filled region was slight, being mostly due to the turbulent diffusion. There was also little upward diffusion of the vapor.

The behavior of the boundary layer appeared different depending on the angle, β_o, of the shock wave that the boundary layer was interacting with. When β_o was large, say 33.1^o due to the $\alpha_f = 15^o$, $\lambda_f = 0^o$ fin, the thin layer of fluid close to the test surface was deflected to angles larger than β_o. There also appeared to be an intense level of turbulence

with large turbulent structures spewing out into the main flow. But when β_o was small, the boundary layer was deflected only slightly.

3.6.2 Light Sheet Photography

The photograph of acetone injected through the apex of an $\alpha_f = 15^\circ$, $\lambda_f = 0^\circ$ fin and illuminated by a light sheet (Figure 42a) was obtained with the light sheet incident perpendicular to the test surface and parallel to the freestream direction. The light sheet was 25 mm (1 in) off the tunnel centerline on the far side of the fin. The tunnel floor appeared as a thin white horizontal line. Reflections off the surface could be seen as well. The acetone vapor spewed rapidly spanwise and remained in a layer adjacent to the surface behind the separation line (marked by S). This secondary flow was below that coming from upstream.

To visualize the incoming boundary layer, it was seeded with acetone through an orifice at the centerline of the tunnel (Figure 42b). The acetone vaporized and quickly filled up the depth of the boundary layer. This vapor-filled layer was deflected upwards at the separation line. Figure 42b, together with Figure 42a, showed that the interaction caused the upstream boundary layer to rise over a secondary flow region.

Flow visualization using an $\alpha_f = 9^\circ$, $\lambda_f = 0^\circ$ fin (Figure 43) also showed a secondary flow region downstream of the separation line and a vertical deflection of the incoming boundary layer. The separation line was clearly visible; it was marked unintentionally by a bright spot of light arising from imperfections in the optical system. Compared to the

$\alpha_f = 15^\circ$, $\lambda_f = 0^\circ$ fin, there was a smaller deflection of the incoming boundary layer and a smaller secondary flow region.

The surface kerosene-lampblack flow pattern did not show a separation line for the $\alpha_f = 5^\circ$, $\lambda_f = 0^\circ$ fin and the stereoscopic photographs showed that the boundary layer was not deflected above β_c through the interaction. Therefore, only acetone injection through a tap on the centerline of the tunnel floor was done for this fin. The light sheet was moved to the centerline of the tunnel for this test. The photograph (Figure 44) showed that the vapor-filled boundary layer remained attached to the floor without lifting off as in the previous examples.

Based on the above observations for unswept fins, extra tests using light sheets with leading-edge sweepback of the $\alpha_f = 9^\circ$ fin were done to investigate the behavior of the boundary layer interacting with the generated shock wave. The light sheet was returned to its original position, 25 mm (1 in) from the tunnel centerline on the far side of the fin and parallel to the freestream. At $\lambda_f = 55^\circ$ sweepback, the kerosene-lampblack visualization showed that the separation line was very faint, if at all present. For this geometry, Figure 45a shows that the acetone injected through the fin apex streamed spanwise past the plane of the light sheet. Acetone injected through the centerline orifice showed the vapor-filled boundary layer moving downstream (Figure 45b). It is not possible to determine clearly from these photographs if the boundary layer had lifted off the surface. The two photographs showed that the vapor-filled regions were not mutually exclusive regions as compared

with, for example, photographs of the regions obtained with the $\alpha_f = 9^\circ$, $\lambda_f = 0^\circ$ fin or the $\alpha_f = 15^\circ$, $\lambda_f = 0^\circ$ fin.

The experiment was repeated for an $\alpha_f = 9^\circ$, $\lambda_f = 30^\circ$ fin which had a separation line in the surface flow pattern. Acetone injection through the apex of the fin also showed the vapor-filled region confined very close to the floor with none flowing upstream of the separation line (Figure 46a). By injecting acetone through the centerline orifice (Figure 46b), the vapor-filled incoming boundary layer was seen to be deflected upwards more than the deflection obtained with an interaction caused by an $\alpha_f = 9^\circ$, λ_f [illegible] and less than the deflection obtained with an interaction caused by an $\alpha_f = 9^\circ$, $\lambda_f = 0^\circ$ fin. There appeared to be a more distinct lift-off (or "separation") of the incoming boundary layer than the photographs in Figure 45.

These experiments showed that the separation line did indeed separate the incoming boundary layer from the secondary flow arising from a swept shock wave interaction. Two distinct flow regions could be seen in the photographs and a "separation line" could be identified. But these photographs did not show two-dimensional separation. In the acetone injection experiments, the secondary flow region, far from being a re-circulating bubble, flowed vigorously in the spanwise direction.

3.7 ADDITIONAL COMMENTS ON THE CONICAL REGION

The evidence from kerosene-lampblack and surface pressure distributions suggested that, except for the apex region, the surface phenomena upstream

of the inviscid shock wave location behaved in a conical manner. The apex region was not conical and was governed chiefly by the geometry which in the present investigation could be characterized by α_f and λ_f. But the conical region was characterized by Δy and L_{incep}. The length Δy was only weakly dependent on Re and δ although it varied significantly with α_f and λ_f. The length L_{incep} was obtained from the correlated upstream influence plots of Figure 26. This length was the value of L_s where the data started to follow a straight line and from those plots,

$$\frac{L_{incep}\, Re^{1/3}}{\delta_{local}^{2/3}} \simeq 10^3. \qquad (12)$$

In the conical flowfield, the important parameters were those of the flow itself, these being M_n, Re and δ, where $M_n = M_\infty \sin \beta_o$. Since β_o was the angle of the inviscid shock wave from the freestream direction on the test surface, the plot of the orientation angles of planar shock waves (Figure 8) had to be revised for the present experiments and this is shown in Figure 47. The angle θ was then the sweepback angle of the inviscid shock wave on the flat surface and was the complement of β_o.

Compared to the simplified diagram of Figure 8 which showed a large region of overlap between swept fins and swept ramps producing the same interaction, the present diagram shows a smaller region. The present experiments showed that the surface features were quasi-conical for $57^\circ < \theta < 70^\circ$ and $\phi > 25^\circ$. In contrast, the experiments of Settles *et al.* (1981)

did not lie in this range; particularly, they were less swept. The swept compression ramps did not, in general, produce attached inviscid shock waves at $\theta > 57^{\circ}, \phi < 25^{\circ}$. Thus, at $\theta = 0^{\circ}$, the interaction was two-dimensional and was therefore cylindrical. As θ increased, the interaction took on a quasi-cylindrical form and eventually became quasi-conical.

The upstream influence data of Settles *et al.* (1981) for highly swept ramps and with attached shock waves were re-plotted according to the scheme of Dolling and Bogdonoff (1981). The measured upstream influence (Figure 48a) showed that the most swept back data were due to the $\alpha_r = 10^{\circ}$, $\lambda_r = 50^{\circ}$ ramp and the least swept back data were due to the $\alpha_r = 24^{\circ}$, $\lambda_r = 30^{\circ}$ ramp. Also measured was the upstream influence for an $\alpha_r = 16^{\circ}$, $\lambda_r = 20^{\circ}$ ramp. Cursory inspection of the data showed that for the highly swept models, the upstream influence was growing relative to the inviscid shock wave location (or, equivalently, the ramp leading edge). But for the less swept case, the upstream influence remained approximately constant.

The scaled ramp data were plotted together with the scaled fin data (Figure 48b). The interaction due to the $\alpha_r = 16^{\circ}$, $\lambda_r = 20^{\circ}$ ramp was quasi-cylindrical in nature since the correlated upstream influence length was parallel to the shock wave location and did not increase with span. But the correlated upstream influence lengths for the highly swept ramps grew with span although not as fast as the correlated upstream influence lengths of the fins. In these examples, the inception length to a conical field for swept ramps with attached shock waves was also given by Equation 12. From these observations, both θ and ϕ would be needed to determine if

the ramp interaction was quasi-conical or quasi-cylindrical in nature.

Chapter 4

CONCLUSIONS

The present study is one of the first systematic approaches to examine interactions generated by fins with leading edge sweepback. The paucity of studies using such configurations prevented comparison except with interactions generated by upright fins that were extensively studied at the Gas Dynamics Laboratory of Princeton University. The main parameters controlling the surface features in the apex region and in the farfield conical interaction region have been isolated for a range of incoming flow conditions and shock wave orientations.

4.1 SUMMARY

4.1.1 Main Parameters Affecting the Interaction

The surface flow patterns of sharp fin interactions can be divided in a similar way as that of swept ramp interactions (Teng and Settles (1982)). From surface flow visualization and surface pressure measurements, sharp fin interactions can be seen to produce quasi-conical surface features. The present study, which concentrated on the region upstream of the inviscid shock wave location, shows that in this portion of the surface flow, two regions can be identified. These are the apex region which is close to the fin and the conical region further away. The apex region is affected by the geometry which can be characterized by α_f and λ_f. The farfield region is a conical region affected by flow parameters such

as M_n, Re and δ.

4.1.1.a. The Upstream Influence

The upstream influence of sharp fins determined by kerosene-lampblack surface flow visualization are found to be the same as those determined by surface pressure distributions within experimental accuracy. The kerosene-lampblack technique is perhaps the more versatile one for this purpose because while the upstream influence measurements from surface pressure readings are limited to specific points in the interaction region, those from surface flow visualization can reveal the whole upstream influence line.

This study shows that for a fixed fin geometry, the upstream influence scales by $Re_u^{1/3}/\delta^{2/3}$. But, if the leading-edges of the fins are swept back, the upstream influence then scales by M_n. Therefore, the upstream influence line moves with the inviscid shock wave location. As the inviscid shock wave location on the test surface moves closer to the fin with increasing λ_f at a fixed α_f, so does the upstream influence line. Thus, the same scaling laws apply for fins with leading-edge sweep as those for upright fins. The success in using the same scaling laws as those proposed by Dolling and Bogdonoff (1982) appears to arise from the small changes in the inviscid shock wave location near the test surface when λ_f changes, that is, large changes in λ_f cause only small changes in β_o. Based on the limited data of the present experiments and those of Dolling (1982), the upstream influence can be scaled by M_n, Re and δ according to

Equation (11) regardless of whether the fin leading-edge is swept or not.

4.1.1.b. The Surface Static Pressure and the Reynolds Number Effect

The surface pressure distributions through the interaction region show that the pressure starts to rise upstream of the inviscid shock wave location on the test surface. For particular examples where the leading-edges of the fins were unswept, the downstream pressure ratio can be readily obtained from the perfect gas shock tables. The present results show that the pressure takes more than 75 mm (3 in) or 5 δ_{av} downstream of the inviscid shock wave location before even reaching those inviscid pressure levels. These results are the same as those obtained by Oskam *et al.* (1975) who tested upright fins from 2^{o} to 14^{o} angle of attack.

When the leading edge of the fin is swept back at a constant α_f, the pressure rise tends to be less as λ_f increases. In addition, the upstream location tends to be closer to the inviscid shock wave location. These changes are because the interaction becomes weaker as the leading-edge is swept back.

In experiments to determine the changes of the pressure distribution with changes in the Reynolds number, the present study found that an increase in the Reynolds number results in a decrease in the downstream pressure levels and a movement of the upstream influence closer to the inviscid shock wave location. These changes are more important with weaker interactions, for example, those generated by $\alpha_f = 5^{o}$ fins.

4.1.2. Experimental Techniques

The well-tested kerosene-lampblack technique used in this study enables a general qualitative picture of the surface features found in such a shock wave boundary layer interaction to be obtained quickly. In addition, it can be used to obtain the upstream influence. This has been validated here by a comparison with the usual technique using surface pressure distributions. Both the surface streak pattern and the surface pressure distributions have been found in this study to exhibit the same quasi-conical behavior. They provide limited evidence at the present that highly swept fin interactions are quasi-conical in nature.

The interaction was studied by a localized vapor-screen visualization in an attempt to link surface features with features above the surface. There appears to be a change in the behavior of the boundary layer when it interactions with the shock wave depending on whether a "separation line" appeared or not. When a separation line is not seen in the kerosene-lampblack traces, for example, when α_f is 5°, the incoming boundary layer undergoes a mild spanwise deflection. But when a separation line is seen in the kerosene-lampblack traces, the incoming boundary layer undergoes a spanwise and an upward deflection. The evidence suggests that when "separation" occurs, the incoming boundary layer lies above another layer of fluid which is moving rapidly in the spanwise direction. The most upstream extent of this bottom layer is the separation line.

4.2 SUGGESTIONS FOR FURTHER STUDY

To determine if not only the surface features in the farfield are conical but if the flowfield itself is conical as well, flowfield measurements must be done at different spanwise distances and then correlated. Whether the flowfield is quasi-conical is an important piece of information towards understanding swept interactions.

In addition, a comprehensive set of data for interactions at a different (preferably lower) Mach number is needed to compare the Mach number and the sweep effects with those of the present experiments. The interactions at a lower Mach number flow will generally be less swept than those in the present experiments. Another way of obtainining less swept interactions at Mach 3 is by using fins with $\alpha_f > 15^o$. Hence, Mach number and shock sweepback effects can be checked through the correlations used in the present study.

An interesting study of highly swept interactions is to use half-cones as shock generators (a realistic problem in engine inlets). Such a study will complement the present study and those studies using swept ramps. An advantage of this geometry is that the inviscid solution for attached shocks is known. Together with fin and ramp studies, these studies map out a large region of three-dimensional shock wave turbulent boundary layer interactions.

REFERENCES

1. Adamson, T.C., Jr. and Messiter, A.F., "Analysis of Two-Dimensional Interactions Between Shock Waves and Boundary Layers." *Ann. Rev. Fluid Mech.*, *12*, 103-138, 1980.

2. Cooper, J.R. and Hankey, W.L., Jr., "Flow Field Measurements in an Asymmetric Axial Corner at M = 12.5" *AIAA J.*, *12*, No. 10, 1353-7, October 1974.

3. Cousteix, J. and Houdeville, R., "Epaississement et separation d'une couche limite turbulente soumise en interaction avec un choc oblique." *Rech. Aerosp.*, No. 1976-1, 1-11, 1976.

4. Dolling, D.S., private communication, January, 1982.

5. Dolling, D.S. and Bogdonoff, S.M., "Upstream Influence Scaling of Sharp Fin-Induced Shock Wave Turbulent Boundary Layer Interactions." AIAA Paper 81-0336, 1981.

6. Green, J.E., "Interactions Between Shock Waves and Turbulent Boundary Layers." *Prog. in Aerospace Sci.*, *11*, D. Kucheman, ed., 235-340, 1970.

7. Holman, J.P., "Experimental Methods for Engineers." 3rd ed., McGraw-Hill, New York, 1978, 44-51.

8. Korkegi, R.H.,"A Simple Correlation for Incipient Turbulent Boundary-Layer Separation due to a Skewed Shock Wave." *AIAA J.*, *11*, No. 11, 578-9, November 1973.

9. Korkegi, R.H., "On the Structure of Three-Dimensional Shock-Induced Separated Flow Regions." *AIAA J.*, *14*, No. 5, 597-600, May 1976.

10. Kuehn, D.M., "Experimental Investigation of the Pressure Rise Required for the Incipient Separation of Turbulent Boundary Layers." NASA Memo. I-21-59A, 1959.

11. Law, C.H., "Three-Dimensional Shock Wave-Turbulent Boundary Layer Interactions at Mach 6." ARL TR 75-0191, June 1975.

12. Lighthill, M.J., "On Boundary Layers and Upstream Influence. II. Supersonic Flows Without Separation." *Proc. Roy. Soc.*, *A217*, 478-507, 1953.

13. McCabe, A., "A Study of Three-Dimensional Interactions Between Shock Waves and Turbulent Boundary Layers." Ph.D. Dissertation, University of Manchester, England, October 1963.

14. McCabe, A., "The Three-Dimensional Interaction of a Shock Wave with a Turbulent Boundary Layer." *Aero.Quart.*, *17*, Pt. 3, 231-52, August 1966.

15. Myring, D.F., "The Effect of Sweep on Conditions at Separation in Turbulent Boundary-Layer/Shock-Wave Interaction." *Aero. Quart.*, *28*, Pt. 2, 111-122, May 1977.

16. Oskam, B., "Three-Dimensional Flow Fields Generated by the Interaction of a Swept Shock Wave with a Turbulent Boundary Layer." Ph.D. Dissertation, Princeton University, 1976.

17. Oskam, B., Bogdonoff, S.M., and Vas, I.E., "Study of Three-Dimensional Flow Fields Generated by the Interaction of a Skewed Shock Wave with a Turbulent Boundary Layer." AFFDL-TR-75-21, February, 1975.

18. Peake, D.J., "The Three-Dimensional Interaction of a Swept Shock Wave with a Turbulent Boundary Layer and the Effects of Air Injection on Separation." Ph.D. Dissertation, Carleton University, Canada, March 1975.

19. Settles, G.S., "An Experimental Study of Compressible Turbulent Boundary Layer Separation at High Reynolds Numbers." Ph.D. Dissertation, Princeton University, 1975.

20. Settles, G.S. and Perkins, J.J., unpublished data, 1980.

21. Settles, G.S., Perkinds, J.J. and Bogdonoff, S.M., "Investigation of Three-Dimensional Shock/Boundary Layer Interactions at Swept Compression Corners." *AIAA J.*, *18*, No. 7, 779-785, July 1980.

22. Settles, G.S., Perkinds, J.J. and Bogdonoff, S.M., "Upstream Influence Scaling of 2D & 3D Shock/Turbulent Boundary Layer Interactions at Compression Corners." AIAA Paper 81-0334, 1981.

23. Stanbrook, A., "An Experimental Study of the Glancing Interaction Between a Shock Wave and a Turbulent Boundary Layer." ARC CP 555, July 1960.

24. Stewartson, K. and Williams, P.G., "Self-Induced Separation." *Proc. Roy. Soc.*, *A312*, 181-206, 1969.

25. Sun, C.C. and Childs, M.E., "A Modified Wall Wake Velocity Profile for Turbulent Compressible Boundary Layers." *AIAA Journal of Aircraft*, *10*, No. 5, 381-383, June 1973.

26. Teng, H.Y. and Settles, G.S., "Cylindrical and Conical Upstream Influence Regimes of 3-D Shock/Turbulent Boundary Layer Interactions." AIAA Paper 82-0987, 1982.

27. Vas, I.E. and Bogdonoff, S.M., "A Preliminary Report on the Princeton University High Reynolds Number 8" x 8" Supersonic Tunnel." Internal Memo. No. 39, Gas Dynamics Laboratory, Dept. of Aero. and Mech. Sci., Princeton University, 1971.

28. Zehltovodov, A.A., "Three-Dimensional Interaction of a Shock Wave Generated by a Wedge-Shaped Obstacle with a Turbulent Boundary Layer." *Astrophysical Investigations*, No. 6 (in Russian), Scientific Proceedings of the Inst. of Theoretical and Applied Mech., Siberian Branch of the USSR Academy of Sciences, Novosibirsk, 1976.

29. Zubin, M.A. and Ostapenko, N.A., "Structure of Flow in the Separated Region Resulting from Interaction of a Normal Shock Wave with a Boundary Layer in a Corner." Iz. Ak. Nauk. SSR, *Mekh. Zhid. i Gaza*, No. 3, 51-58, May-June 1979 (Eng. trans.).

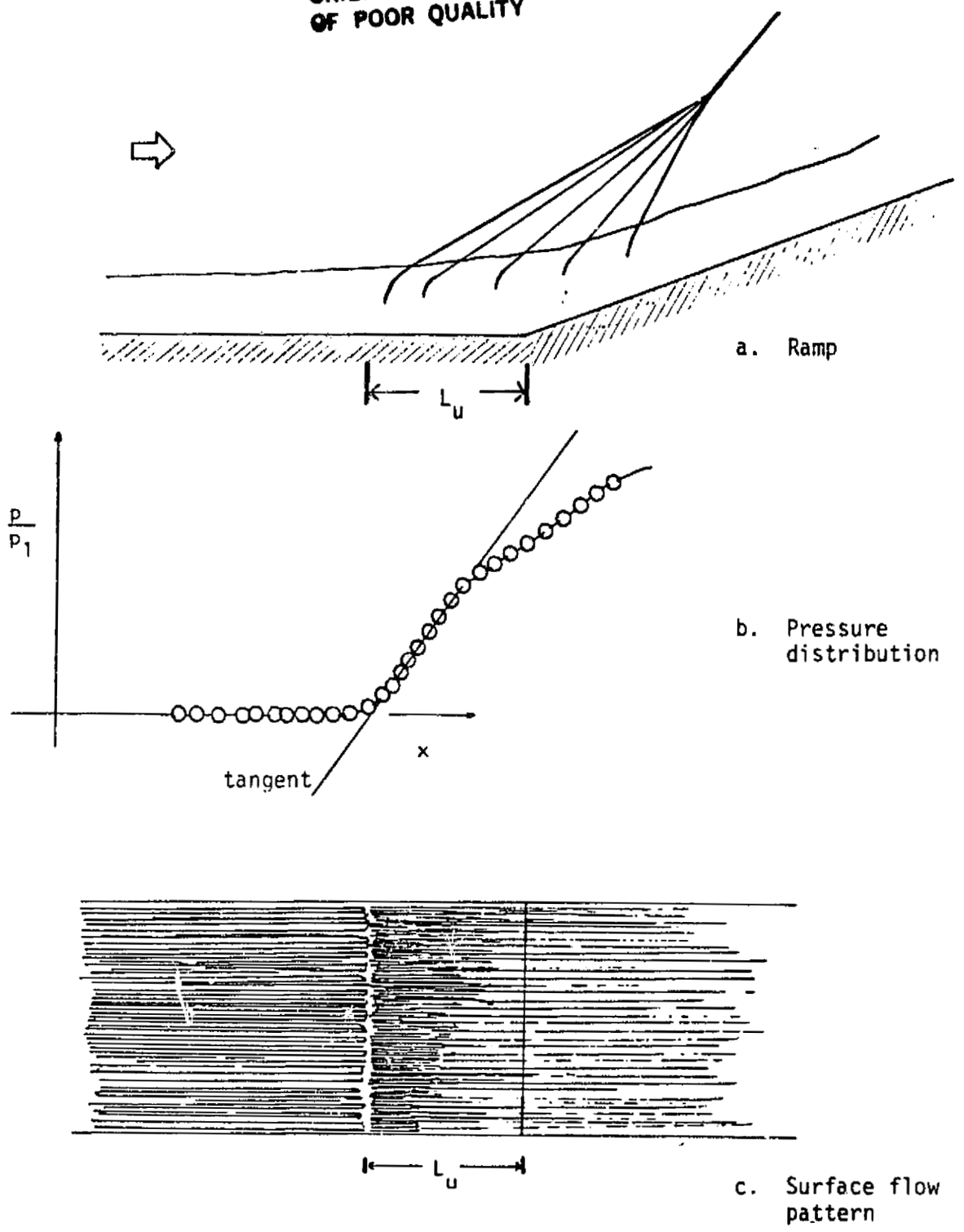

Figure 1. Sketch showing the upstream influence length determined from pressure distributions and from surface flow patterns for a ramp.

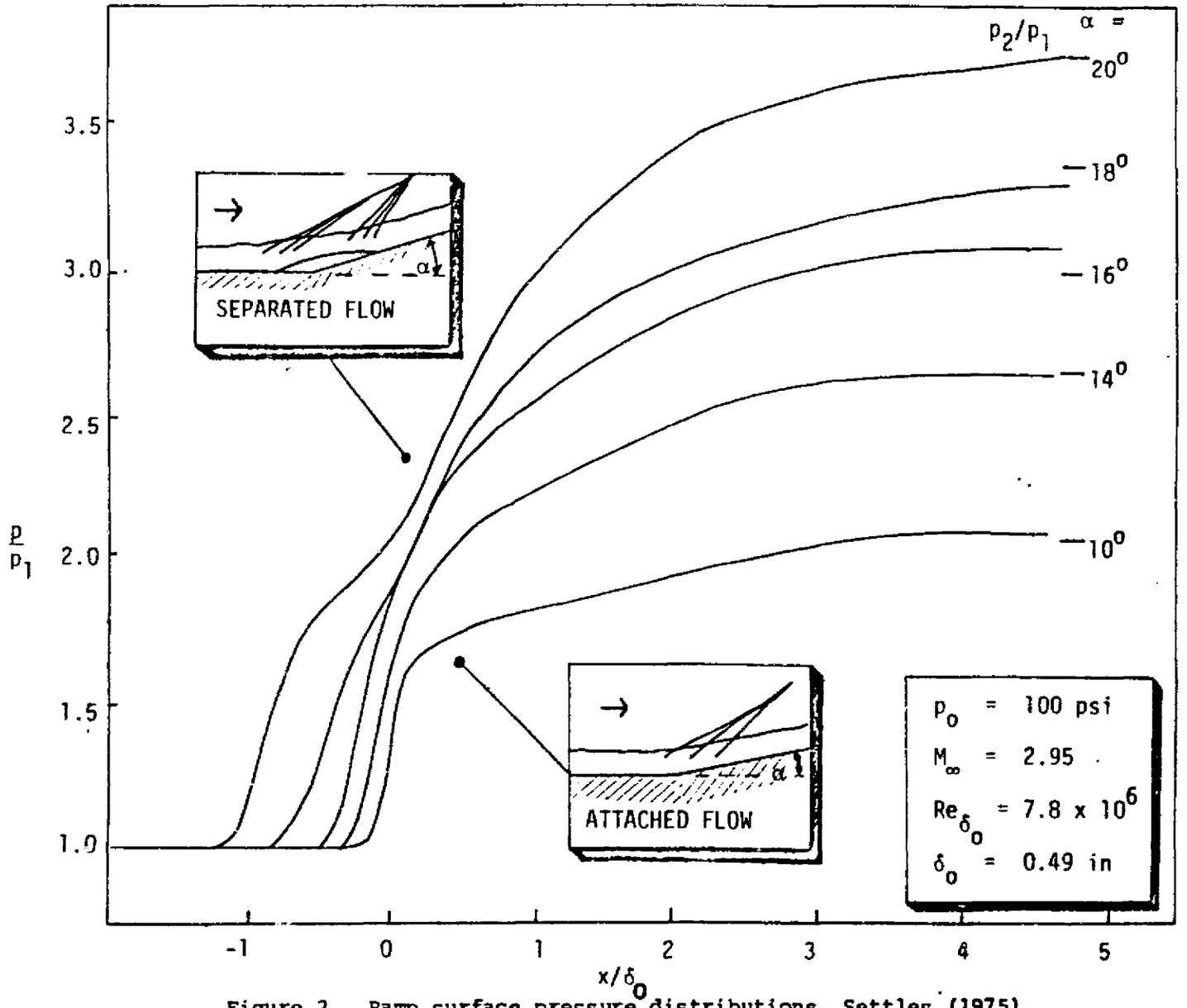

Figure 2. Pamp surface pressure distributions, Settles (1975).

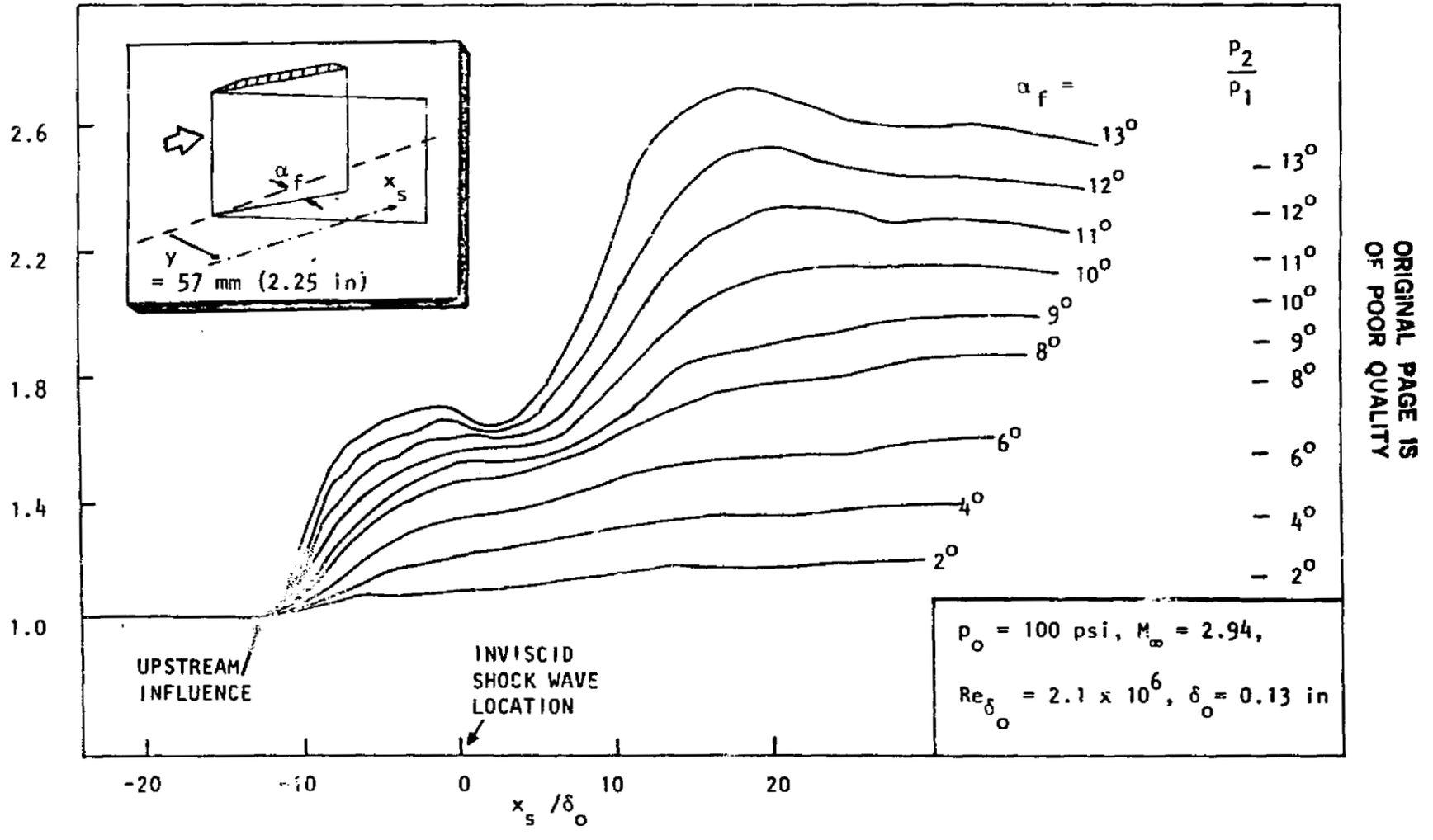

Figure 3. Surface static pressure distributions for a three-dimensional shock wave boundary layer interaction due to a fin, Oskam (1976).

REFERENCES	EXPERIMENTAL CONDITIONS			TUNNEL CROSS-SECTION	FIN ANGLE OF ATTACK	REMARKS
	MACH NUMBER	UNIT REYNOLDS NUMBER	INCOMING BOUNDARY LAYER THICKNESS			
Stanbrook (1961)	1.6 1.8 2.0	1.5×10^7/m (0.37×10^6/in) 1.4×10^7/m (0.35×10^6/in) 1.3×10^7/m (0.33×10^6/in)	3.56 mm (0.14 in) 3.56 mm (0.14 in) 3.56 mm (0.14 in)	100 mm x 100 mm (4 in x 4 in)	2^o to 12^o	Three-dimensional (conical) up to 10δ spanwise from fin; artificial transition, model on centerline of wind tunnel.
McCabe (1966)	1.96 2.94	1.35×10^7/m (3.44×10 /in) 8.1×10^6/m (2.06×10^5/in)	3.56 mm (0.14 in) 5.84 mm (0.23 in)	100 mm W x 125 mm H (4 in W x 5 in H)	2.5^o to 20^o 2.5^o to 10^o	Tendency to cylindrical symmetry after 70δ*, distance measured parallel to the shock; model on tunnel centerline.
Law (1975)	5.85	3.3×10^7/m (10^7/ft) 9.8×10^7/m (3×10^7/ft)	3.3 mm (0.13 in)	254 mm W (10 in W)	4^o to 20^o	Conical up to 30δ, measured parallel to the shock; model offset from tunnel centerline.

Figure 4. Some observations on highly swept interactions.

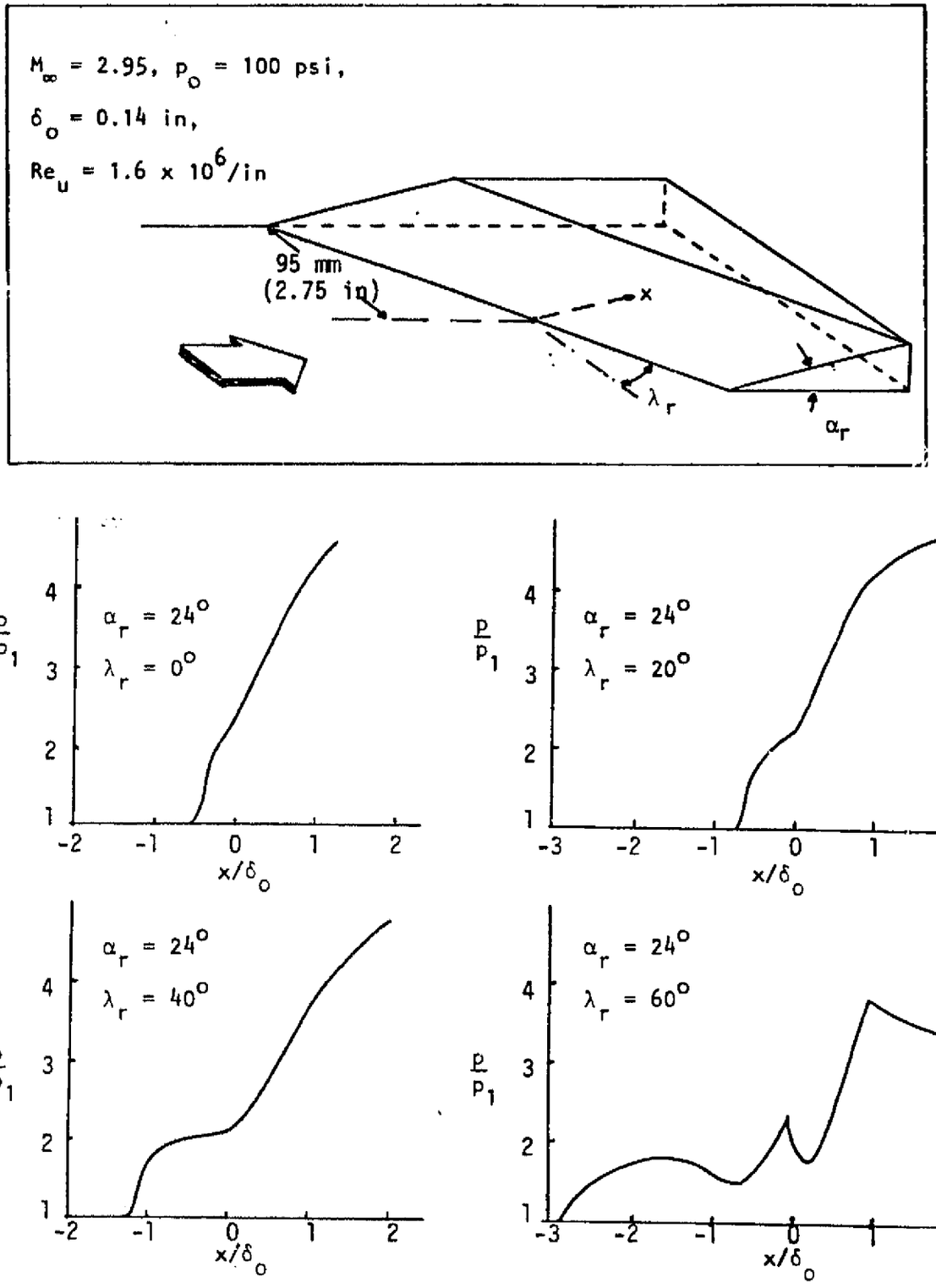

Figure 5. Surface pressure distributions from swept ramp interactions, (Settles and Perkins, 1981).

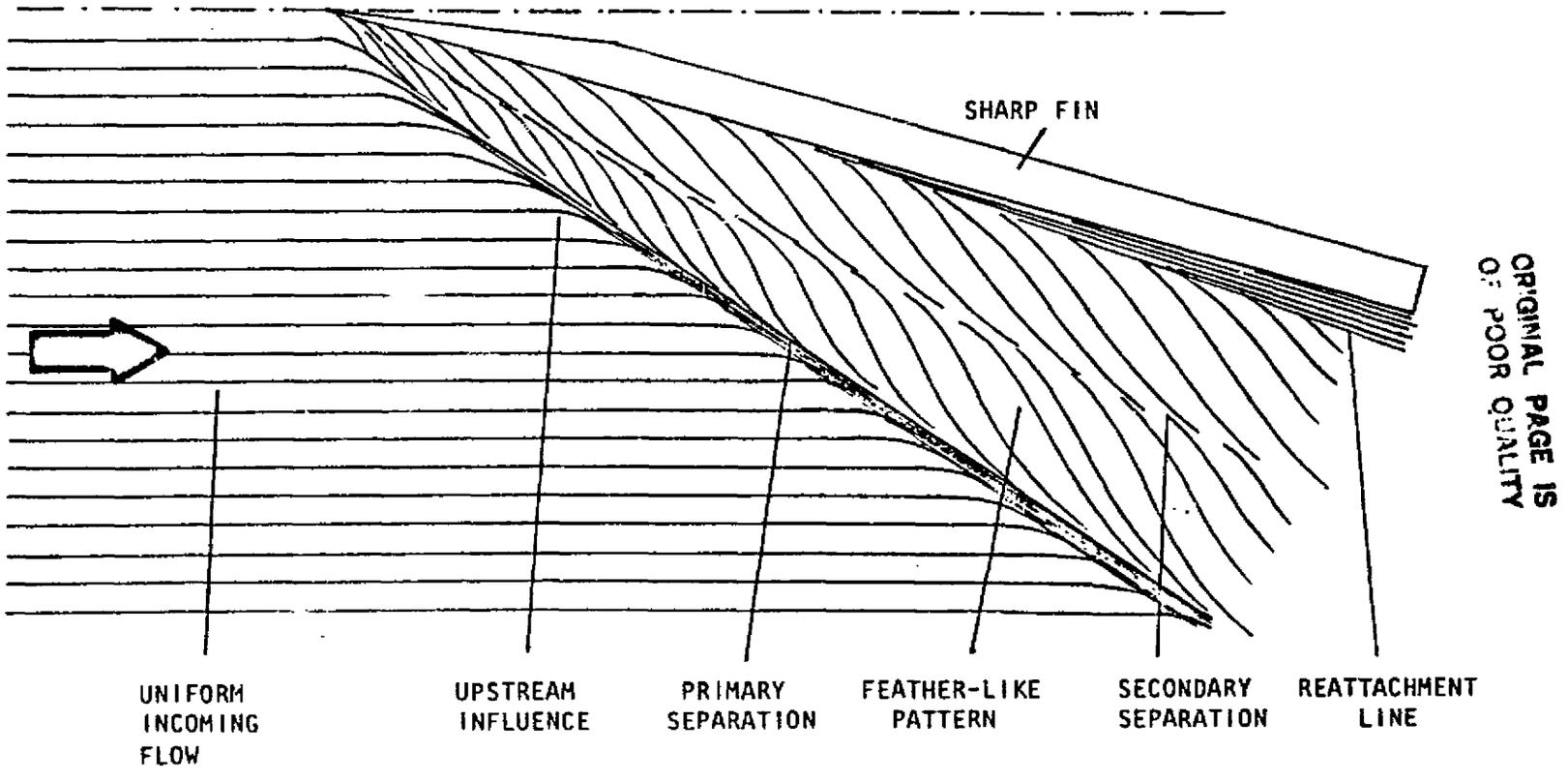

Figure 6. Sketch illustrating features in the surface oil flow past a swept shock wave.

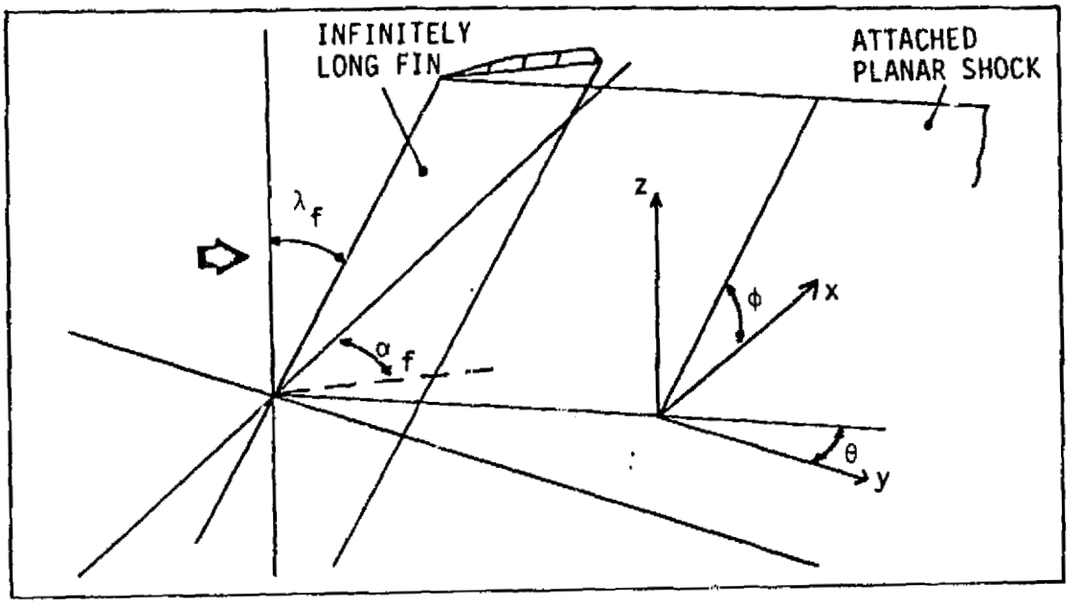

a. Infinitely long fin.

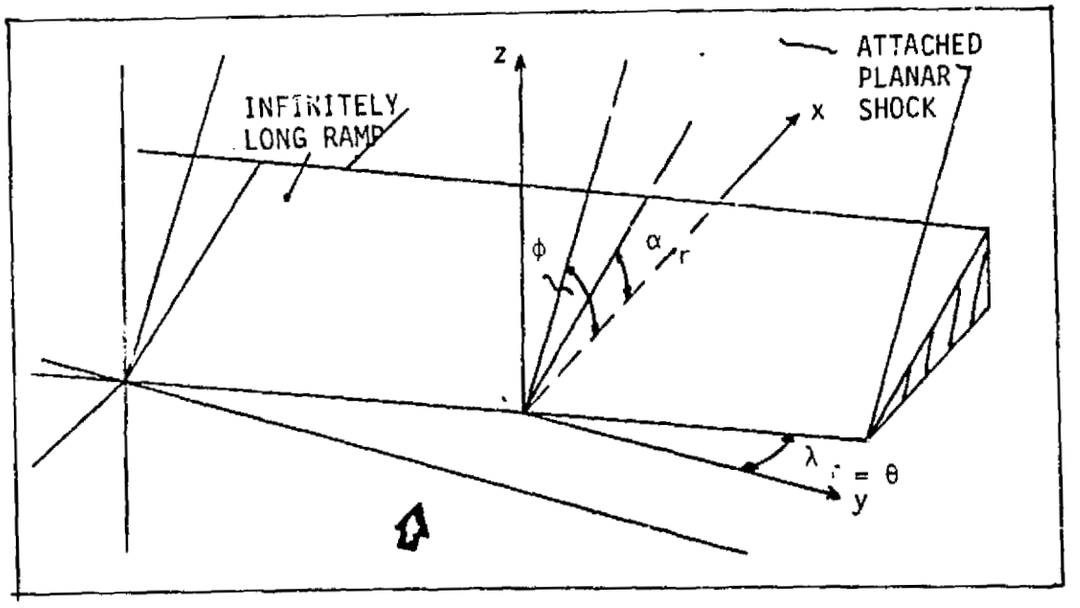

b. Infinitely long ramp.

Figure 7. Geometries for producing swept planar shock waves.

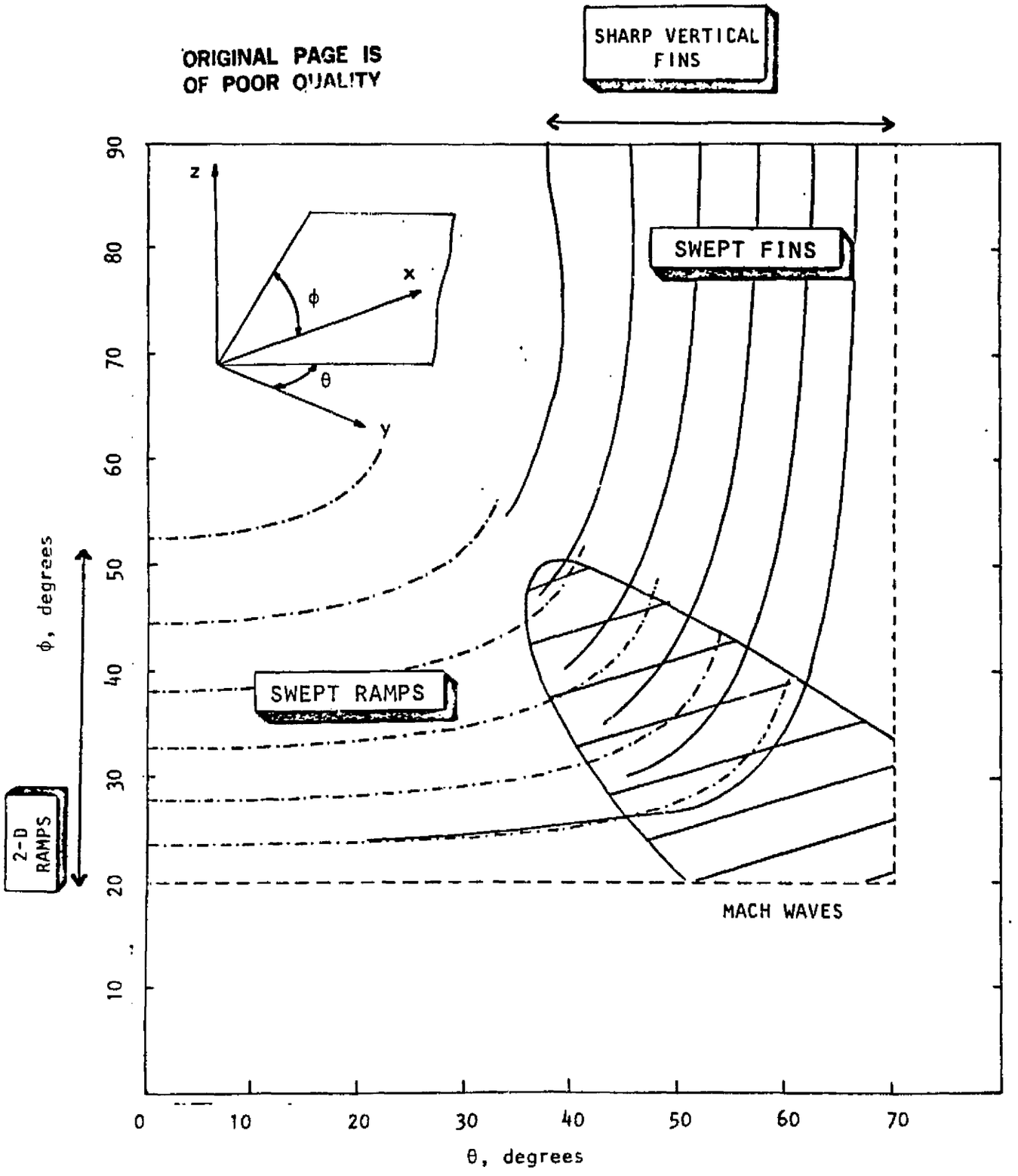

Figure 8. The orientation of planar shock waves attached to infinitely long ramps and fins at $M_\infty = 2.95$.

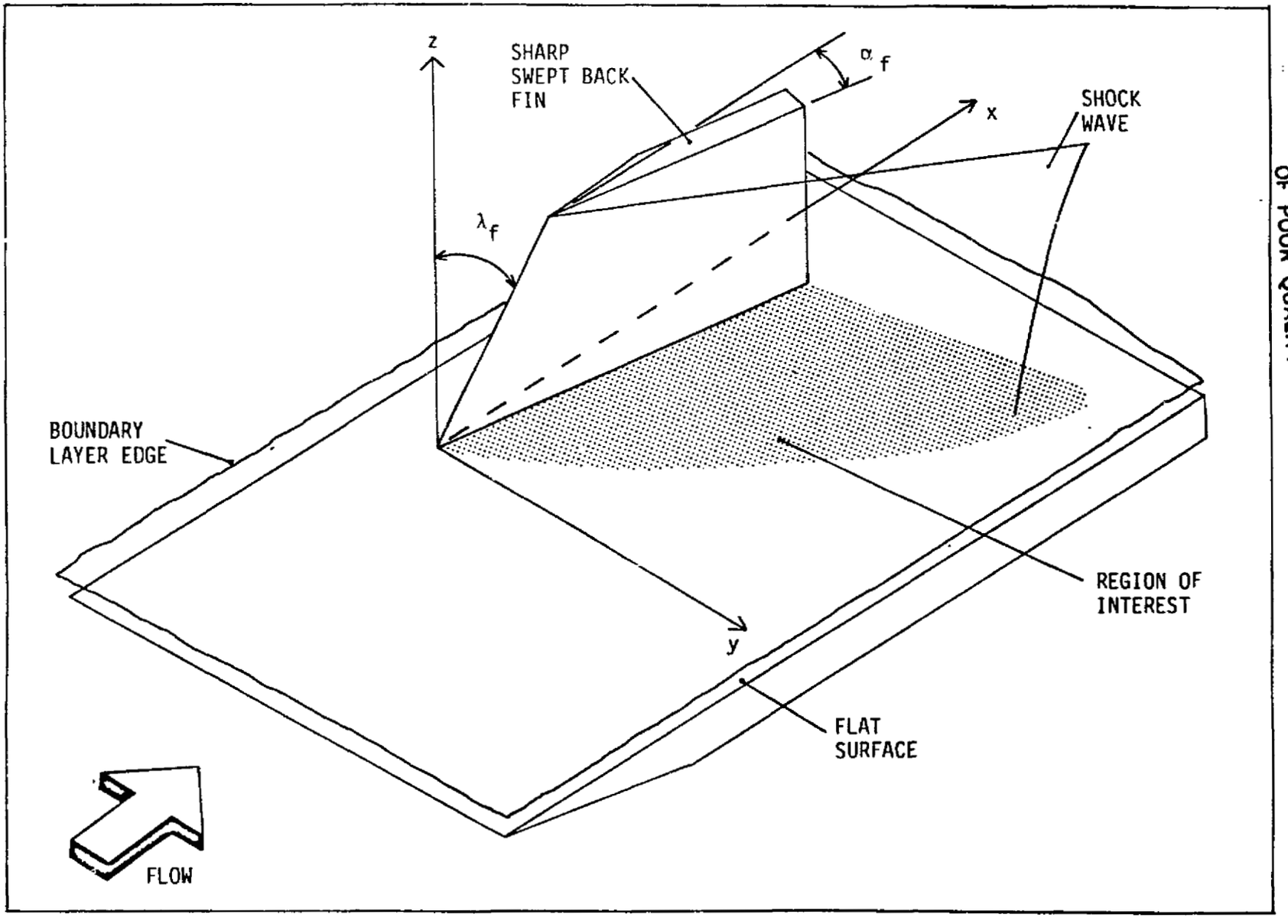

Figure 9. Schematic diagram of the test geometry.

A. EXPERIMENTAL PROCEDURE

1. KEROSENE-LAMPBLACK SURFACE FLOW VISUALIZATION
2. LOCATION OF THE INVISCID SHOCK WAVE
3. SURFACE STATIC PRESSURE MEASUREMENTS
4. VAPOR INJECTION

B. DATA ANALYSIS

1. UPSTREAM INFLUENCE SCALING
2. SURFACE PRESSURE DISTRIBUTION
3. NATURE OF THE UPSTREAM REGION
4. COMPARISON WITH RAMP INTERACTIONS
5. EXAMINATION OF FLOW VISUALIZATION RESULTS
6. EFFECT OF SWEEPING BACK THE FIN LEADING EDGE
7. EFFECT OF THE SWEEPBACK OF THE SHOCK WAVE

Figure 10. Summary of the experimental program.

FIN SWEEP ANGLE, λ_f		SHOCK GENERATOR ANGLE, α_f					
		5°		9°		15°	
0°	l	305	(12)	254	(10)	254	(10)
	h	127	(5)	100	(4)	100	(4)
10°	l	305	(12)	254	(10)	254	(10)
	h	127	(5)	100	(4)	100	(4)
20°	l	305	(12)	254	(10)	254	(10)
	h	127	(5)	100	(4)	100	(4)
30°	l	305	(12)	305	(12)	305	(12)
	h	127	(5)	127	(5)	127	(5)
40°	l	305	(12)	305	(12)	305	(12)
	h	127	(5)	127	(5)	127	(5)
50°	l	305	(12)	305	(12)	305	(12)
	h	127	(5)	127	(5)	127	(5)
55°	l	305	(12)	305	(12)	305	(12)
	h	127	(5)	127	(5)	127	(5)
65°	l	305	(12)	305	(12)	305	(12)
	h	127	(5)	127	(5)	127	(5)

DIMENSIONS IN mm (inches).

Figure 11. Swept fin test geometry.

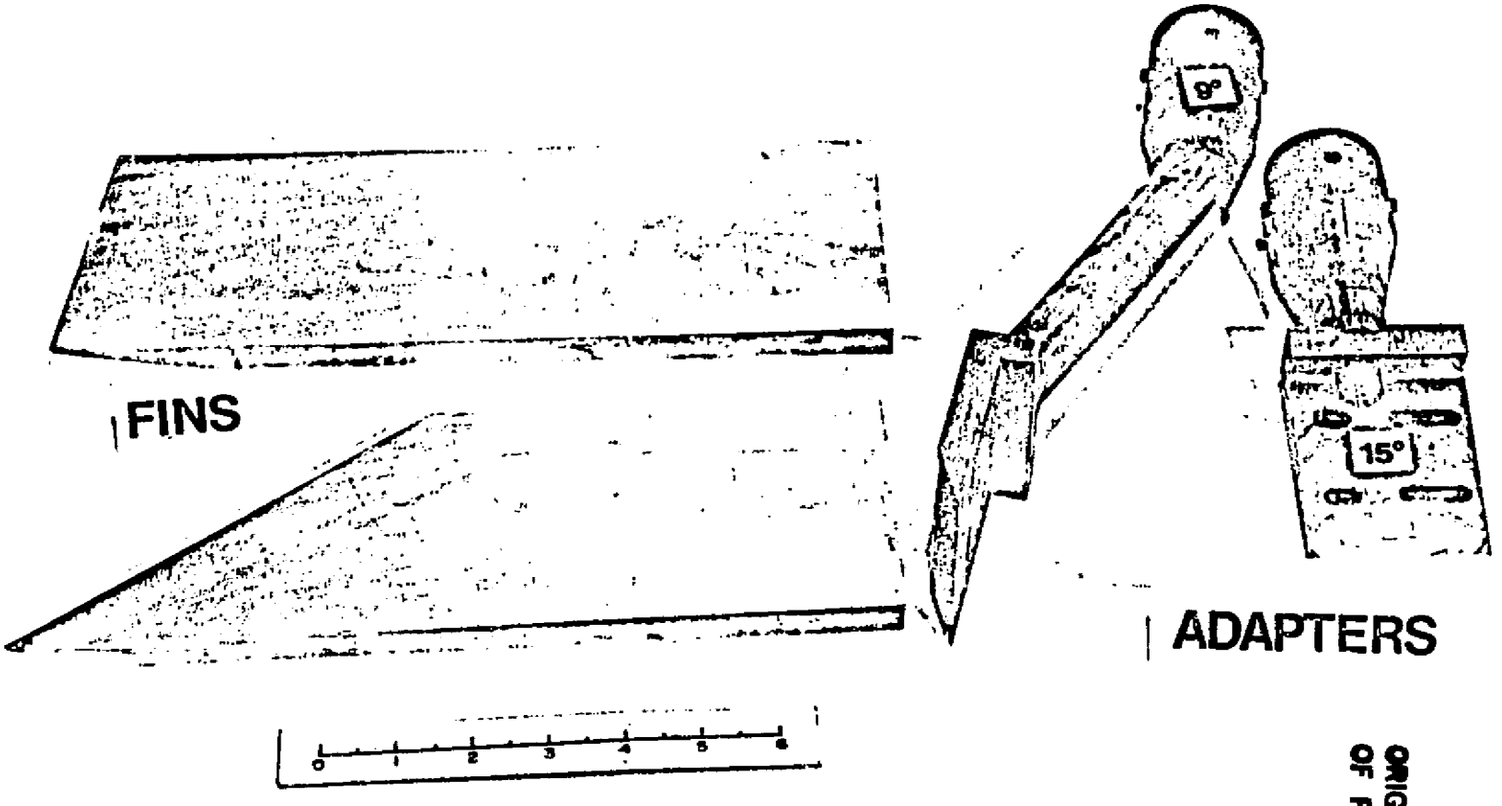

Figure 12. Photograph of some of the fins and adapters used in the experiments.

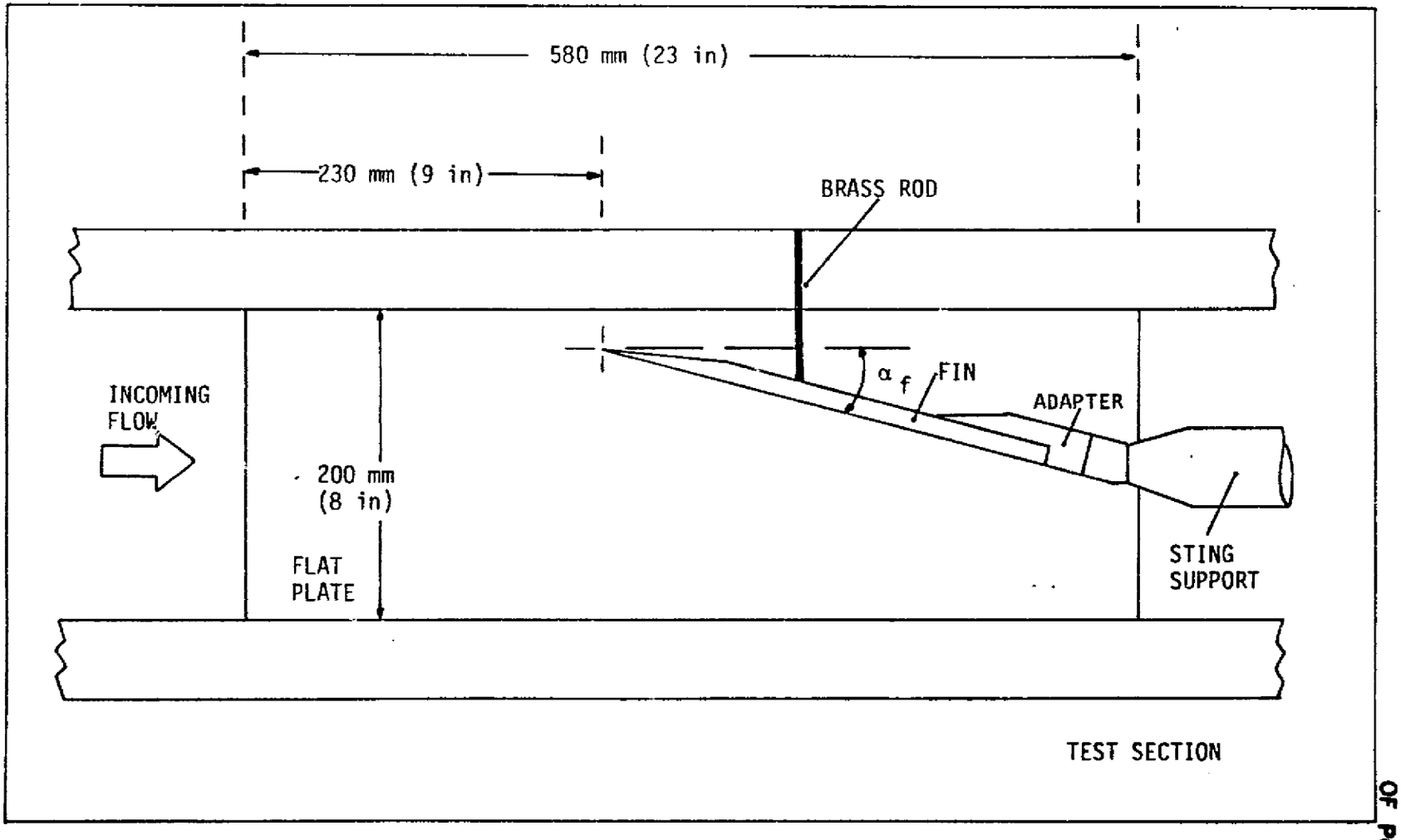

Figure 13. Plan view of a fin mounted on top of a flat plate.

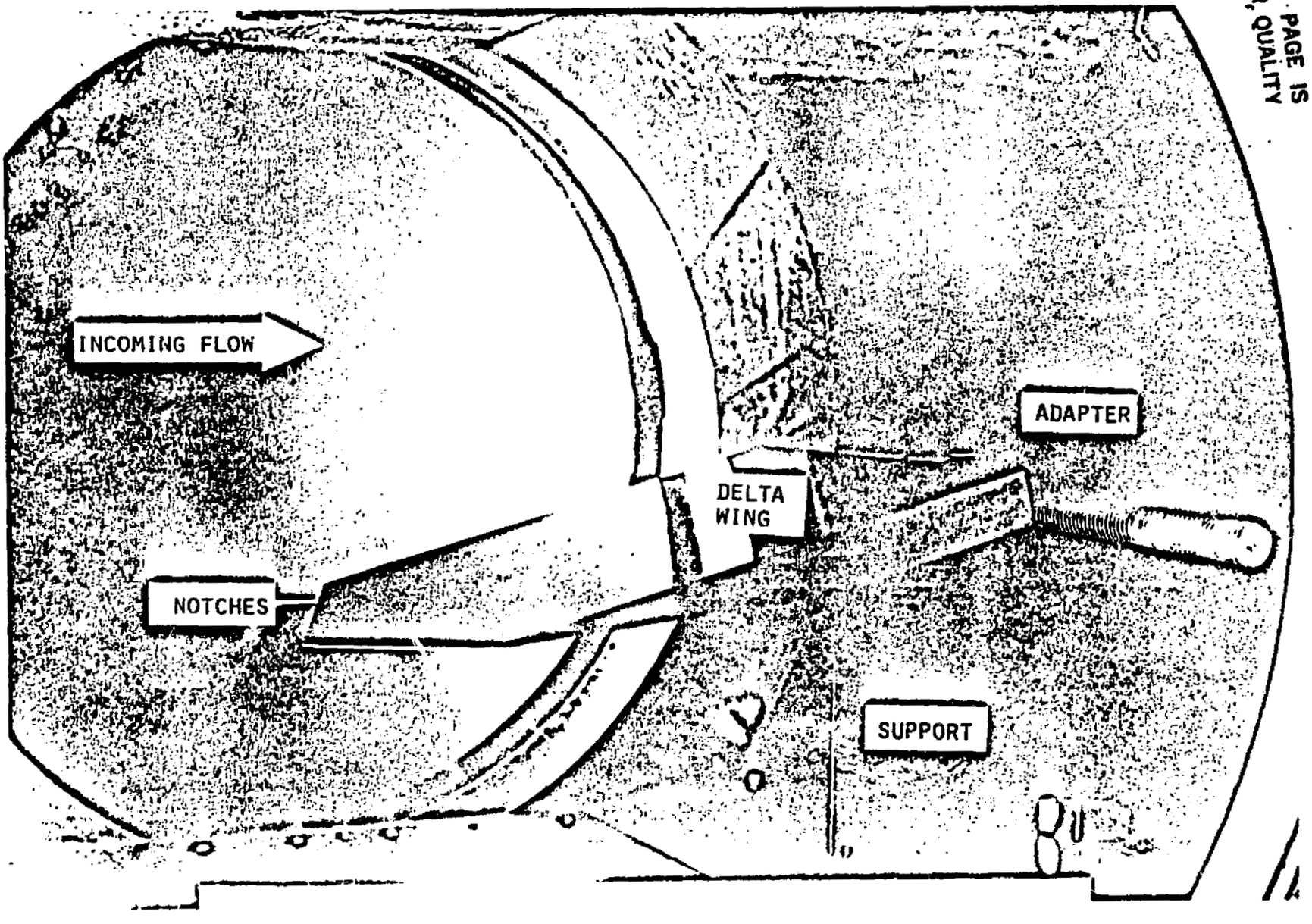

Figure 14. Photograph of a delta wing mounted in the test section.

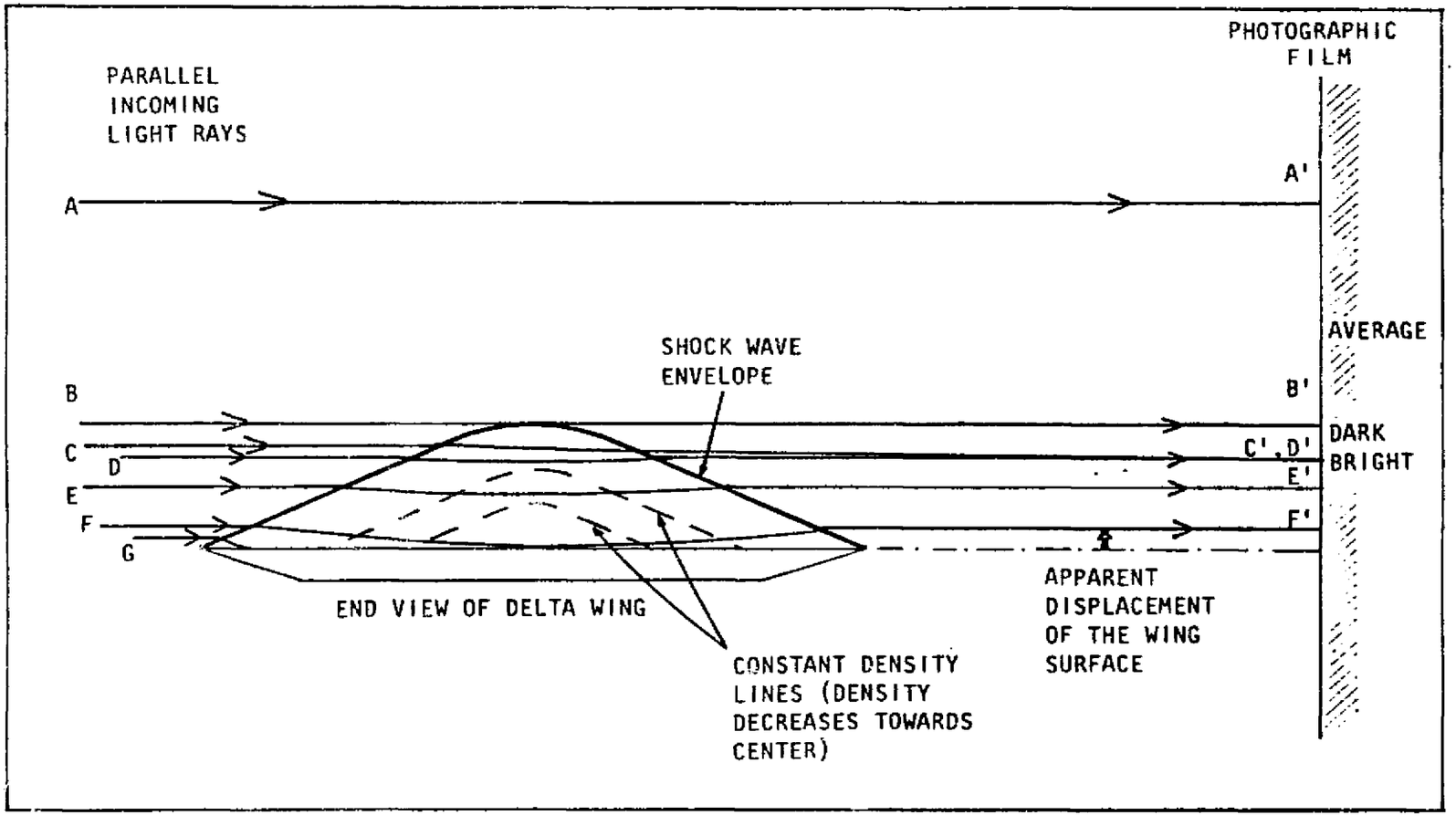

Figure 15. Deflection of light rays through a conical density field.

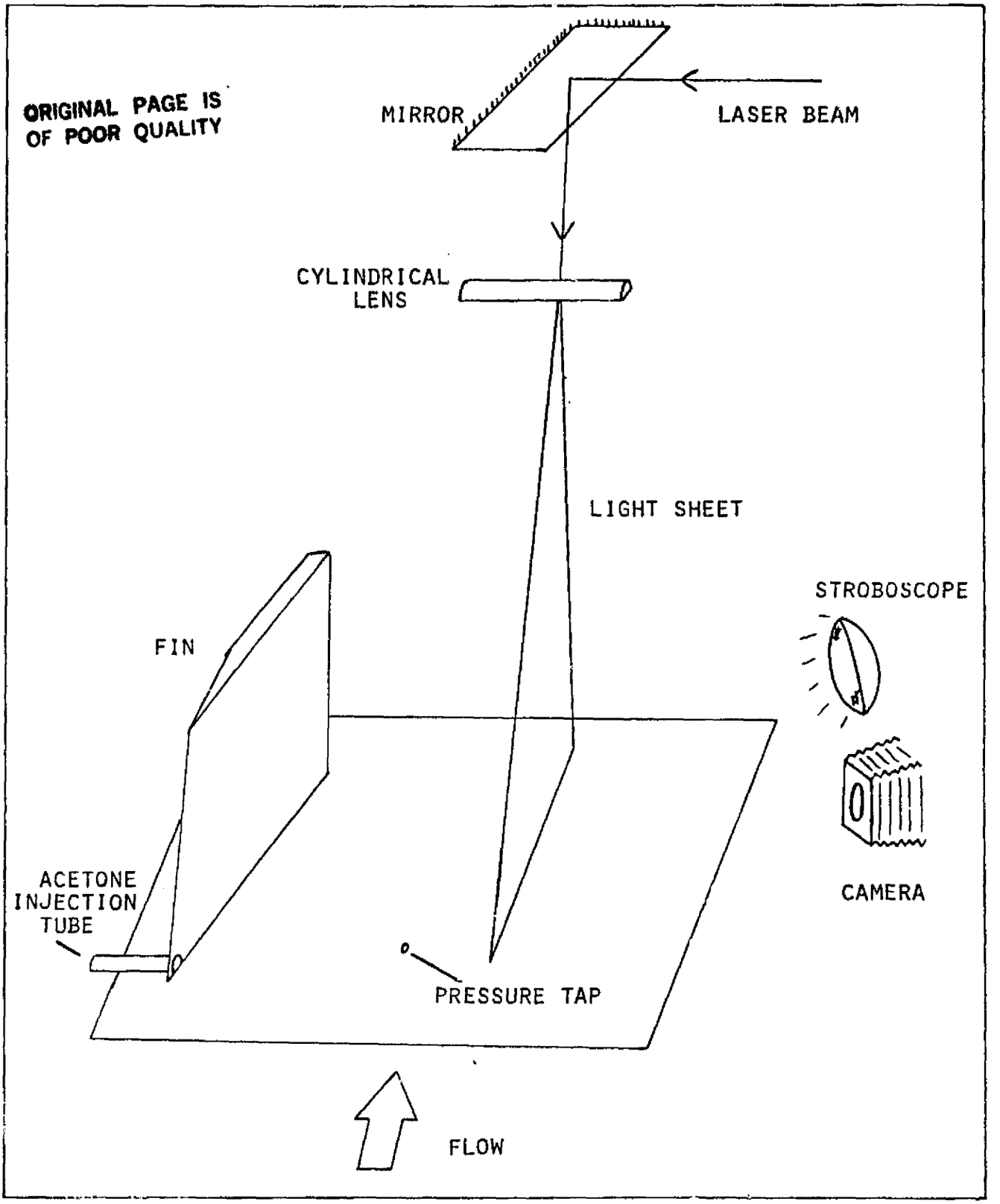

Figure 16. Schematic diagram of the local vapor-screen apparatus.

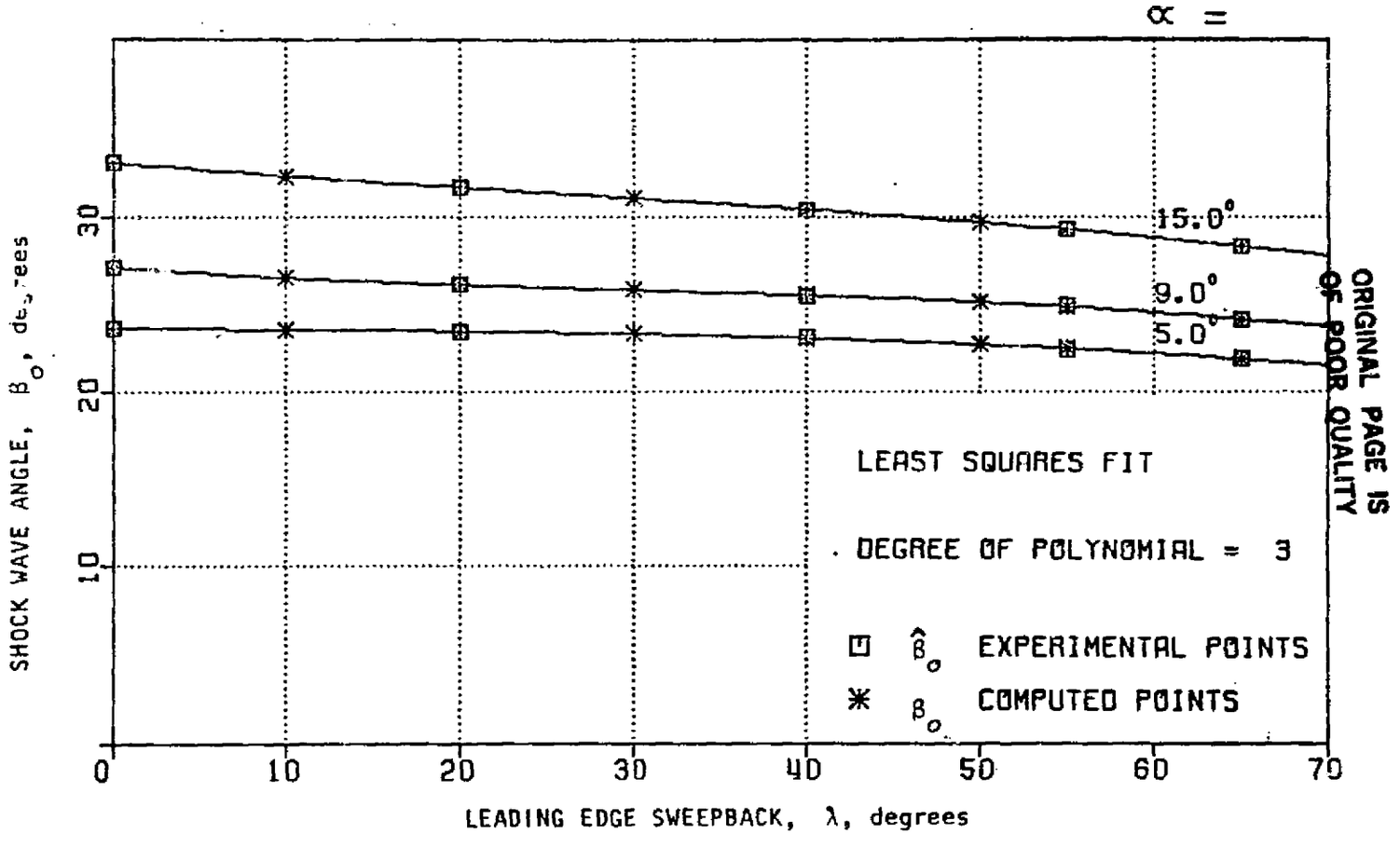

Figure 17. Experimental and interpolated shock wave angles at the centerline of delta wings at $M_\infty = 2.95$.

$\alpha_f = 5^o$

λ_f, deg	0	10	20	30	40	50	55	65
$\hat{\beta}_o$, deg	23.66	-	23.49	-	23.10	-	22.45	21.98
β_o, deg	23.59	23.52	23.43	23.28	23.04	22.69	22.46	21.88
$(\hat{\beta}_o - \beta_o)$, deg	+0.07	-	+0.06	-	+0.06	-	-0.01	+0.1

$\alpha_f = 9^o$

λ_f, deg	0	10	20	30	40	50	55	65
$\hat{\beta}_o$, deg	27.19	-	26.19	-	25.40	-	24.92	24.13
β_o, deg	27.11	26.48	26.07	25.76	25.47	25.09	24.83	24.13
$(\hat{\beta}_o - \beta_o)$, deg	+0.08	-	+0.12	-	-0.07	-	+0.09	0.0

$\alpha_f = 15^o$

λ_f, deg	0	10	20	30	40	50	55	65
$\hat{\beta}_o$, deg	33.11	-	31.79	-	30.45	-	29.37	28.35
β_o, deg	33.10	32.35	31.69	31.07	30.42	29.69	29.28	28.31
$(\hat{\beta}_o - \beta_o)$, deg	+0.01	-	+0.1	-	+0.03	-	+0.09	+0.04

α_f, deg	λ_f, deg	β_o, deg	β_o', deg	$\frac{\Delta\beta}{\beta_o'}$	α_f', deg	$\frac{\Delta\alpha_f}{\alpha_f'}$
5	0	23.59	23.49	0.004	5.13	0.026
9	0	27.11	26.85	0.01	9.29	0.032
15	0	33.10	32.62	0.015	15.46	0.03

Figure 18. Summary of experimental and interpolated values of β_o.

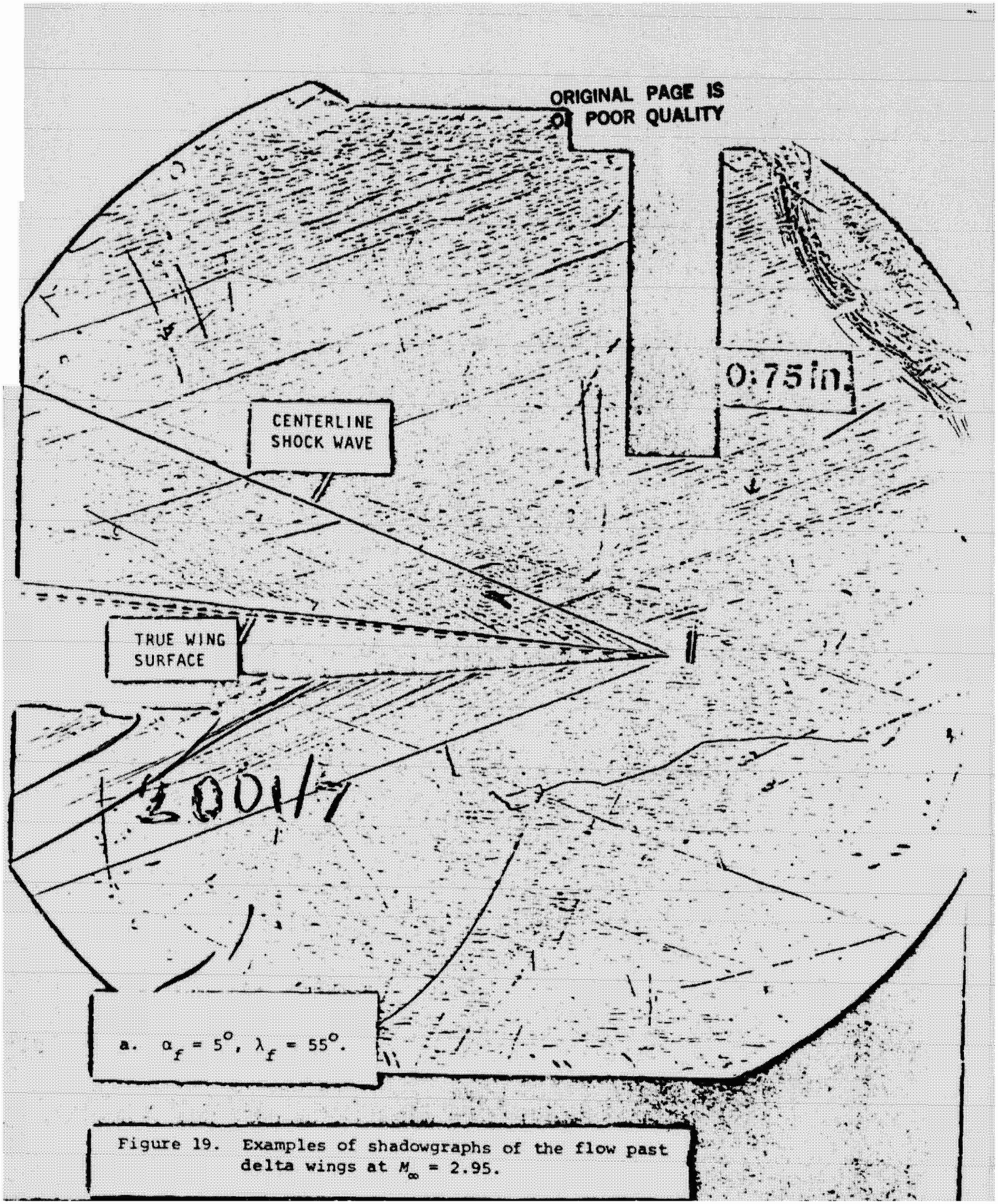

Figure 19. Examples of shadowgraphs of the flow past delta wings at $M_\infty = 2.95$.

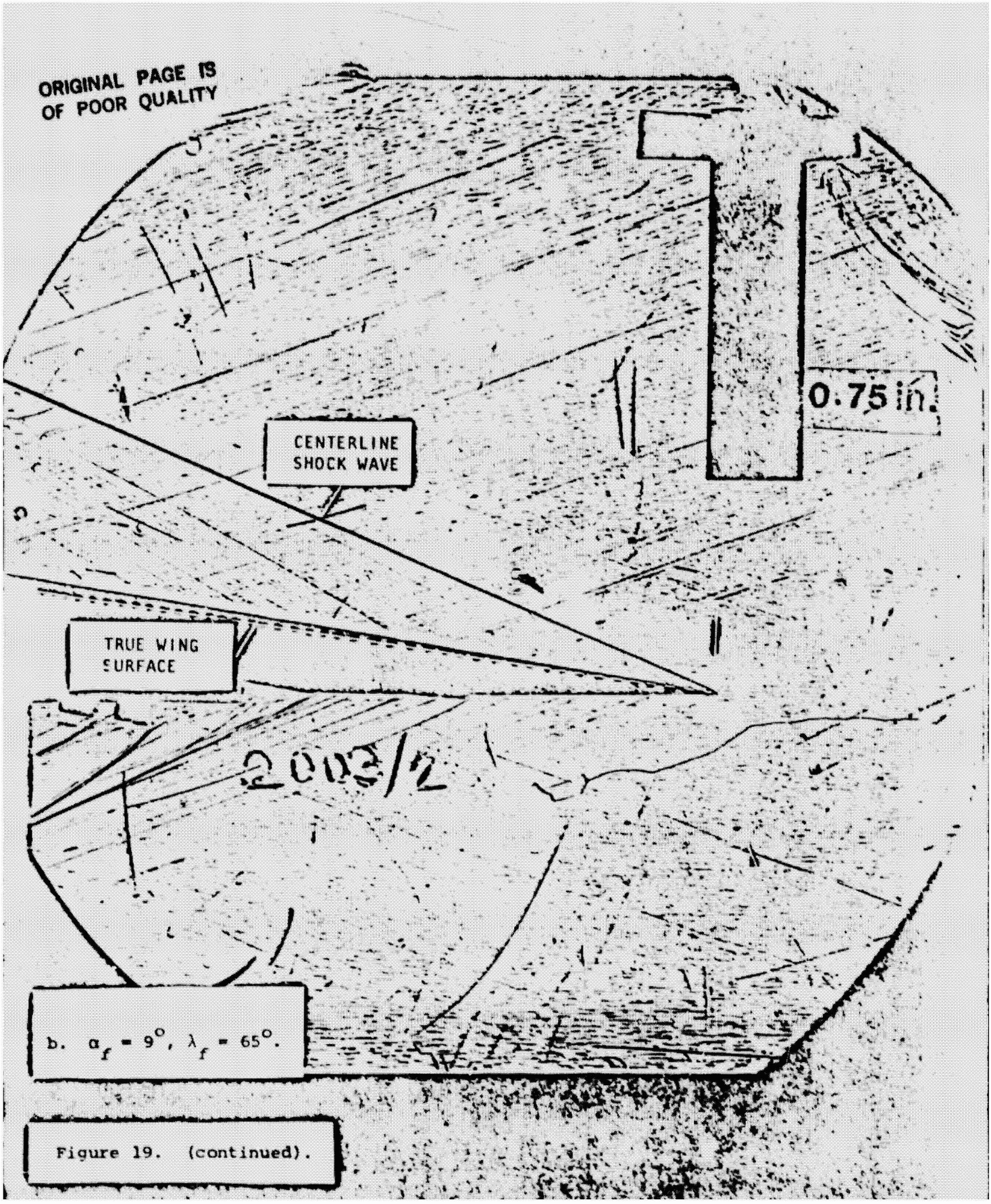

b. $\alpha_f = 9^\circ$, $\lambda_f = 65^\circ$.

Figure 19. (continued).

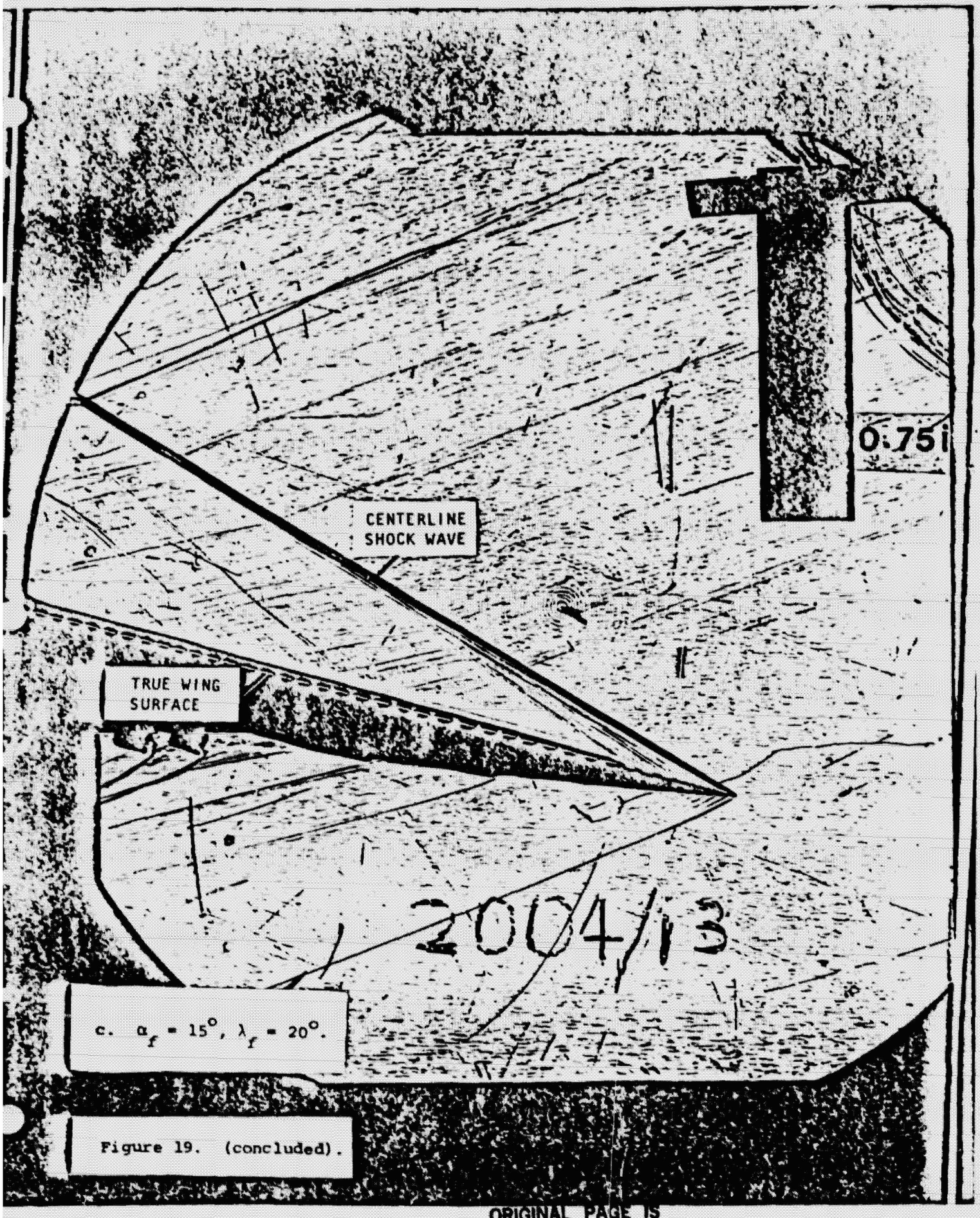

c. $\alpha_f = 15^\circ$, $\lambda_f = 20^\circ$.

Figure 19. (concluded).

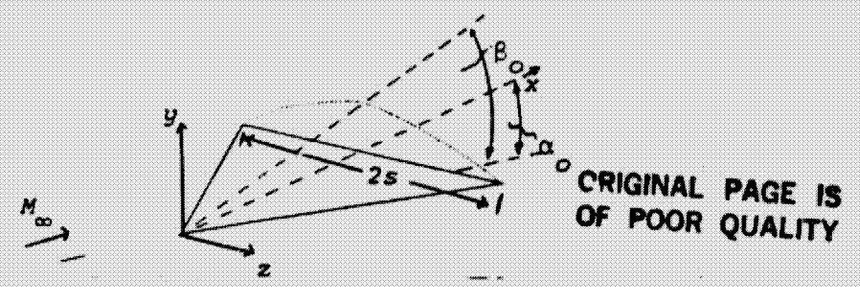

direction of view

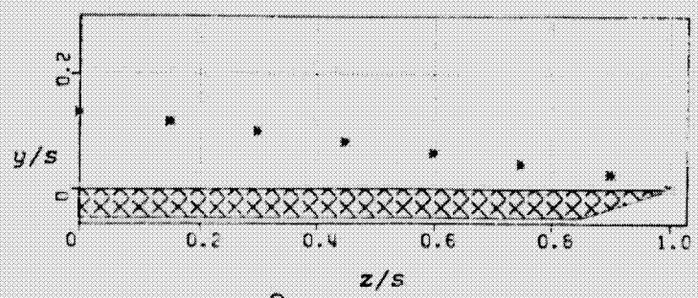

i. $\lambda_f = 20^\circ$

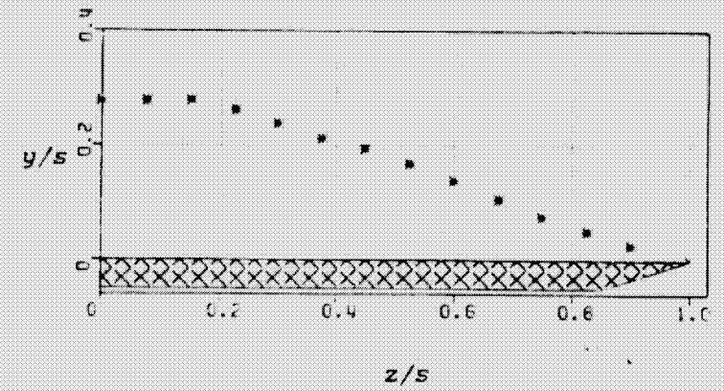

ii. $\lambda_f = 40^\circ$

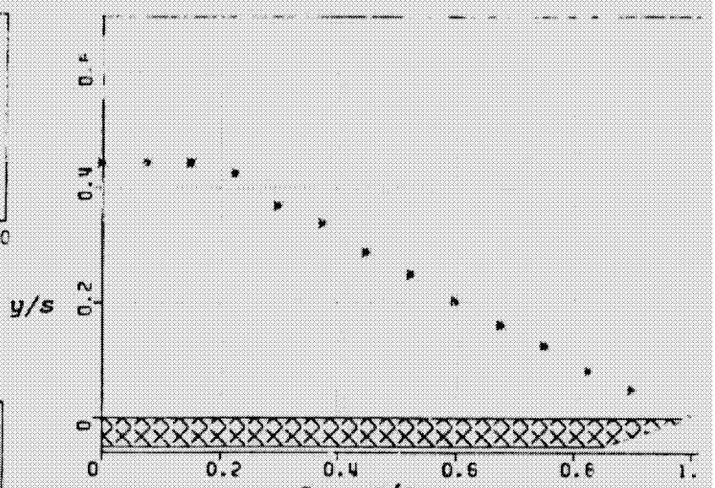

iii. $\lambda_f = 55^\circ$

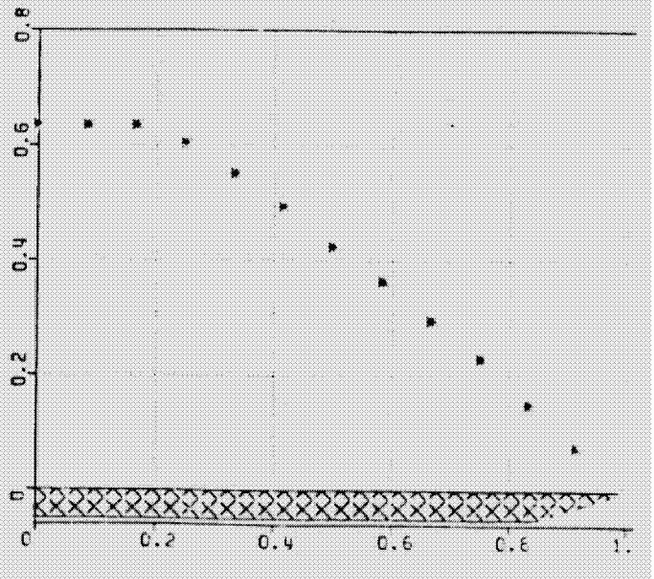

iv. $\lambda_f = 65^\circ$

a. $\alpha_f = 5^\circ$

Figure 20. Shock wave envelope on the windward side of delta wings at incidence at $M_\infty = 2.95$.

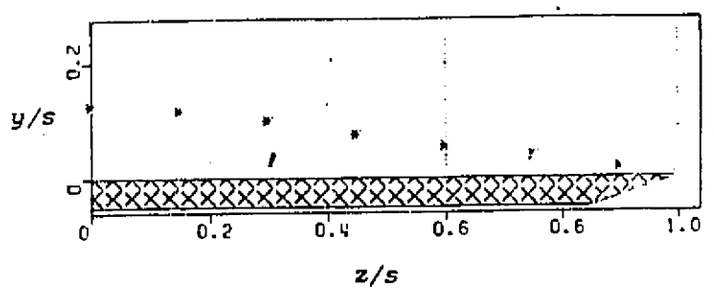

i. $\lambda_f = 20^\circ$

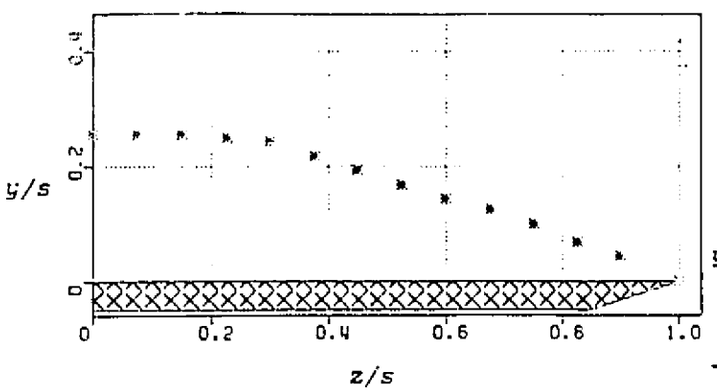

ii. $\lambda_f = 40^\circ$

b. $\alpha_f = 9^\circ$

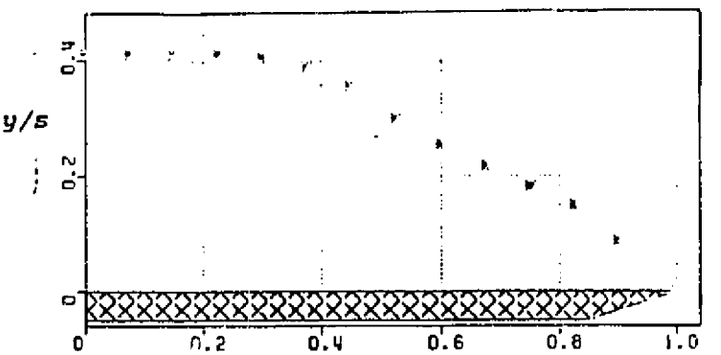

iii. $\lambda_f = 55^\circ$

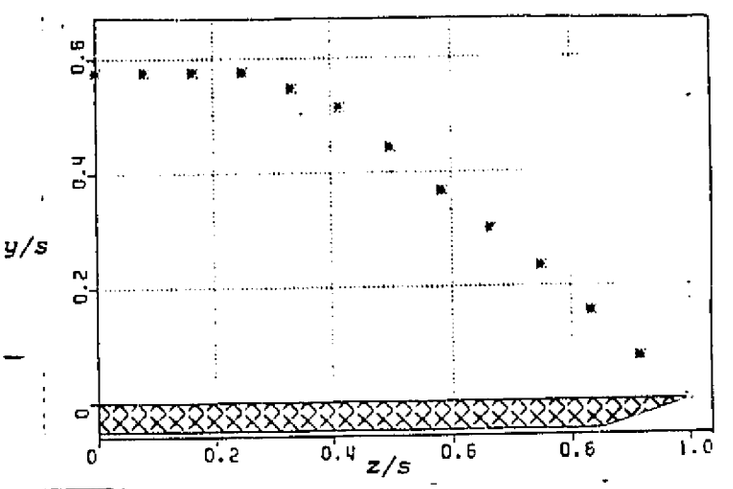

iv. $\lambda_f = 65^\circ$

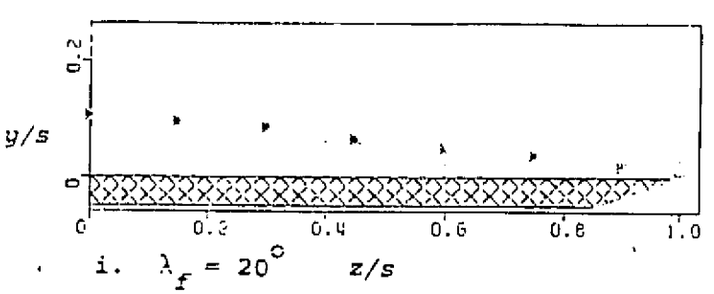

i. $\lambda_f = 20^\circ$

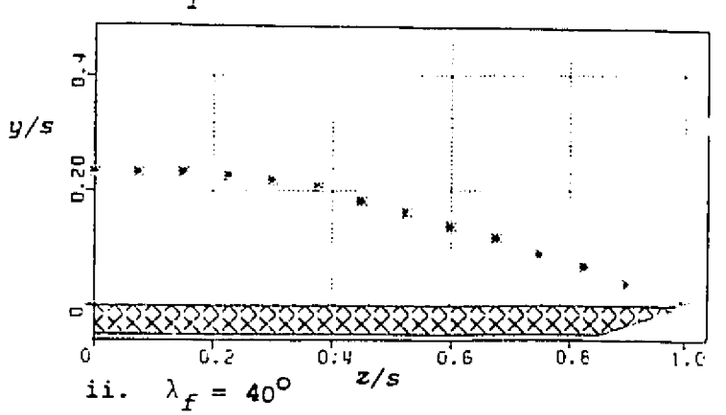

ii. $\lambda_f = 40^\circ$

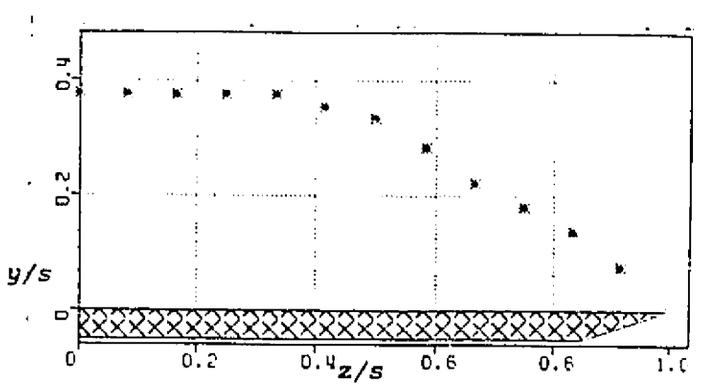

iii. $\lambda_f = 55^\circ$

c. $\alpha_f = 15^\circ$

Figure 20. (concluded).

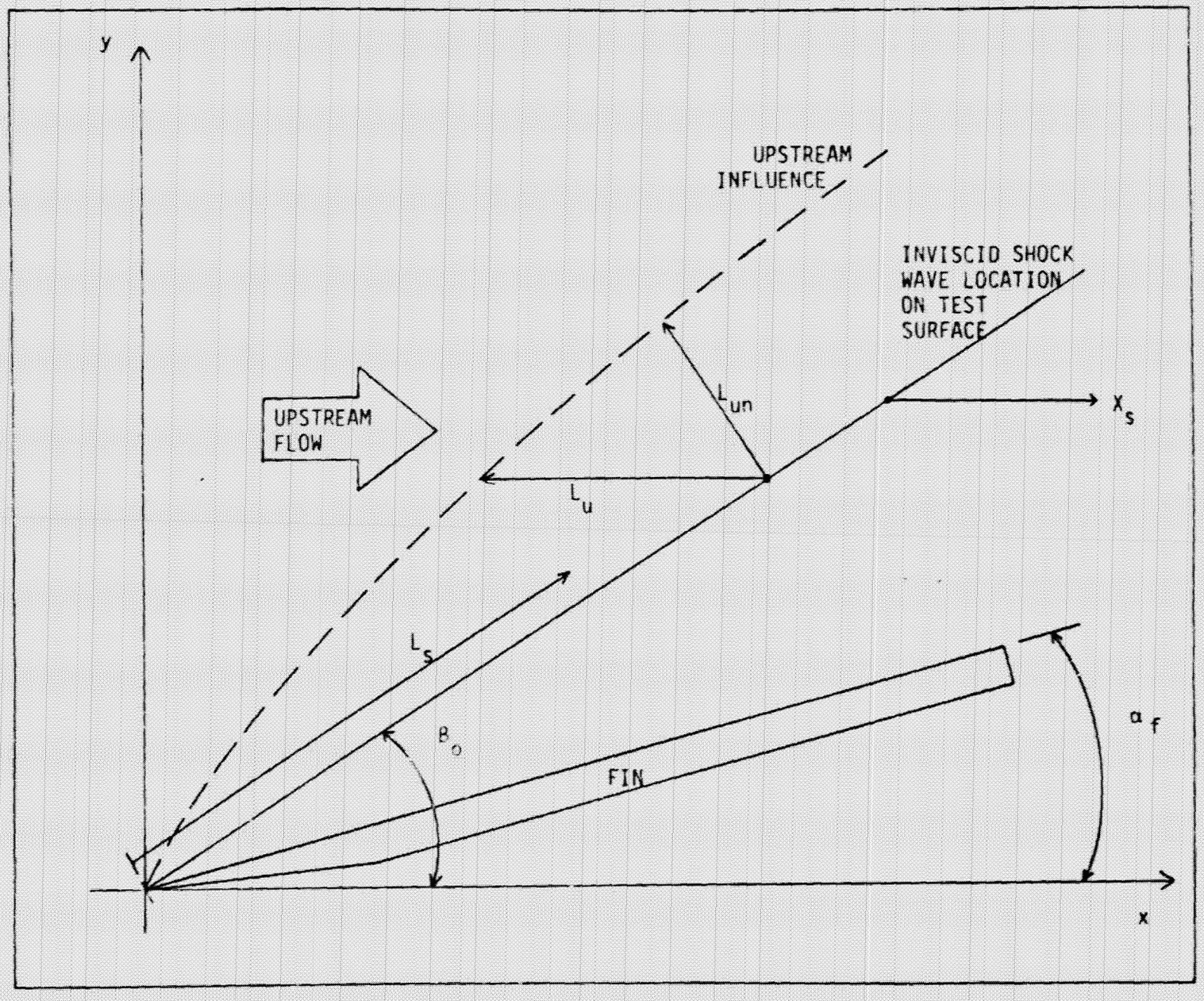

Figure 21. The coordinate system and the upstream influence length.

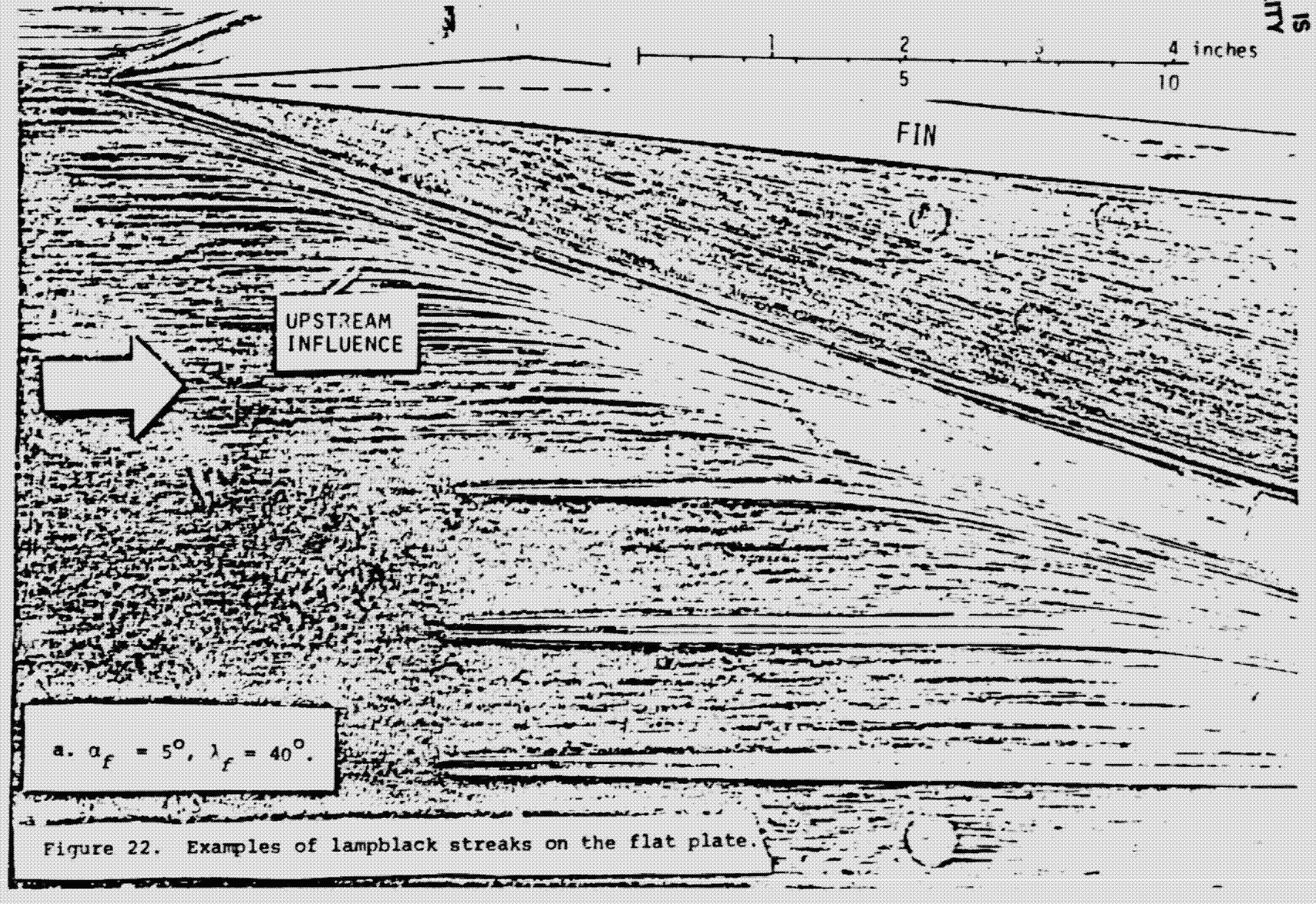

Figure 22. Examples of lampblack streaks on the flat plate.

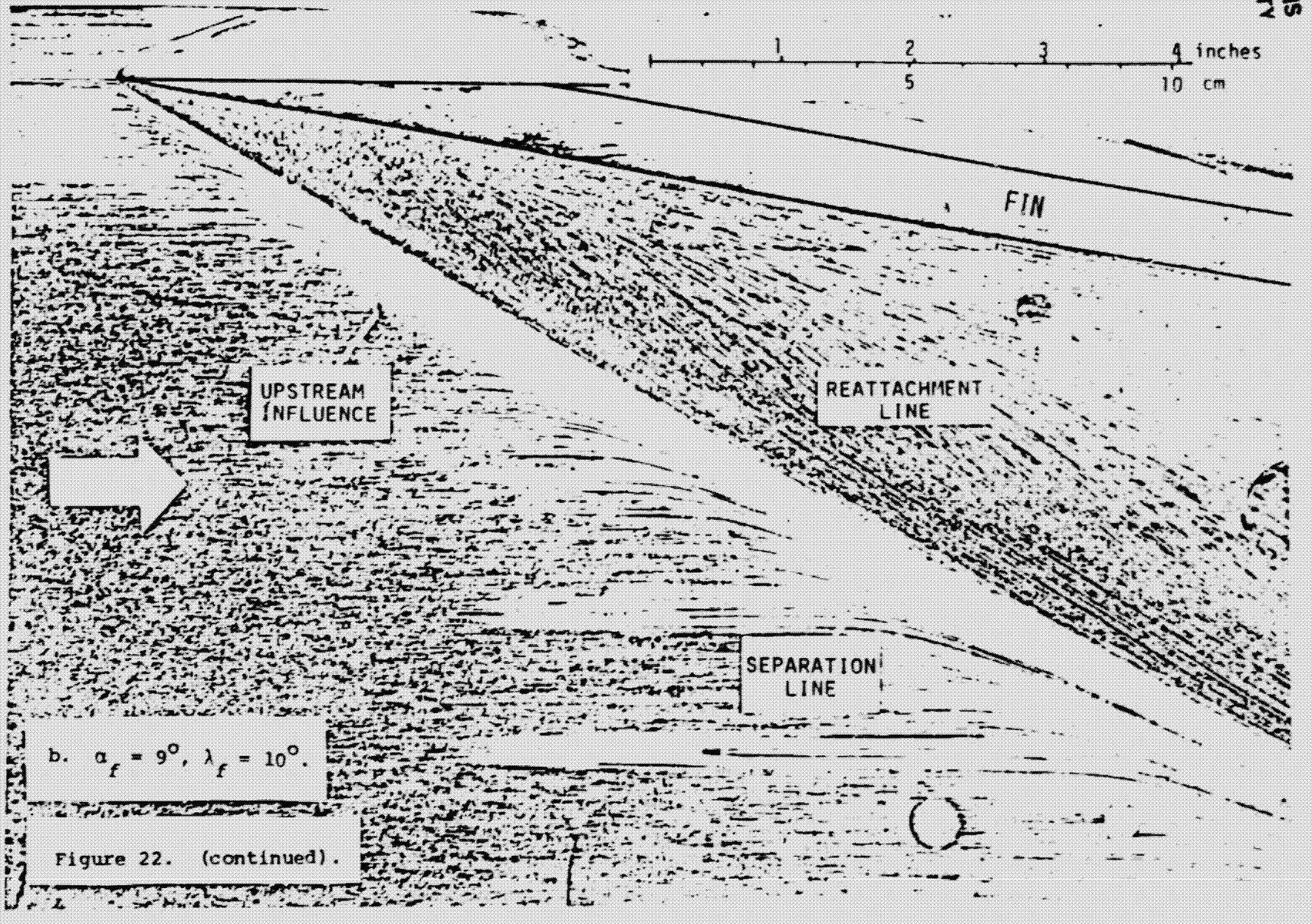

b. $\alpha_f = 9^\circ$, $\lambda_f = 10^\circ$.

Figure 22. (continued).

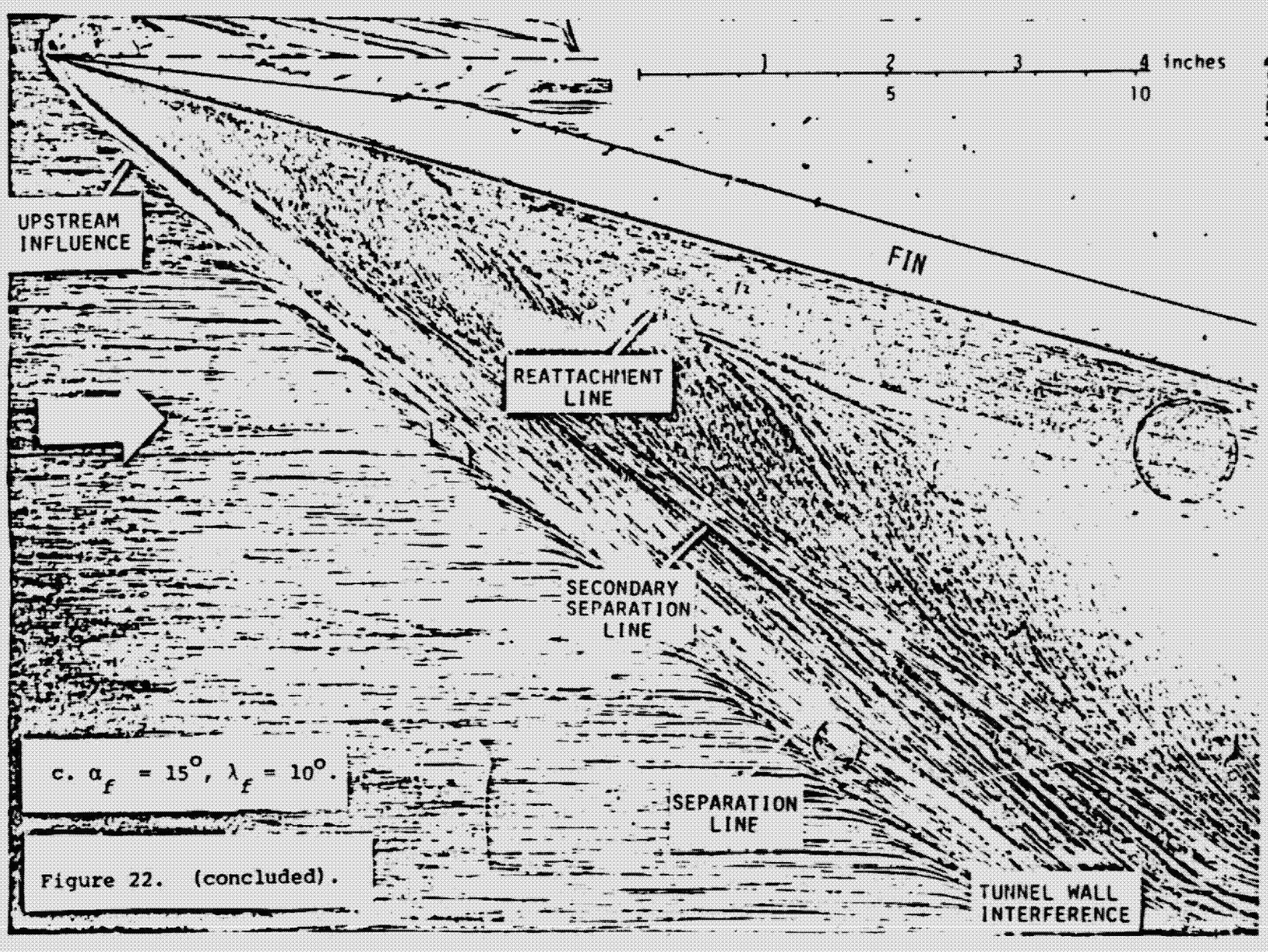

c. $\alpha_f = 15^\circ$, $\lambda_f = 10^\circ$.

Figure 22. (concluded).

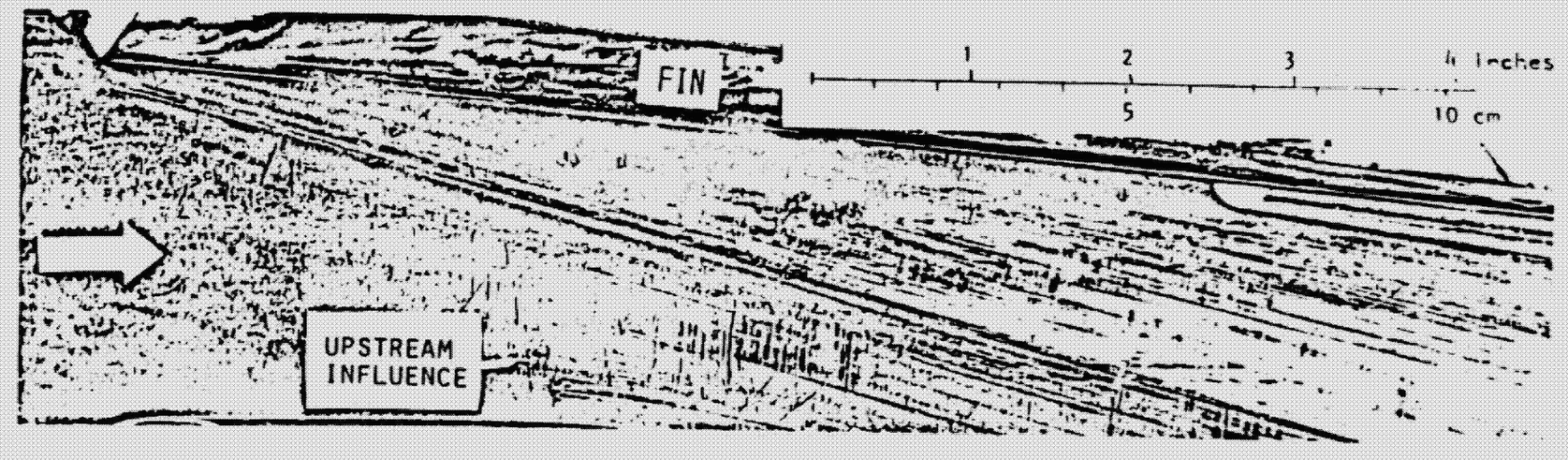

a. $\alpha_f = 5^{\circ}$, $\lambda_f = 30^{\circ}$.

Figure 23. Examples of lampblack streaks on the tunnel floor.

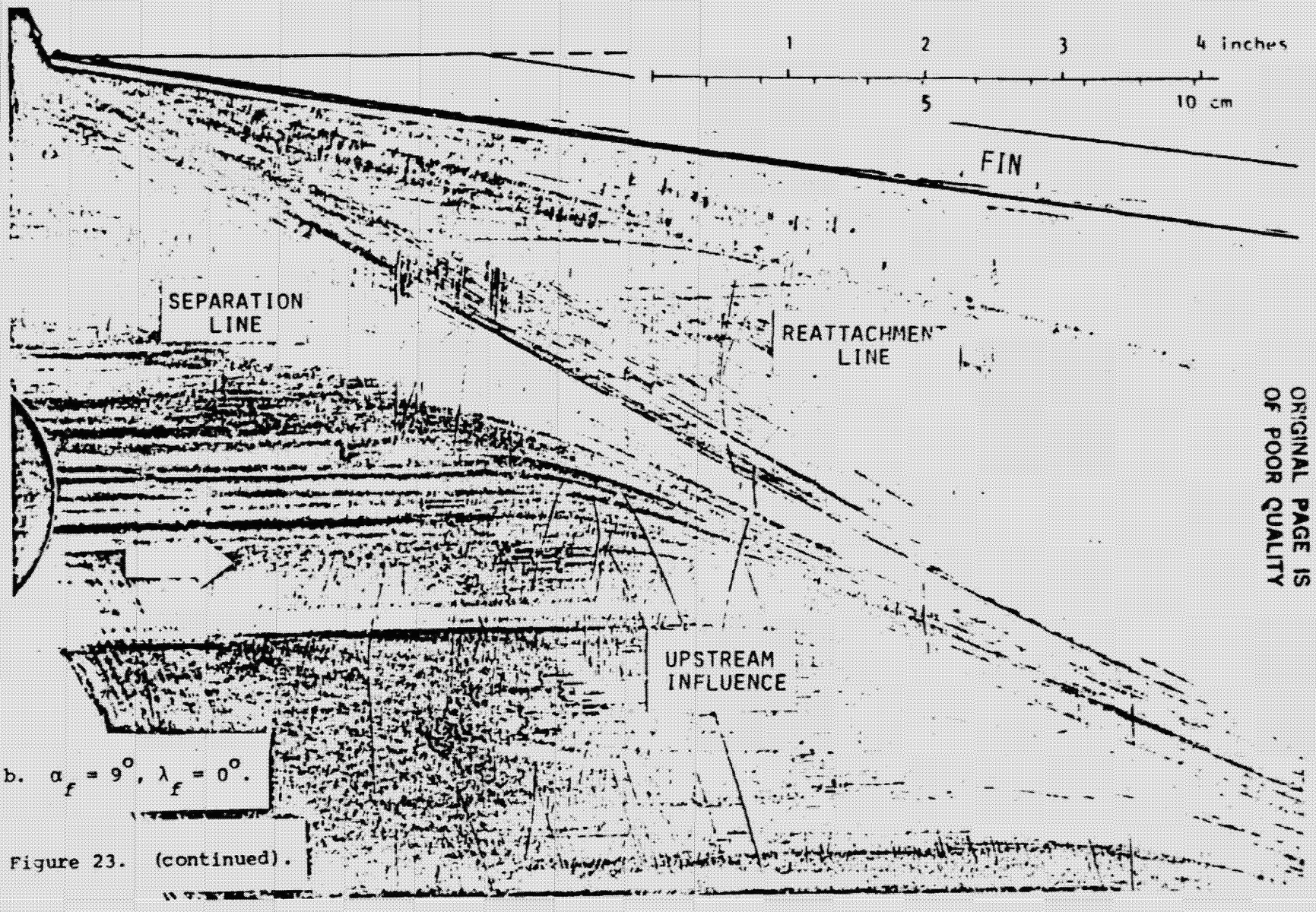

b. $\alpha_f = 9^\circ$, $\lambda_f = 0^\circ$.

Figure 23. (continued).

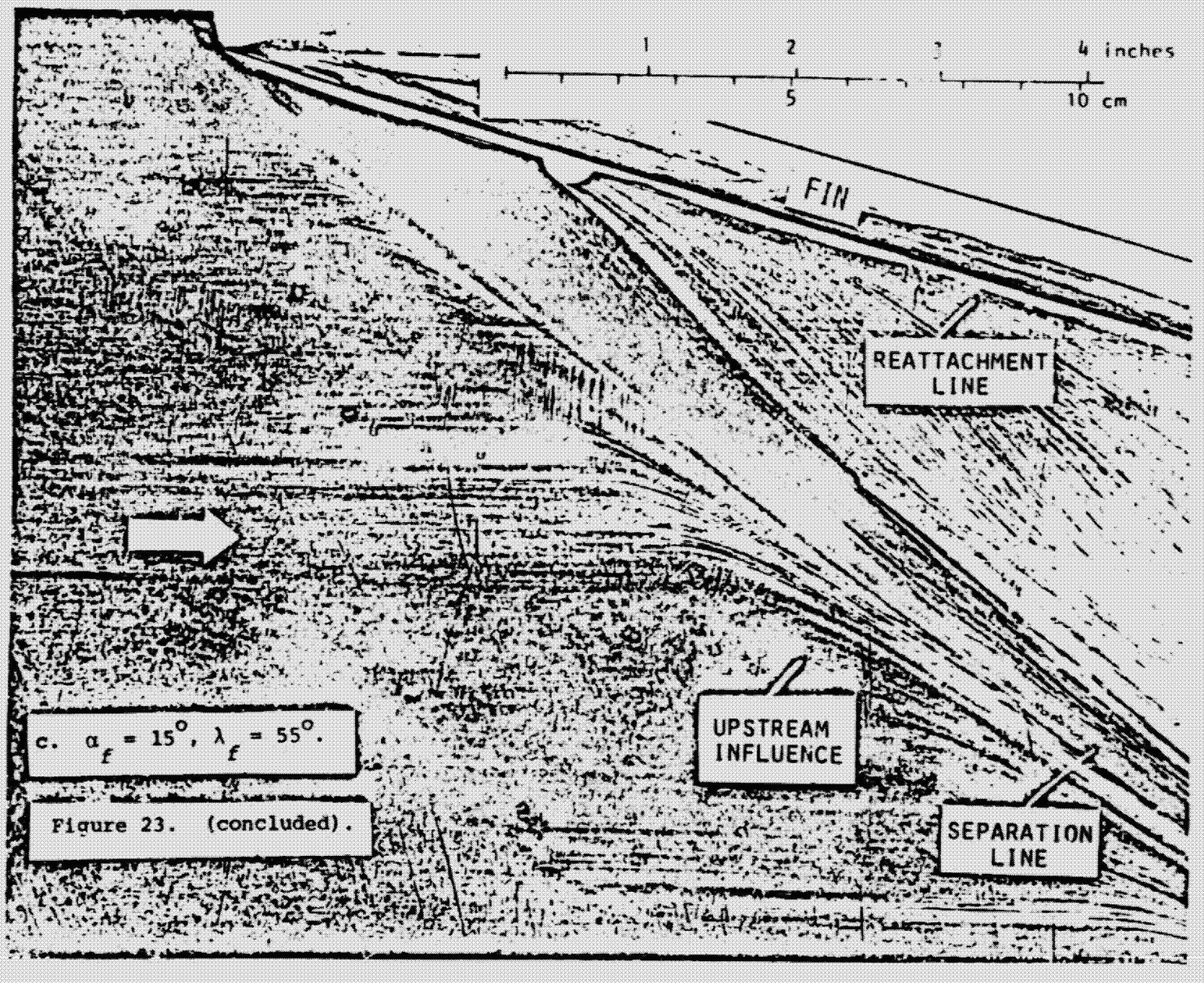

c. $\alpha_f = 15^\circ$, $\lambda_f = 55^\circ$.

Figure 23. (concluded).

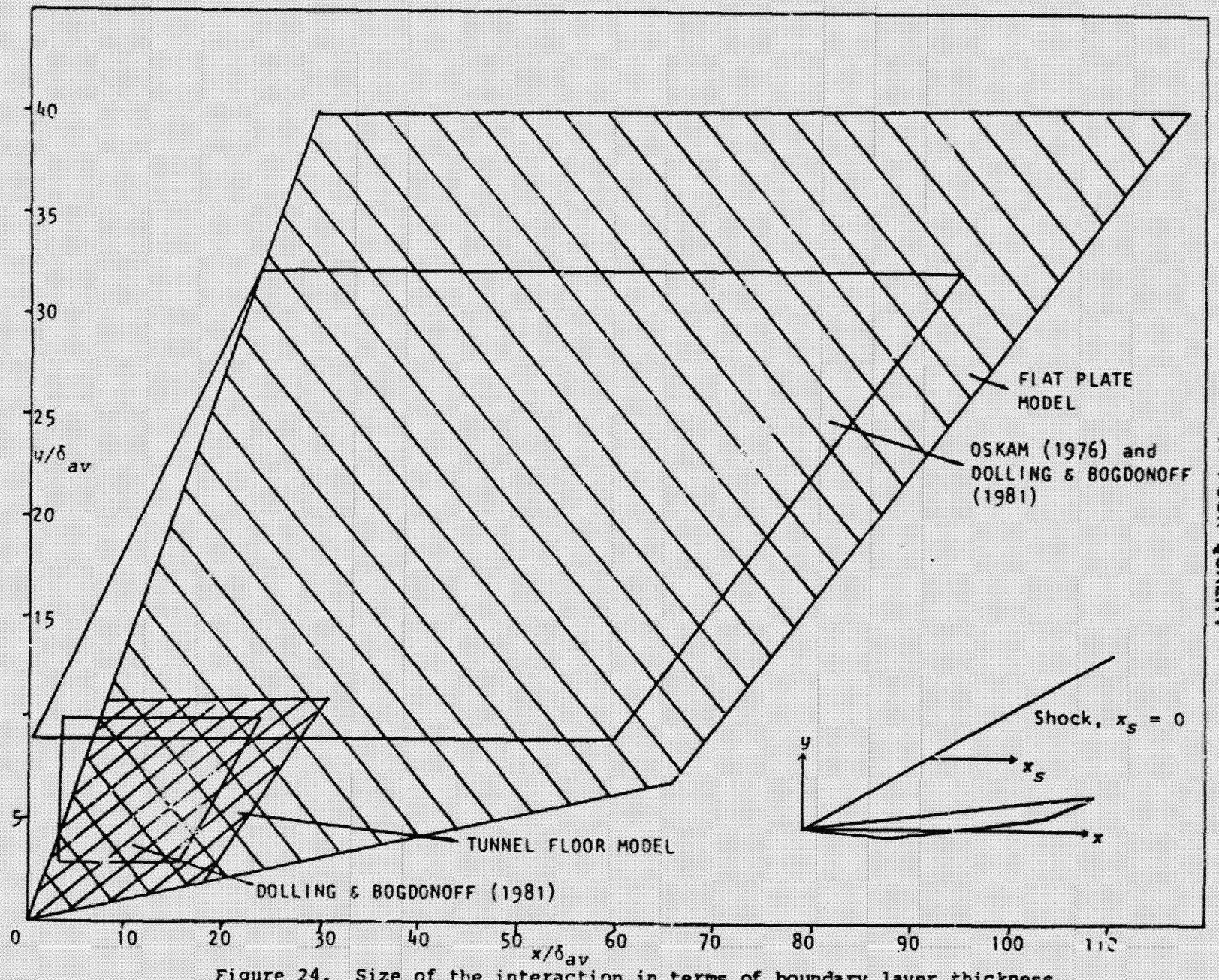

Figure 24. Size of the interaction in terms of boundary layer thickness.

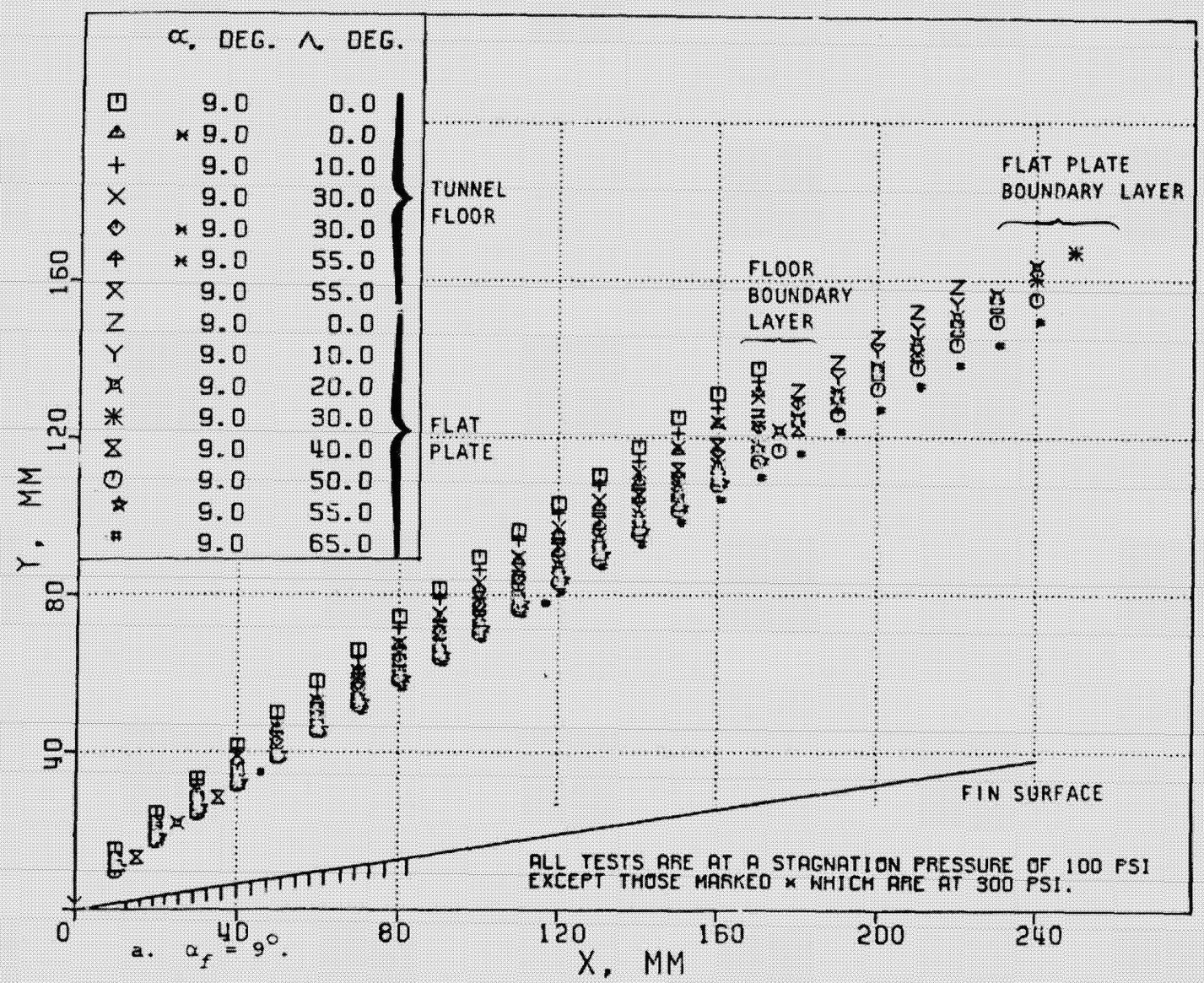

a. $\alpha_f = 9°$.

Figure 25. The upstream influence of sharp fin induced shock wave boundary layer interactions.

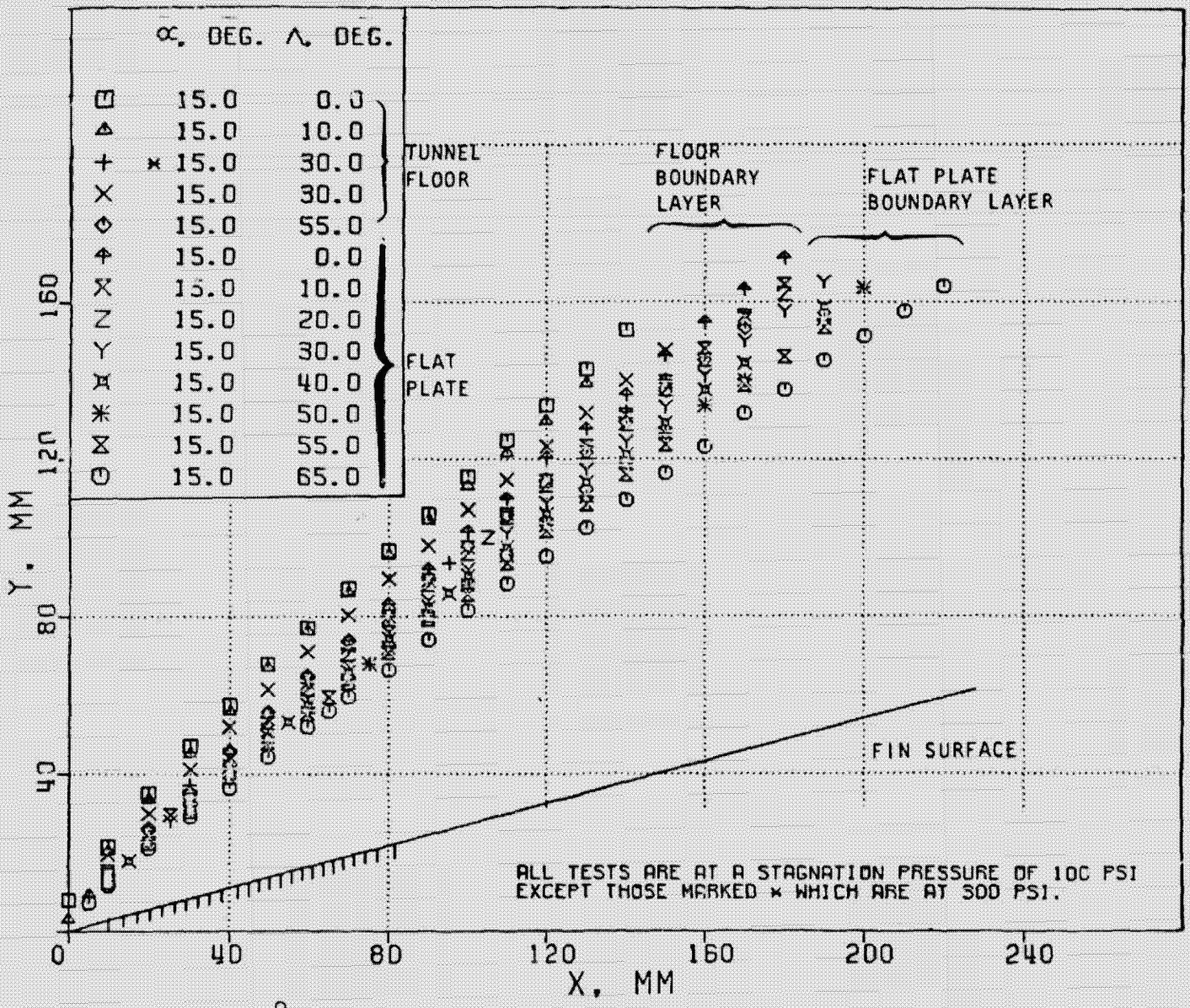

b. $\alpha_f = 15^\circ$

Figure 25. (continued).

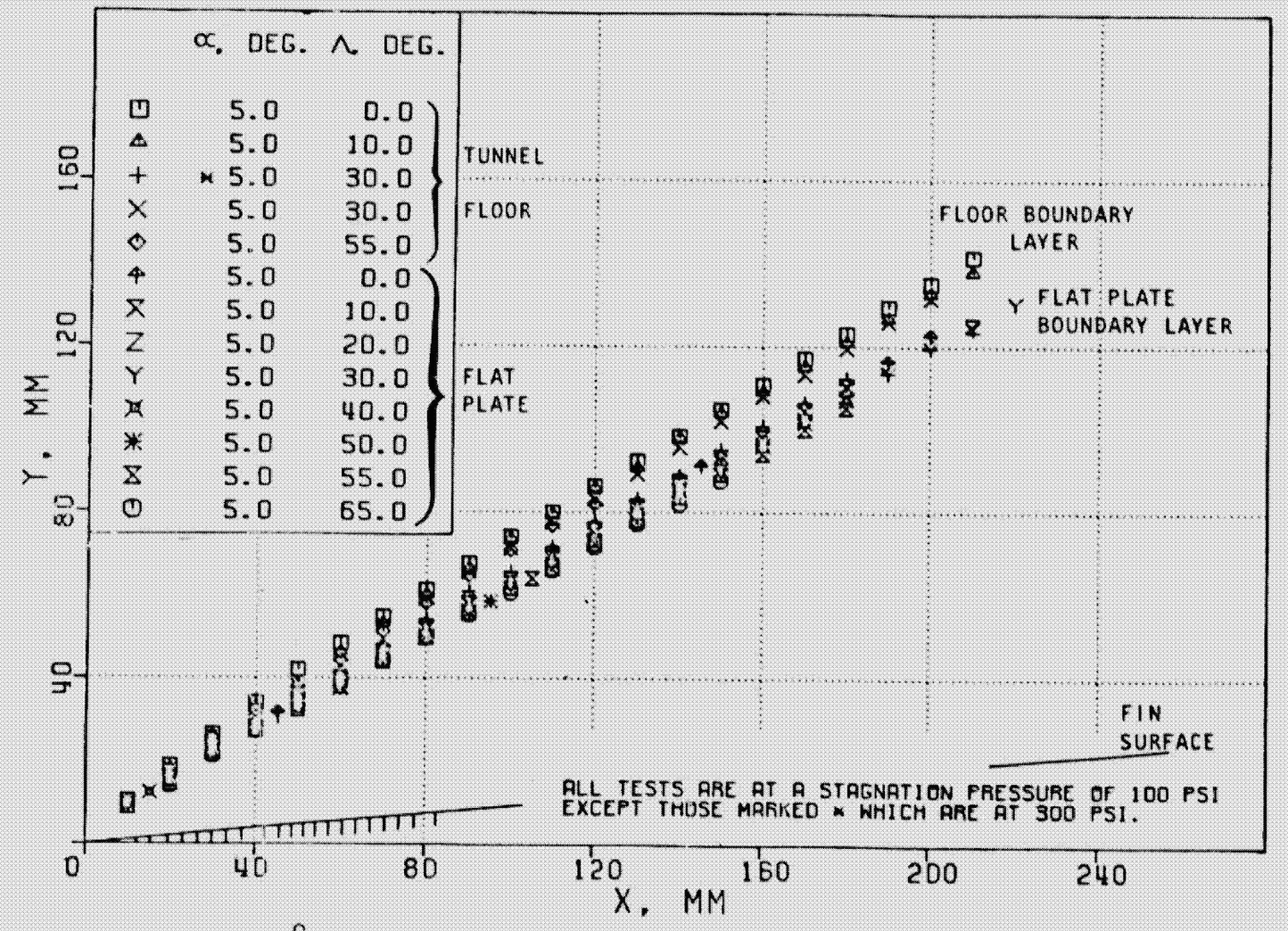

c. $\alpha_f = 5^\circ$

Figure 25. (concluded).

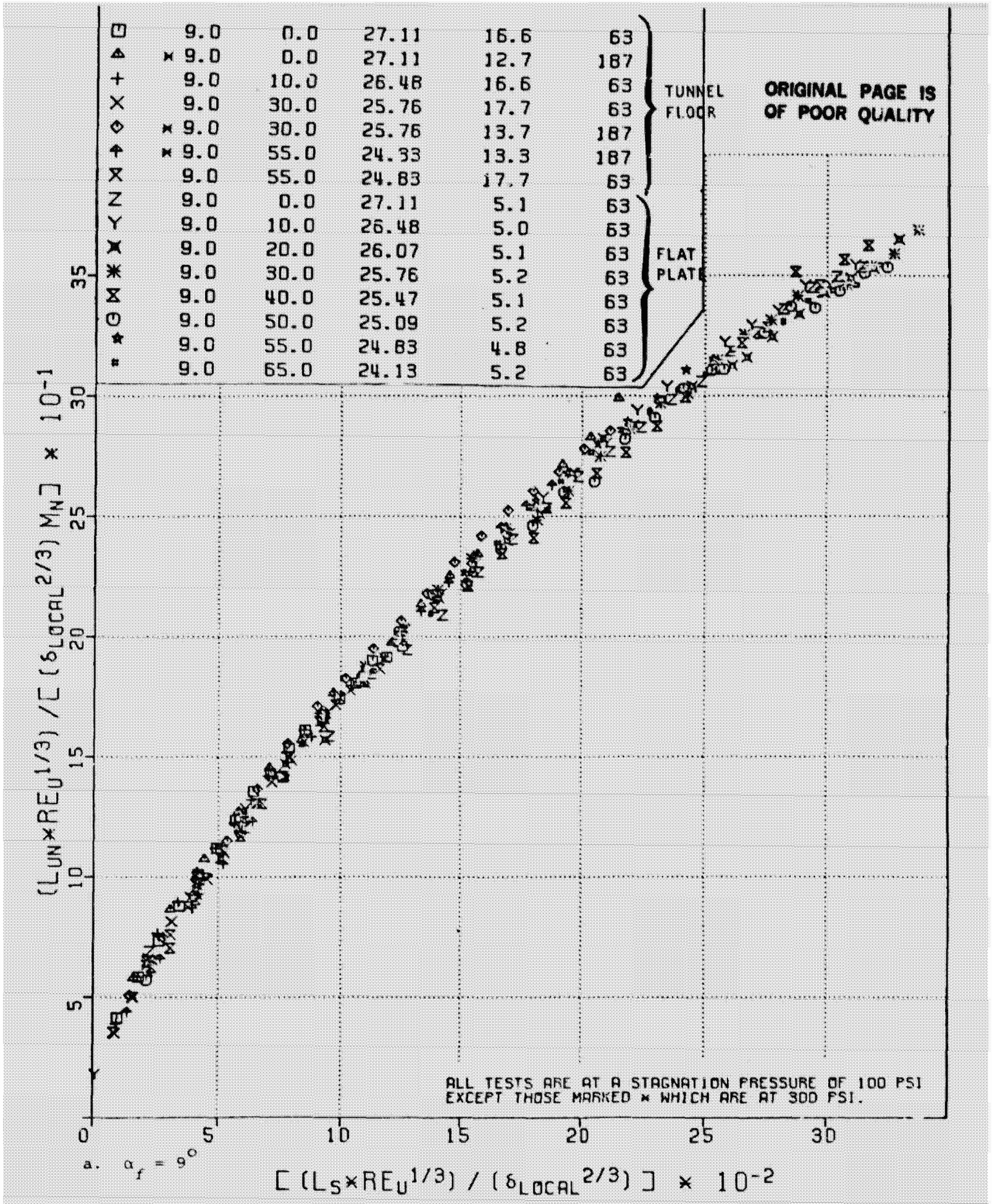

a. $\alpha_f = 9^\circ$

Figure 26. Correlation of the upstream influence.

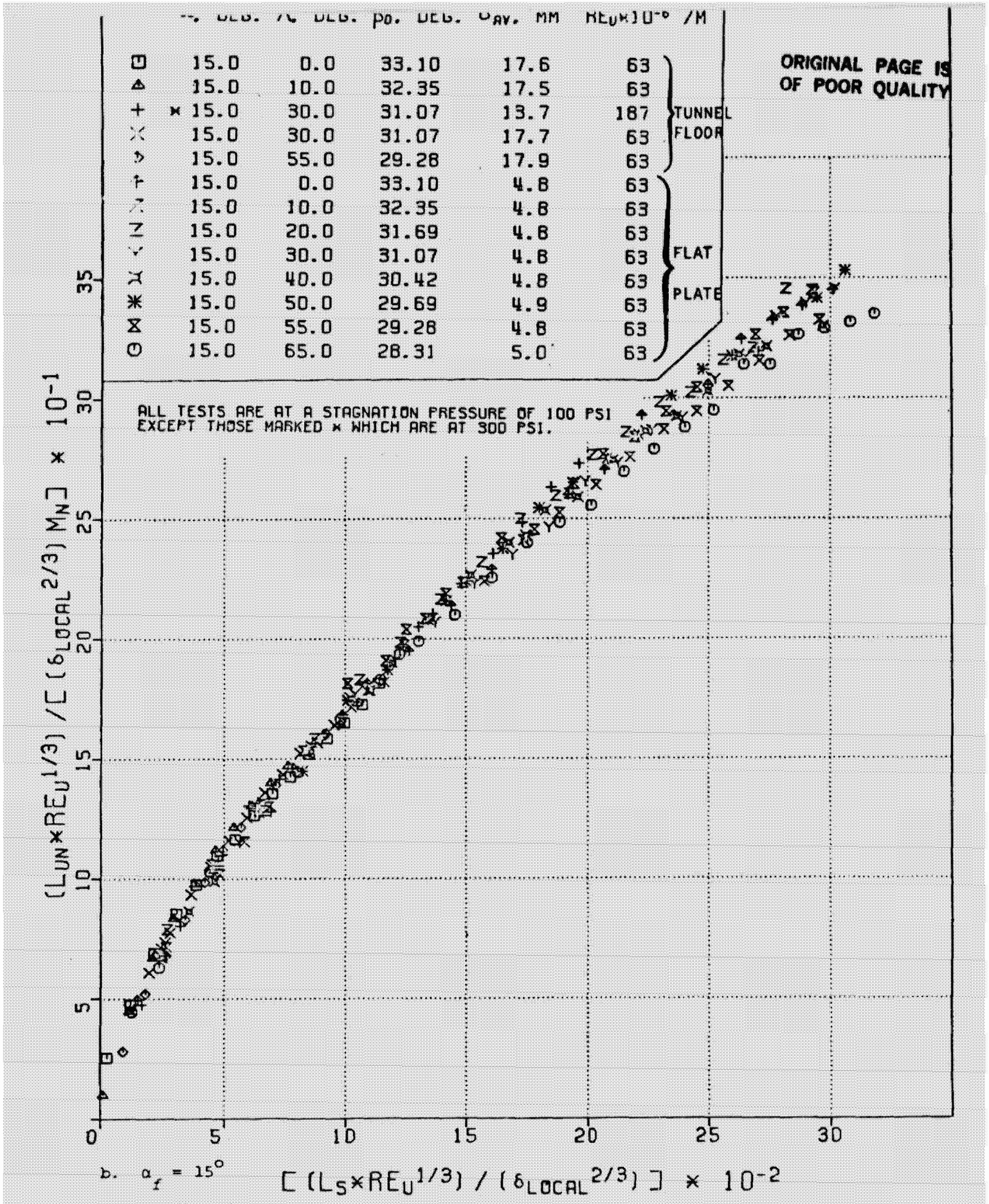

b. $\alpha_f = 15^\circ$

Figure 26. (continued).

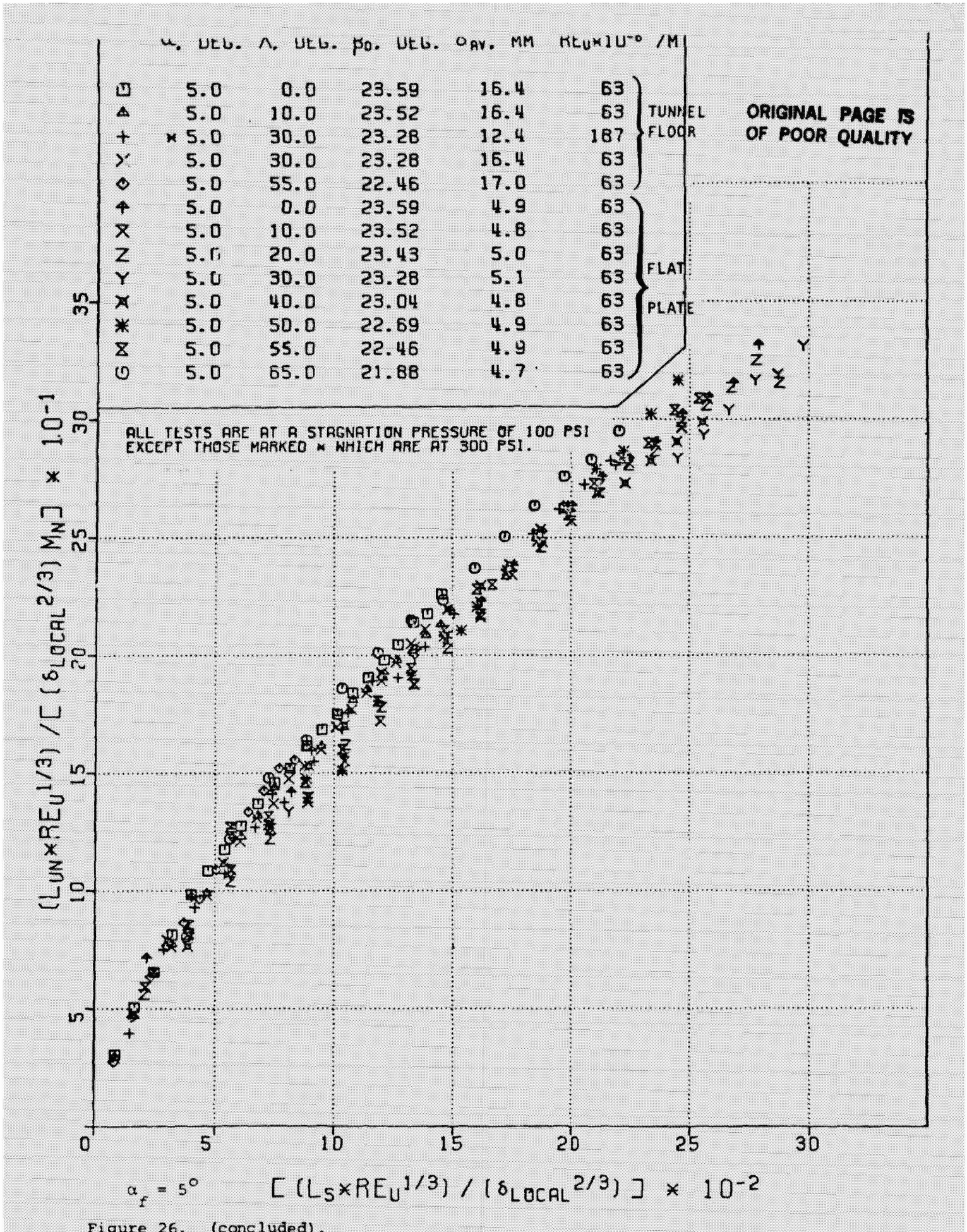

Figure 26. (concluded).

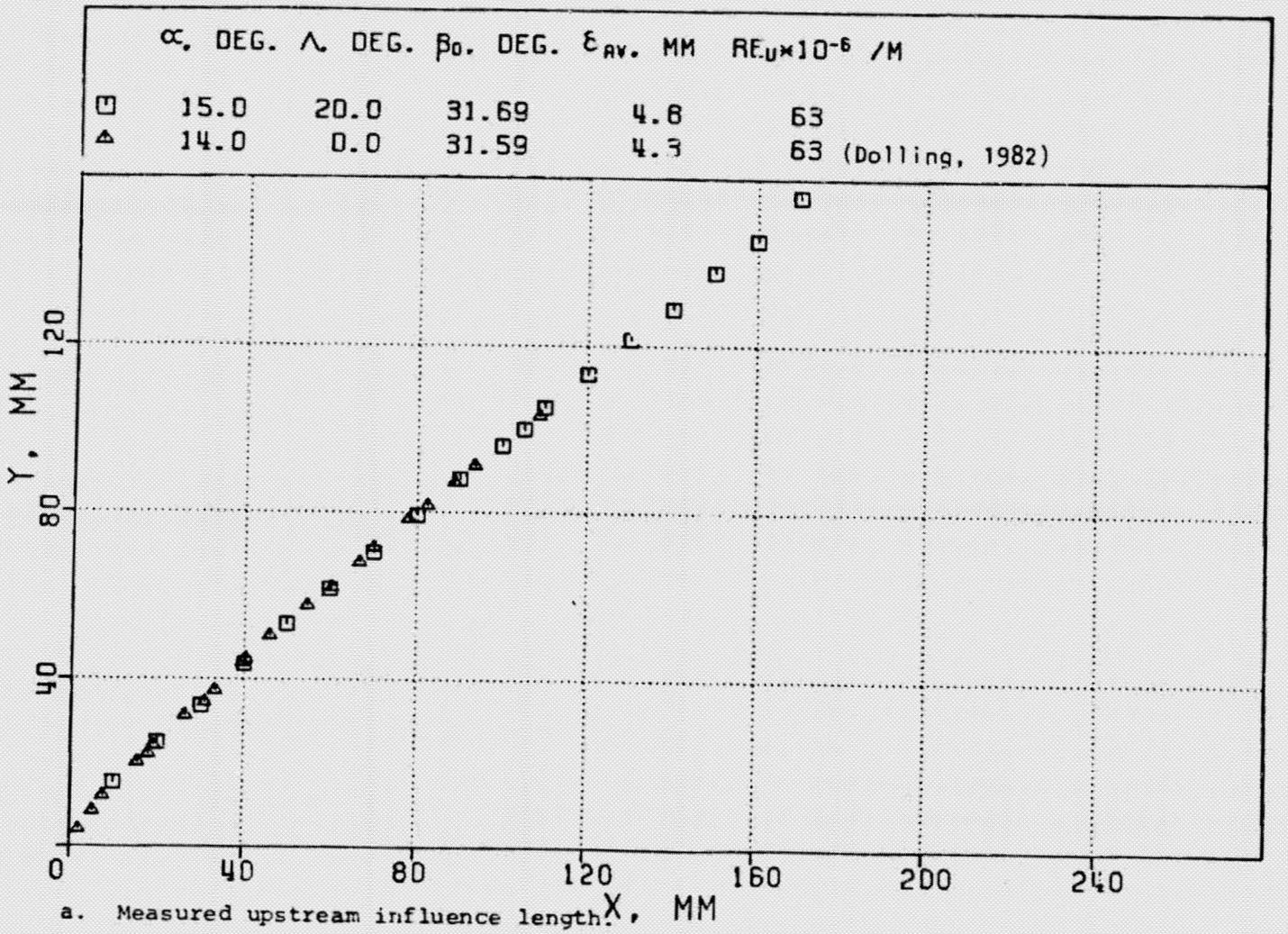

a. Measured upstream influence length.

Figure 27. Comparison of the upstream influence between the interaction due to a fin with a swept leading edge and that due to an upright fin.

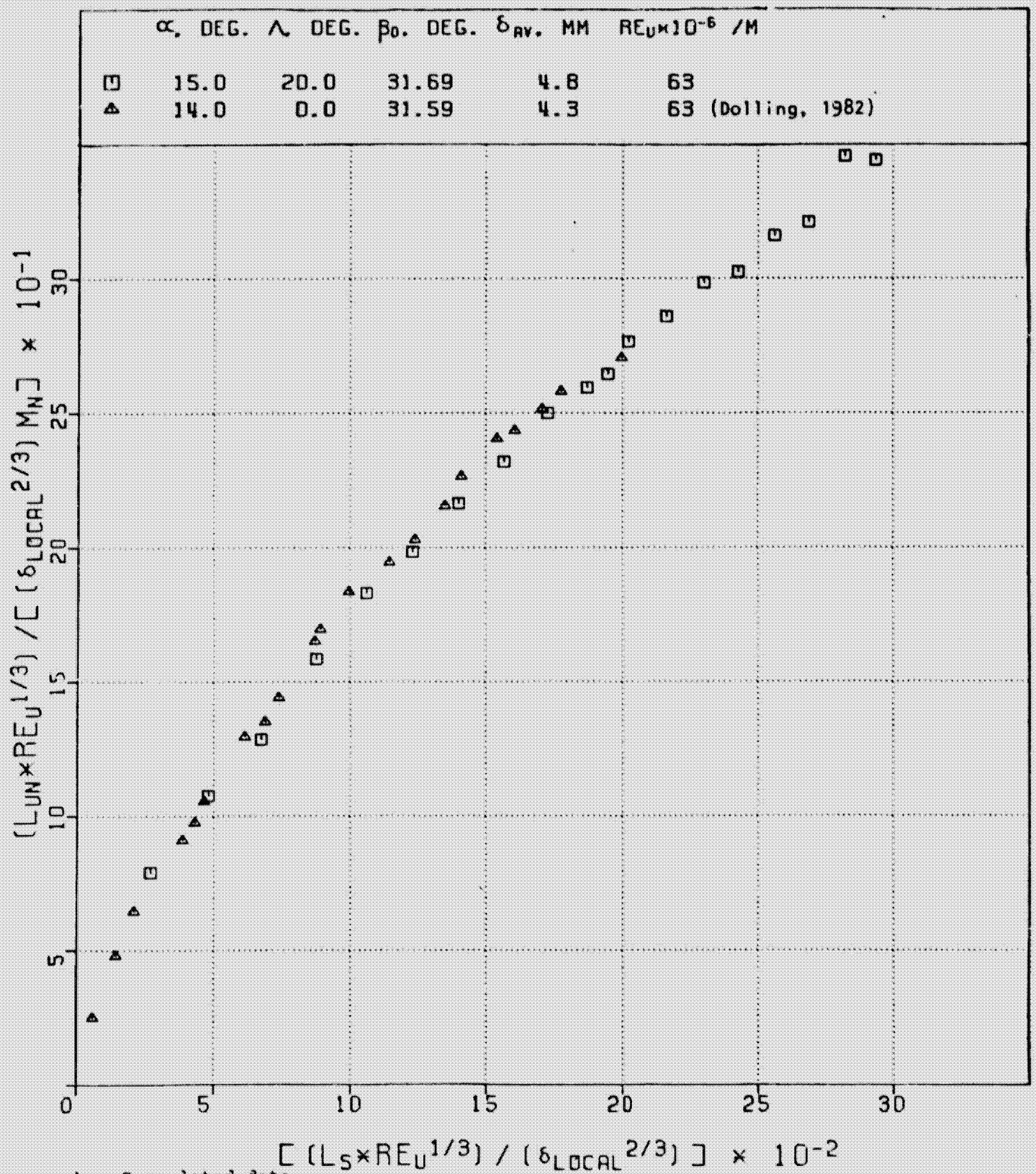

b. Correlated data.
Figure 27. (concluded).

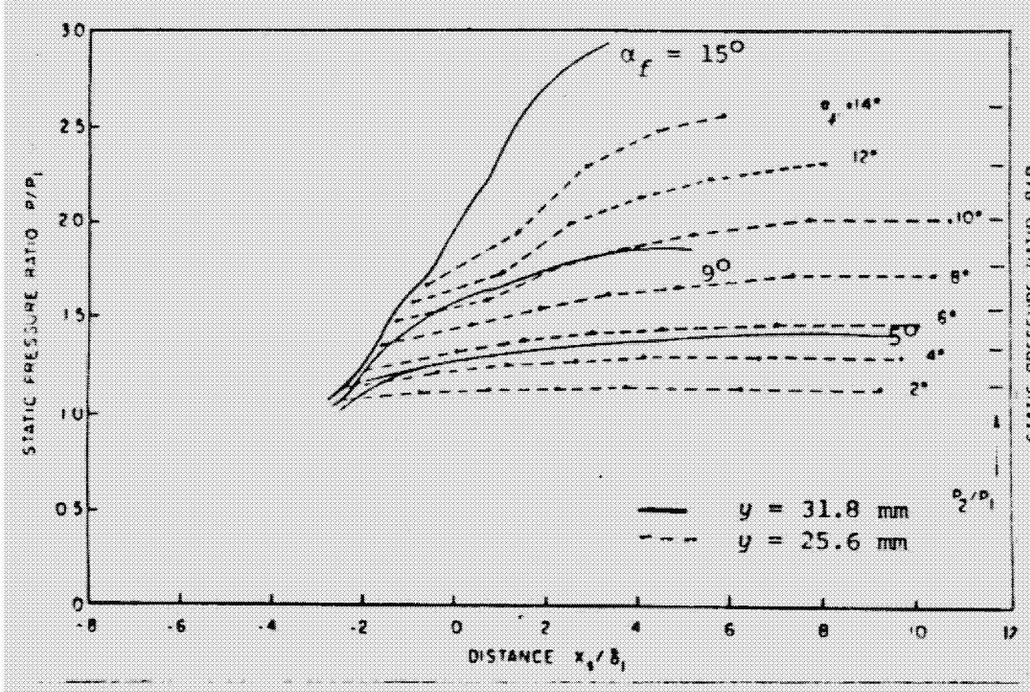

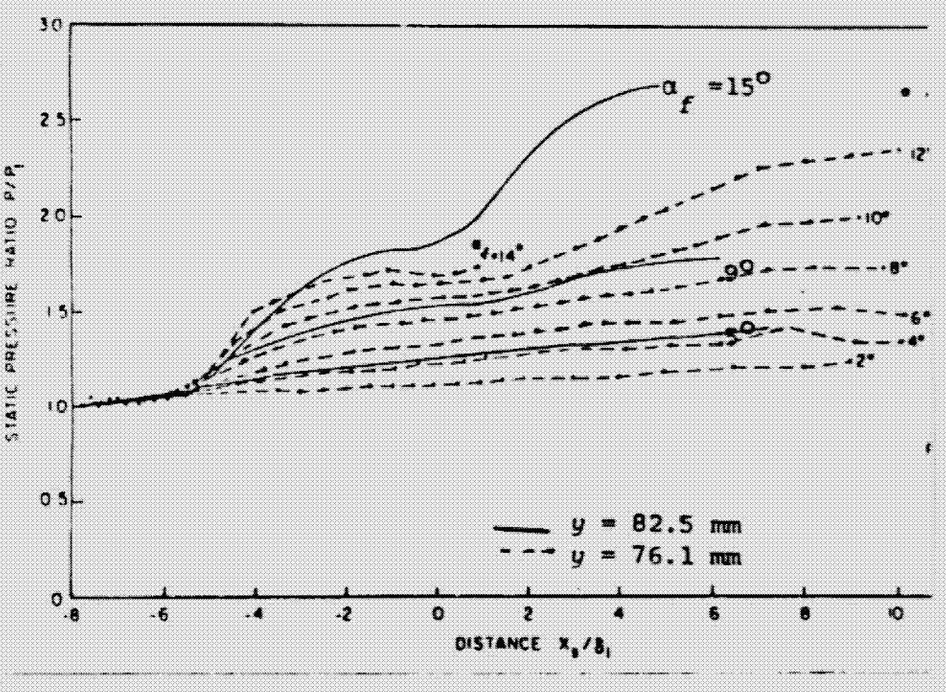

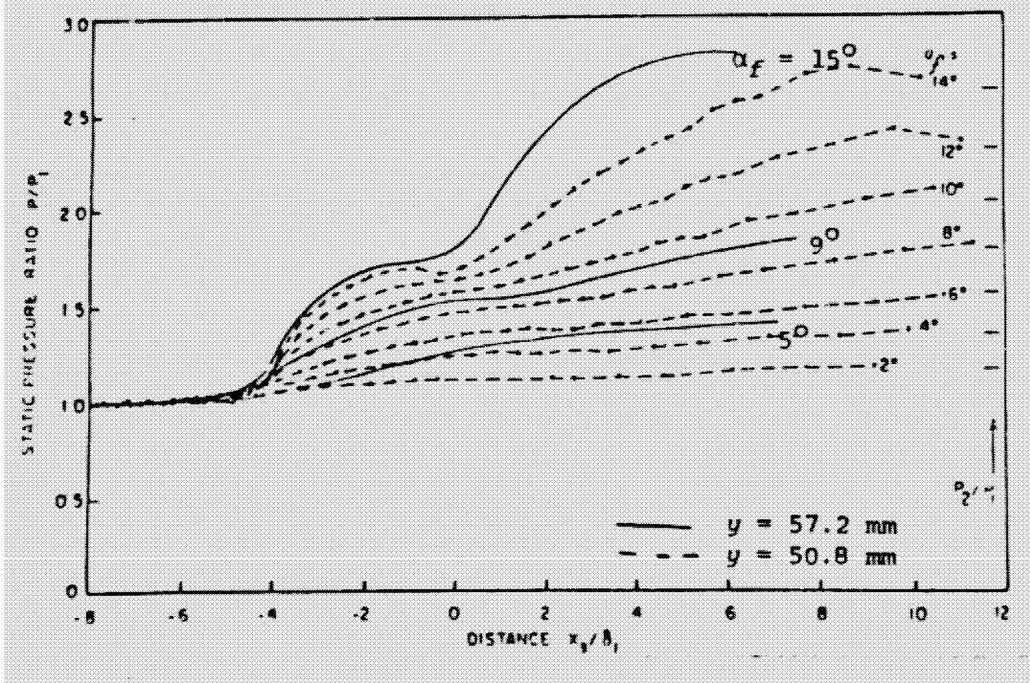

Present experiment, ——
Oskam *et al.* (1975), – – –

Figure 28. Comparison of the pressure distributions obtained with interactions induced by upright fins and those obtained by Oskam *et al.* (1975).

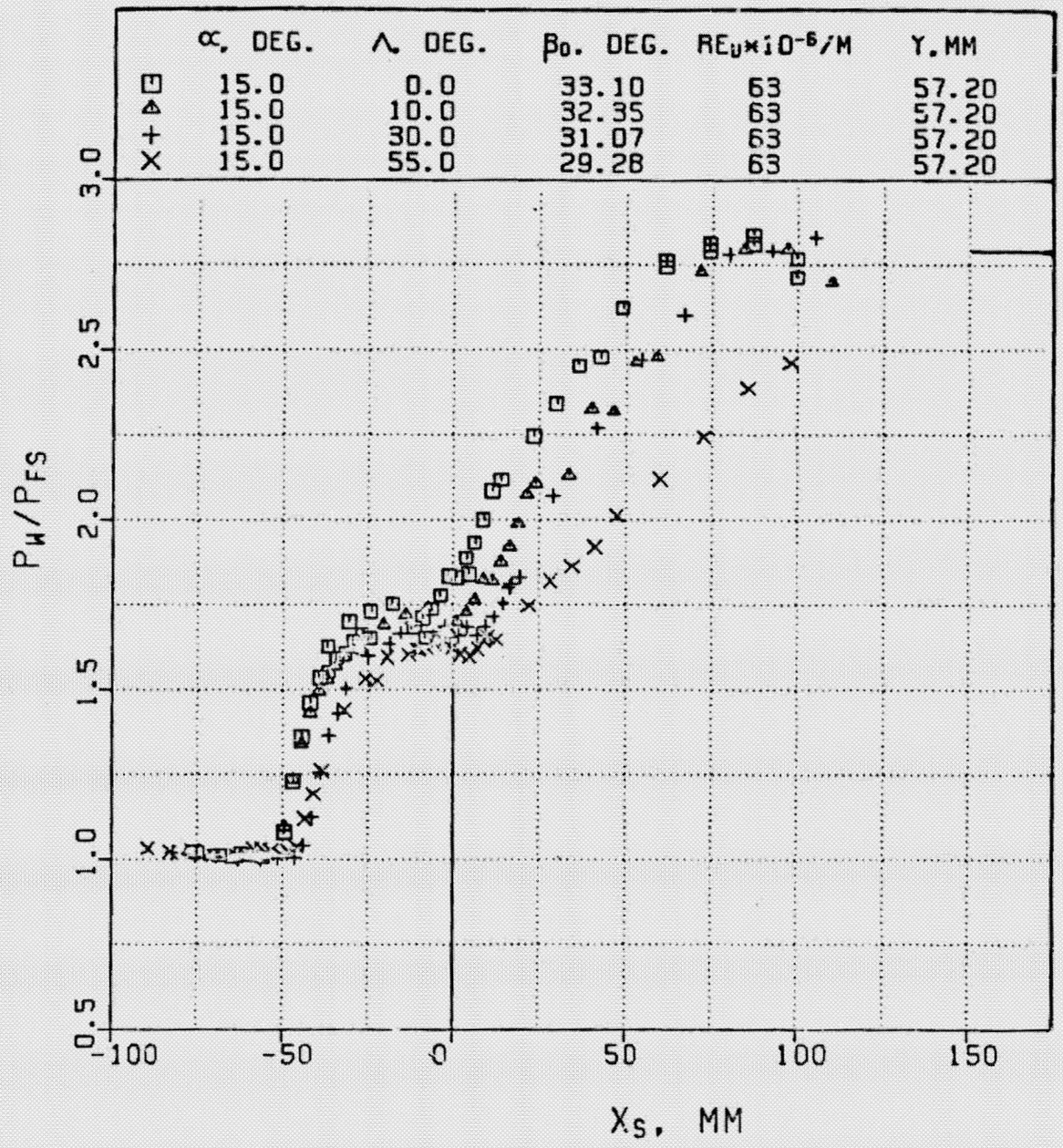

a. $\alpha_f = 15^\circ$.

Figure 29. Surface static pressure distribution.

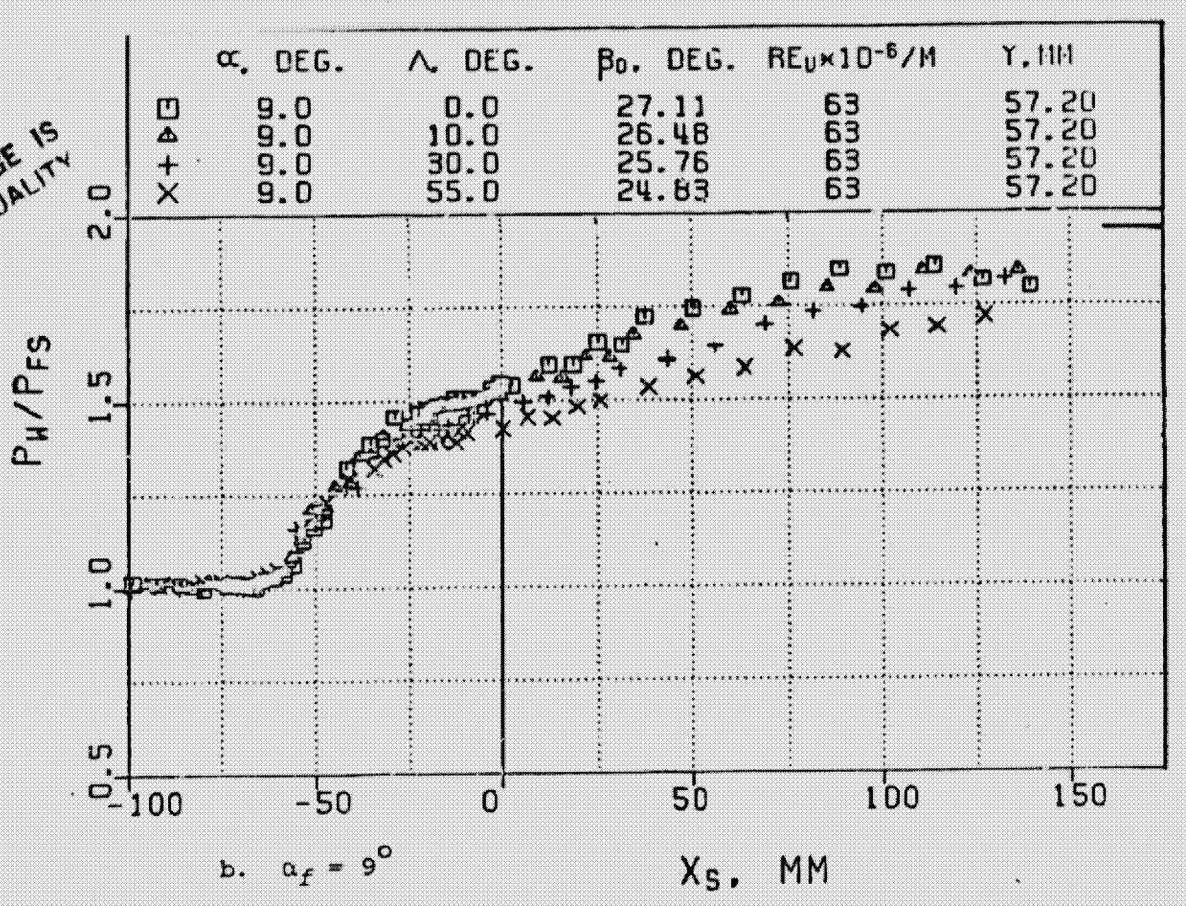

b. $\alpha_f = 9^\circ$

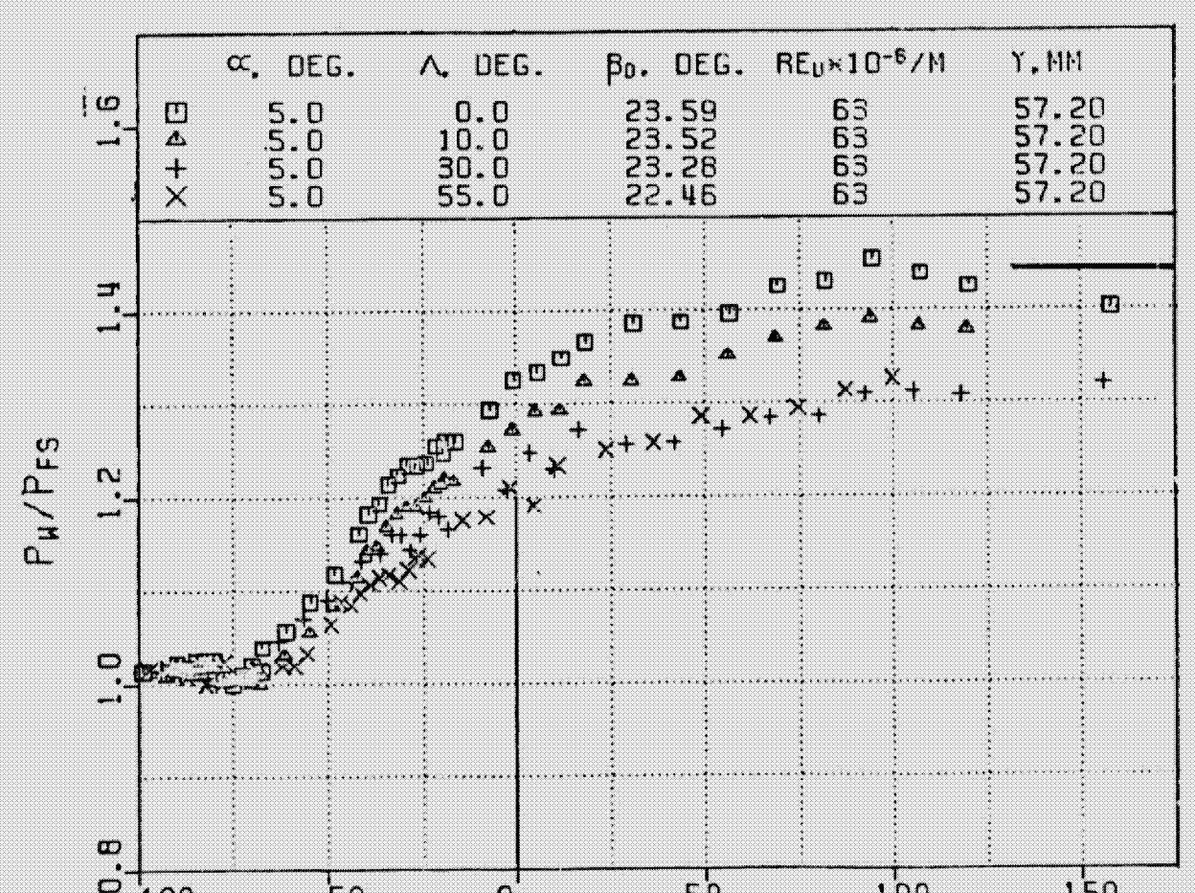

c. $\alpha_f = 5^\circ$.

Figure 29. (concluded).

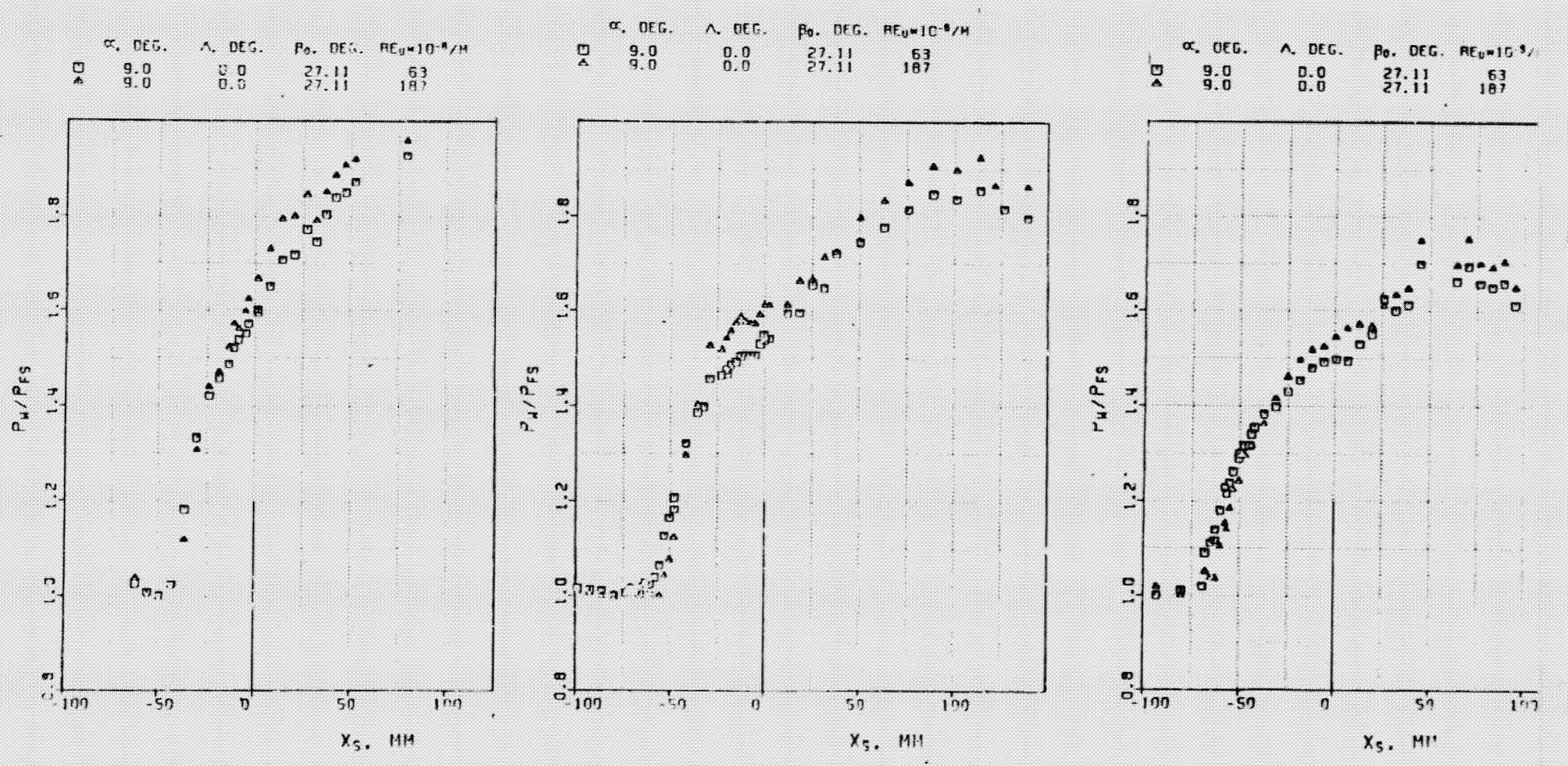

a. y = 31.8 mm. b. y = 57.2 mm. c. y = 82.5 mm.

Figure 30. Reynolds number effect on the surface static pressure distribution for an $\alpha_f = 9^o$, $\lambda_f = 0^o$ fin.

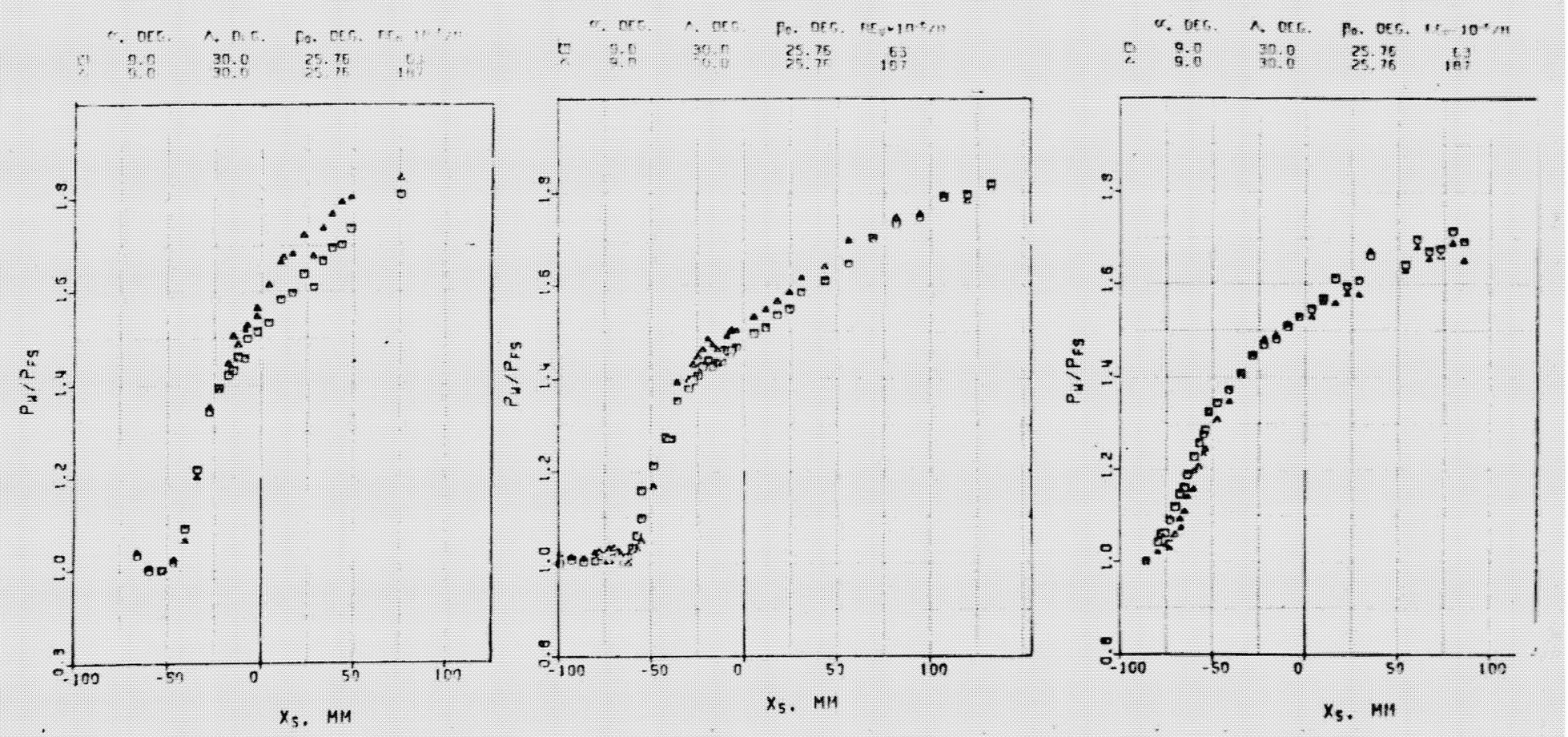

a. y = 31.8 mm. b. y = 57.2 mm. c. y = 82.5 mm.

Figure 31. Reynolds number effect on the surface static pressure distribution for an $\alpha_f = 9^\circ$, $\lambda_f = 30^\circ$ fin.

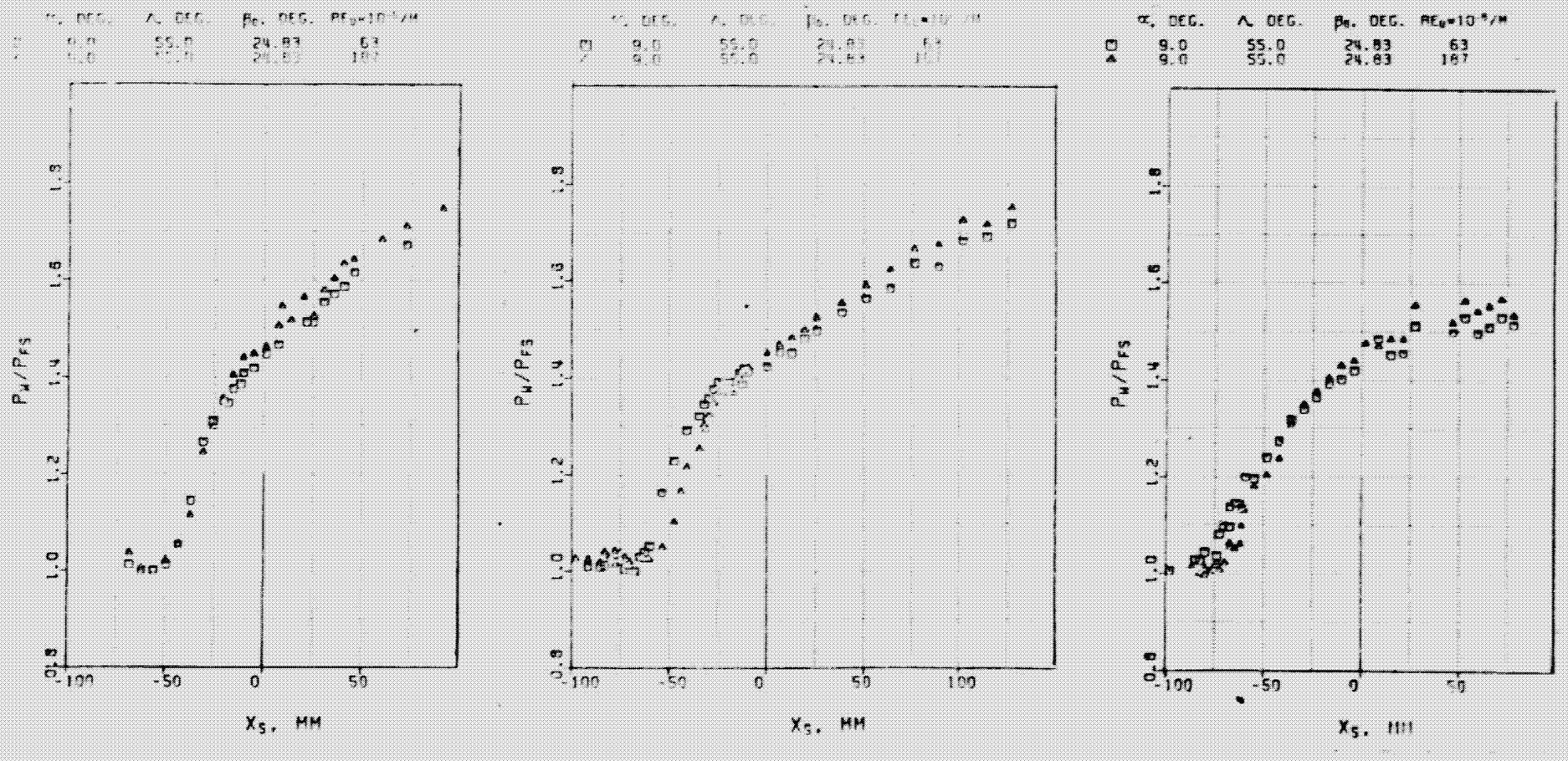

a. y = 31.8 mm. b. y = 57.2 mm. c. y = 82.5 mm.

Figure 32. Reynolds number effect on the surface static pressure distribution for an $\alpha_f = 9^{\circ}$, $\lambda_f = 55^{\circ}$ fin.

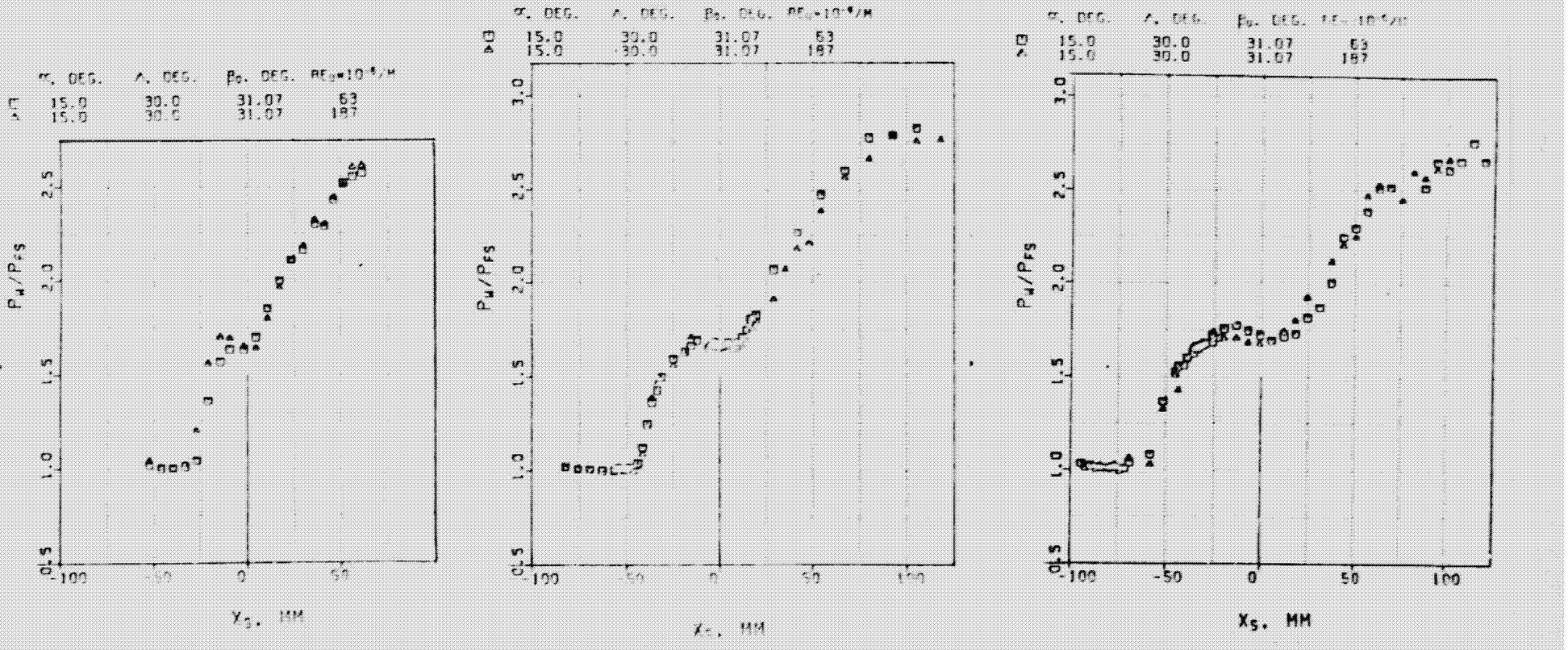

a. y = 31.8 mm. b. y = 57.2 mm. c. y = 82.5 mm.

Figure 33. Reynolds number effect on the surface static pressure distribution for an $\alpha_f = 15^{\circ}$, $\lambda_f = 30^{\circ}$ fin.

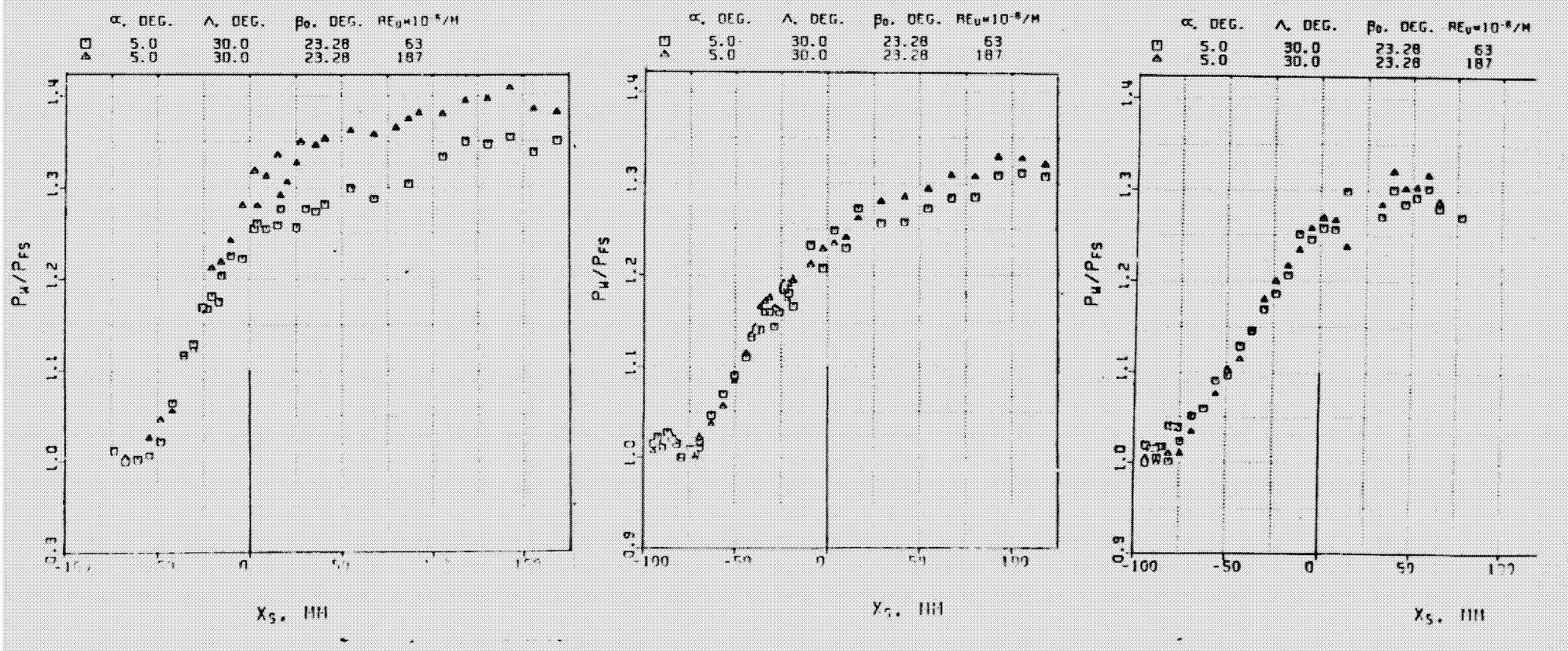

a. y = 31.8 mm. b. y = 57.2 mm. c. y = 82.5 mm.

Figure 34. Reynolds number effect on the surface static pressure distribution for an $\alpha_f = 5^o$, $\lambda_f = 30^o$ fin.

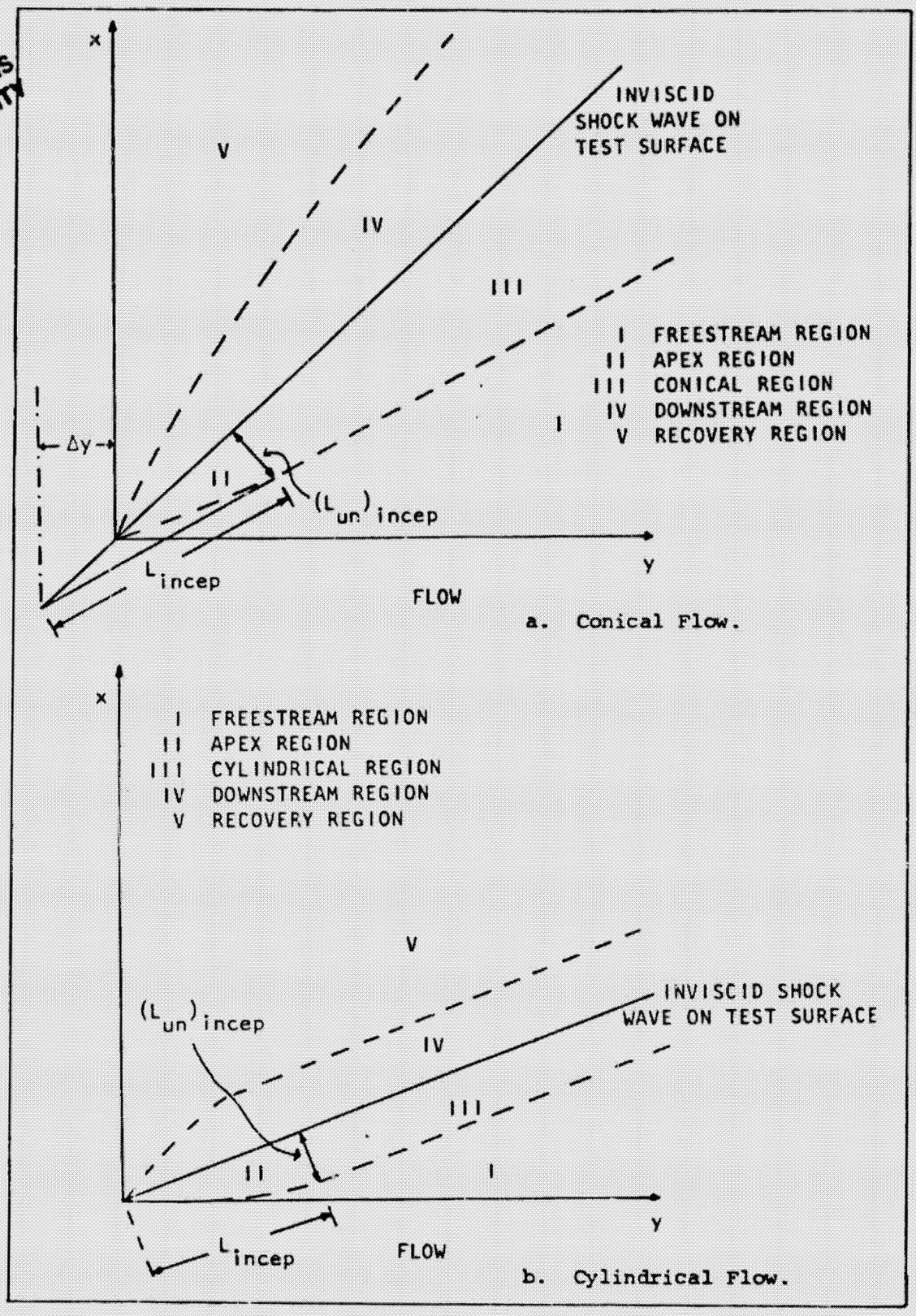

Figure 35. Schematic representation of main regions in surface flow patterns exhibiting conical or cylindrical symmetry.

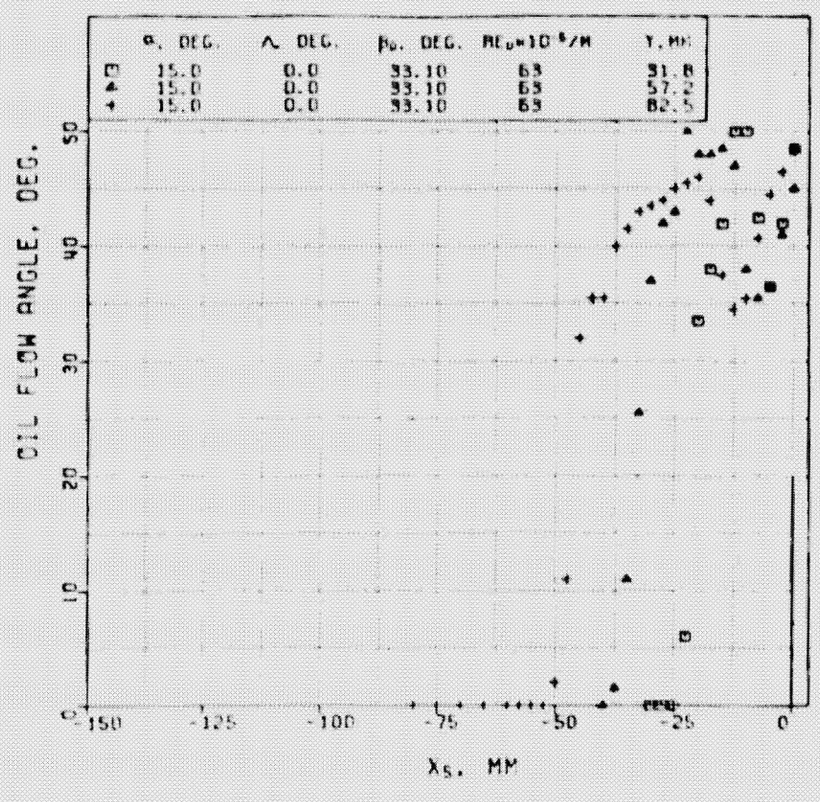

i. Flat plate.

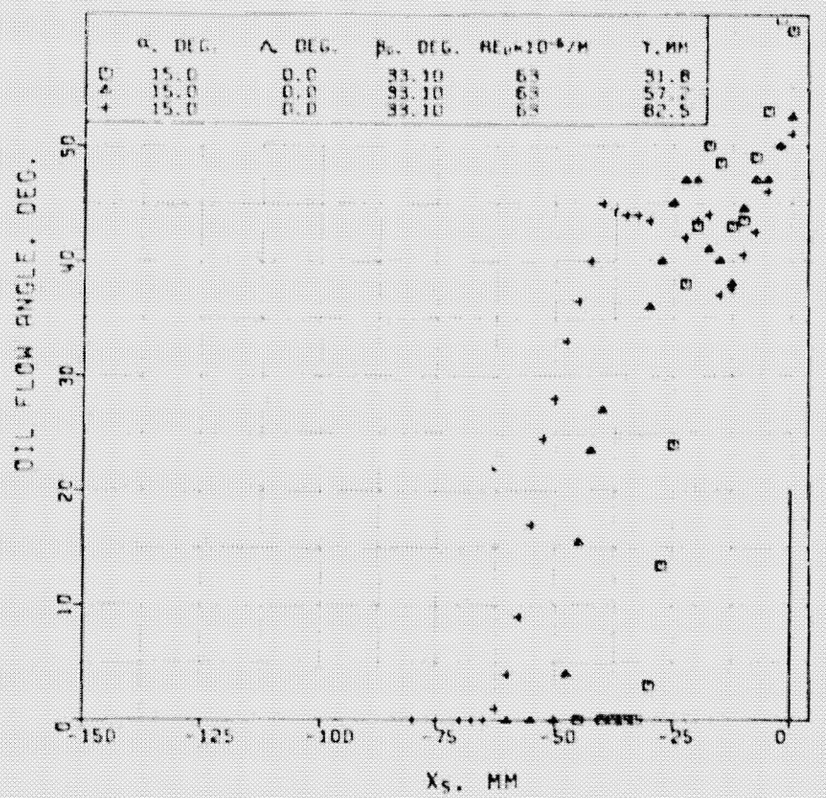

ii. Tunnel floor.

a. $\alpha_f = 15^\circ$, $\lambda_f = 0^\circ$.

Figure 36. Lampblack streak deflection angles upstream of the inviscid shock wave.

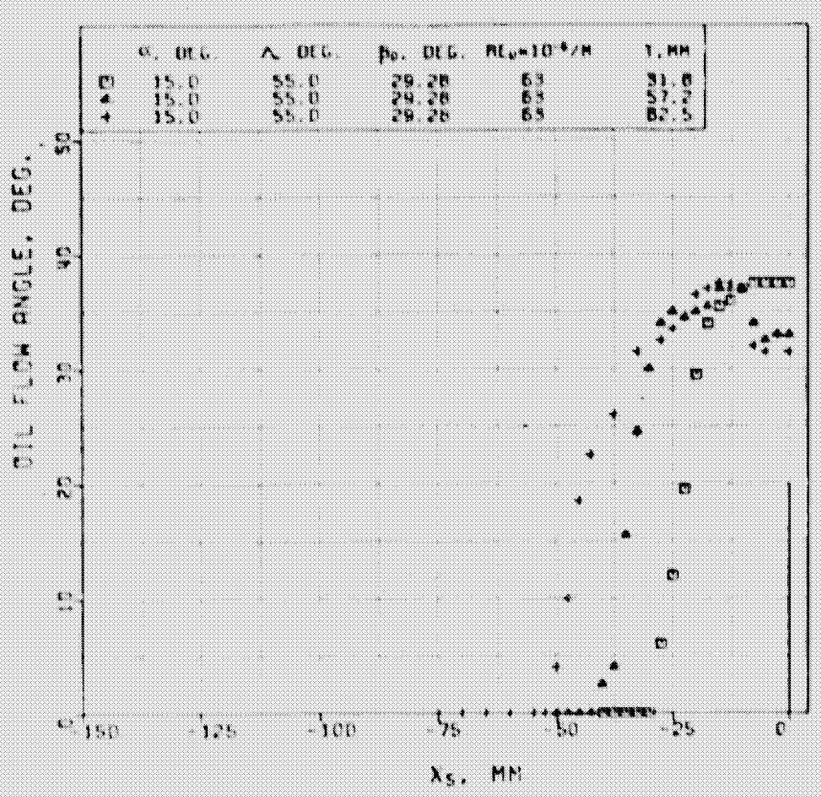

i. Flat plate.

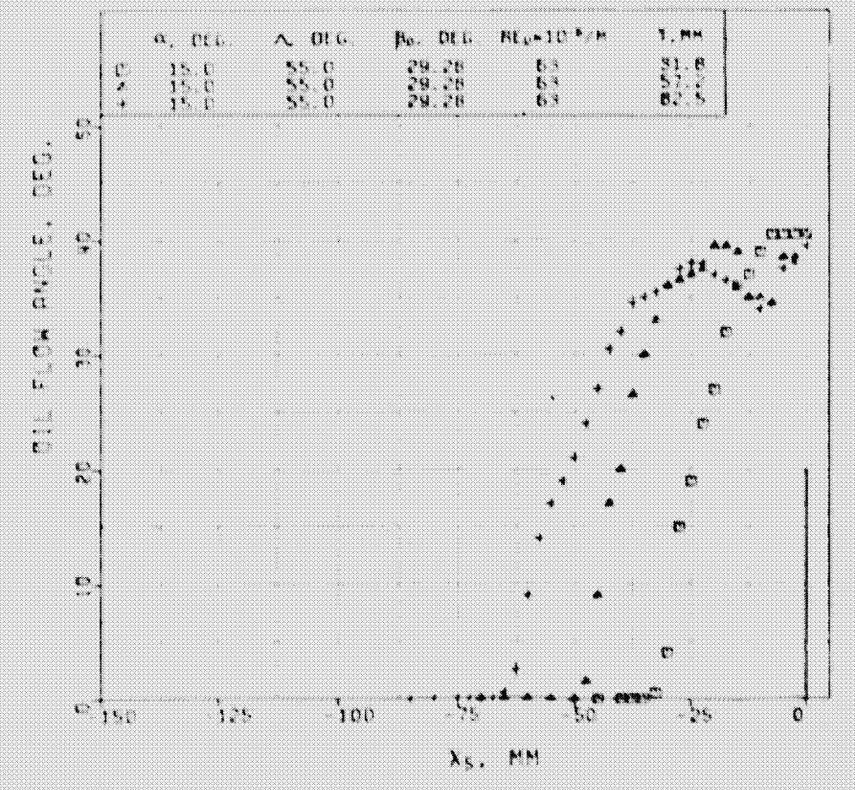

ii. Tunnel floor.

b. $\alpha_f = 15^o$, $\lambda_f = 55^o$.

Figure 36. (continued).

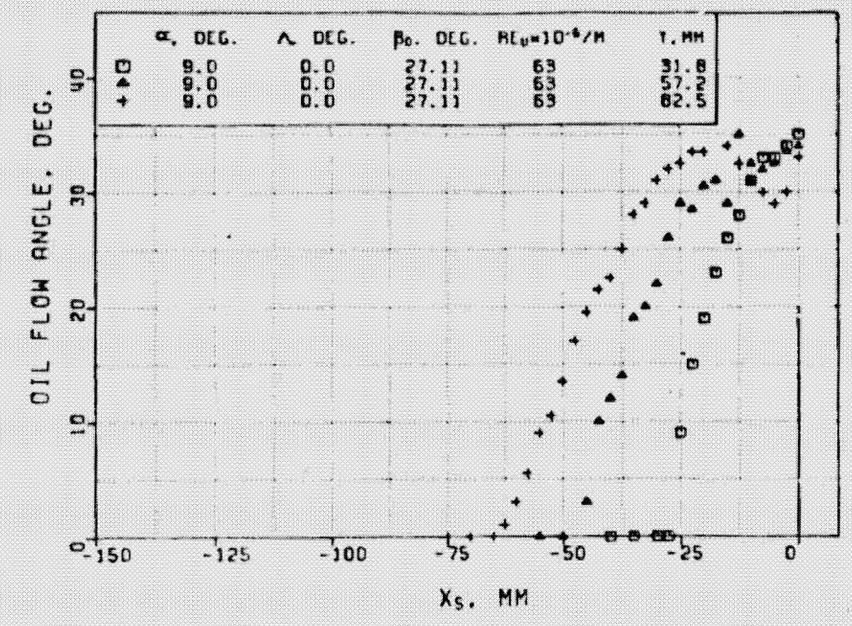

i. Flat plate.

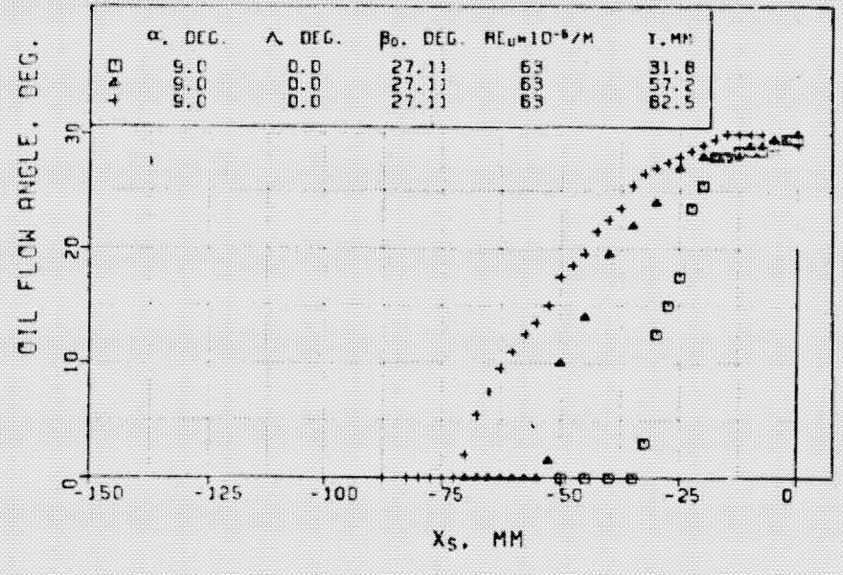

ii. Tunnel floor.

c. $\alpha_f = 9^\circ$, $\lambda_f = 0^\circ$.

Figure 36. (continued).

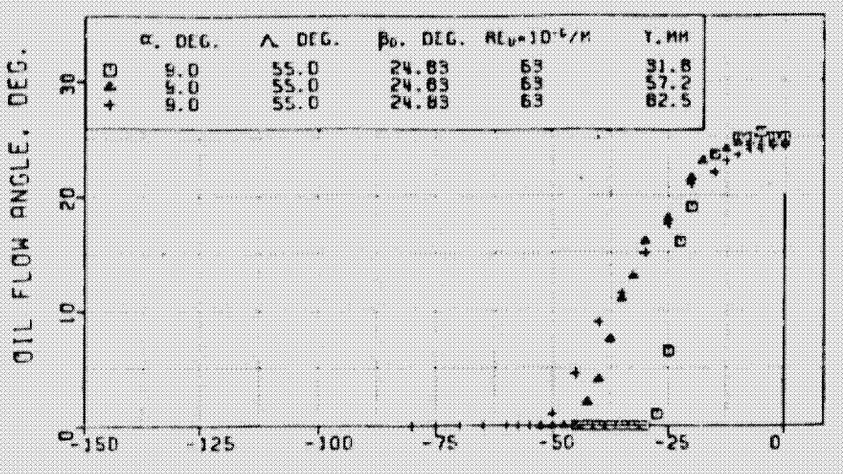

i. Flat plate.

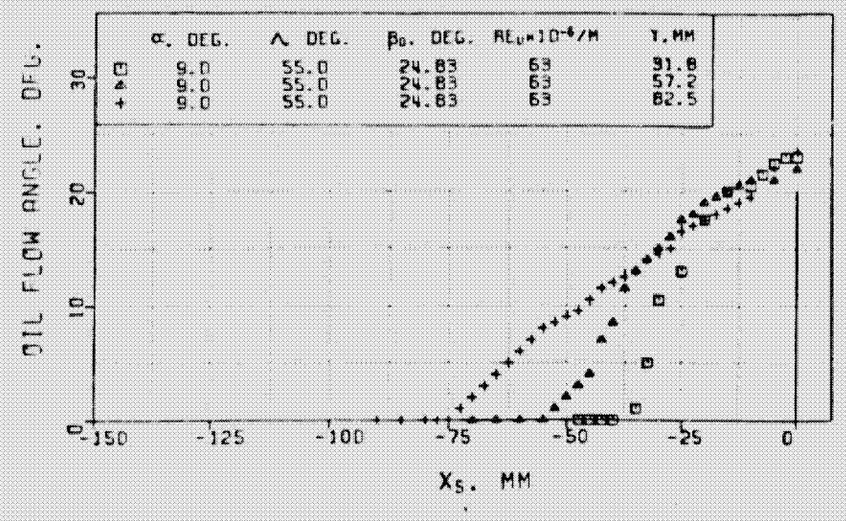

ii. Tunnel floor.

d. $\alpha_f = 9^{\circ}$, $\lambda_f = 55^{\circ}$.

Figure 36. (continued).

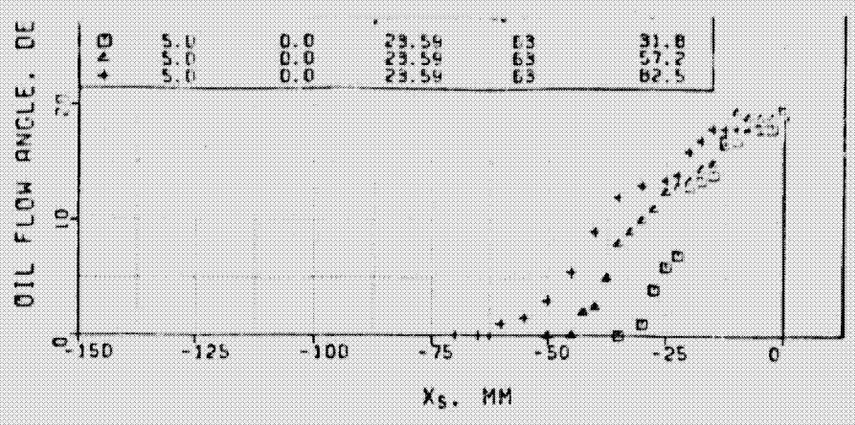

ORIGINAL PAGE IS
OF POOR QUALITY

i. Flat plate.

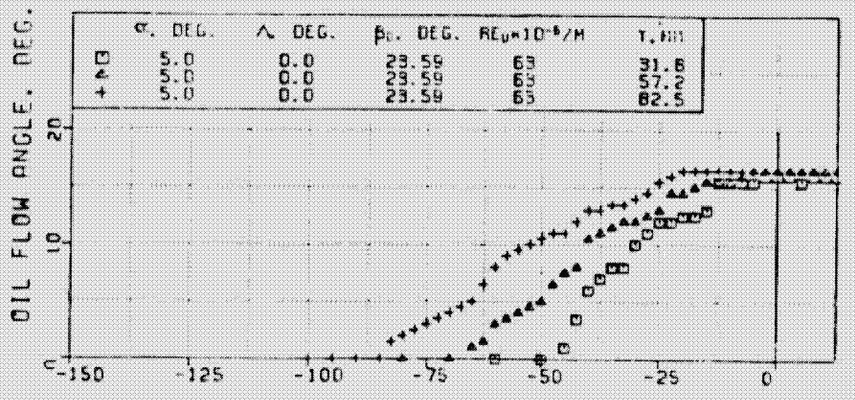

ii. Tunnel floor.

e. $\alpha_f = 5^o$, $\lambda_f = 0^o$.

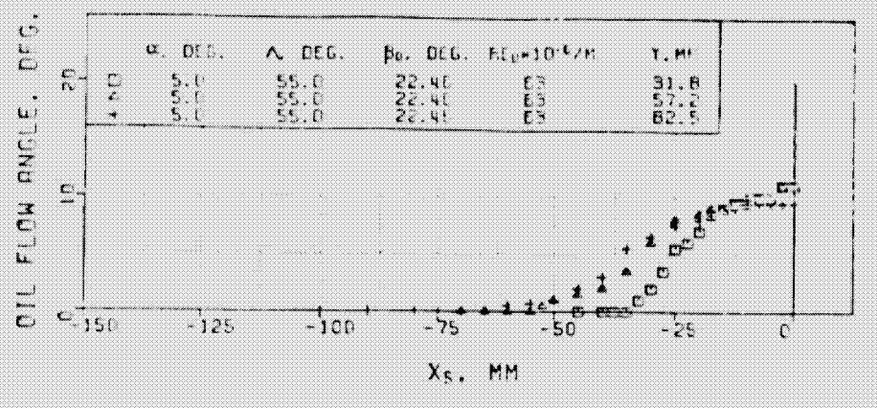

i. Flat plate.

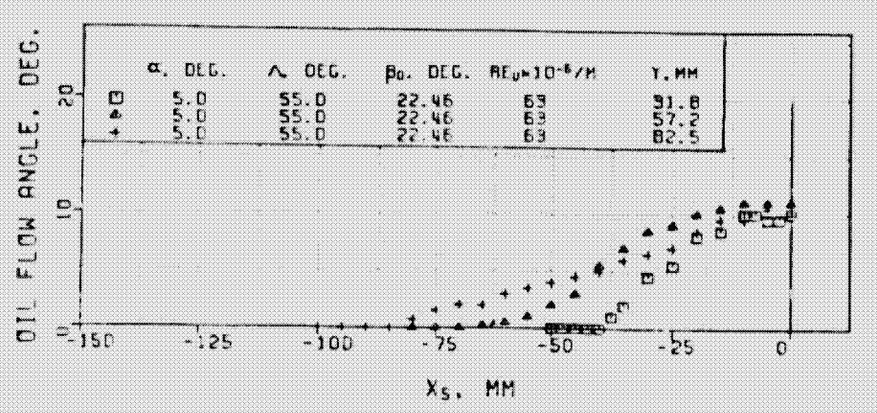

ii. Tunnel floor.

f. $\alpha_f = 5^o$, $\lambda_f = 55^o$.

Figure 36. (concluded).

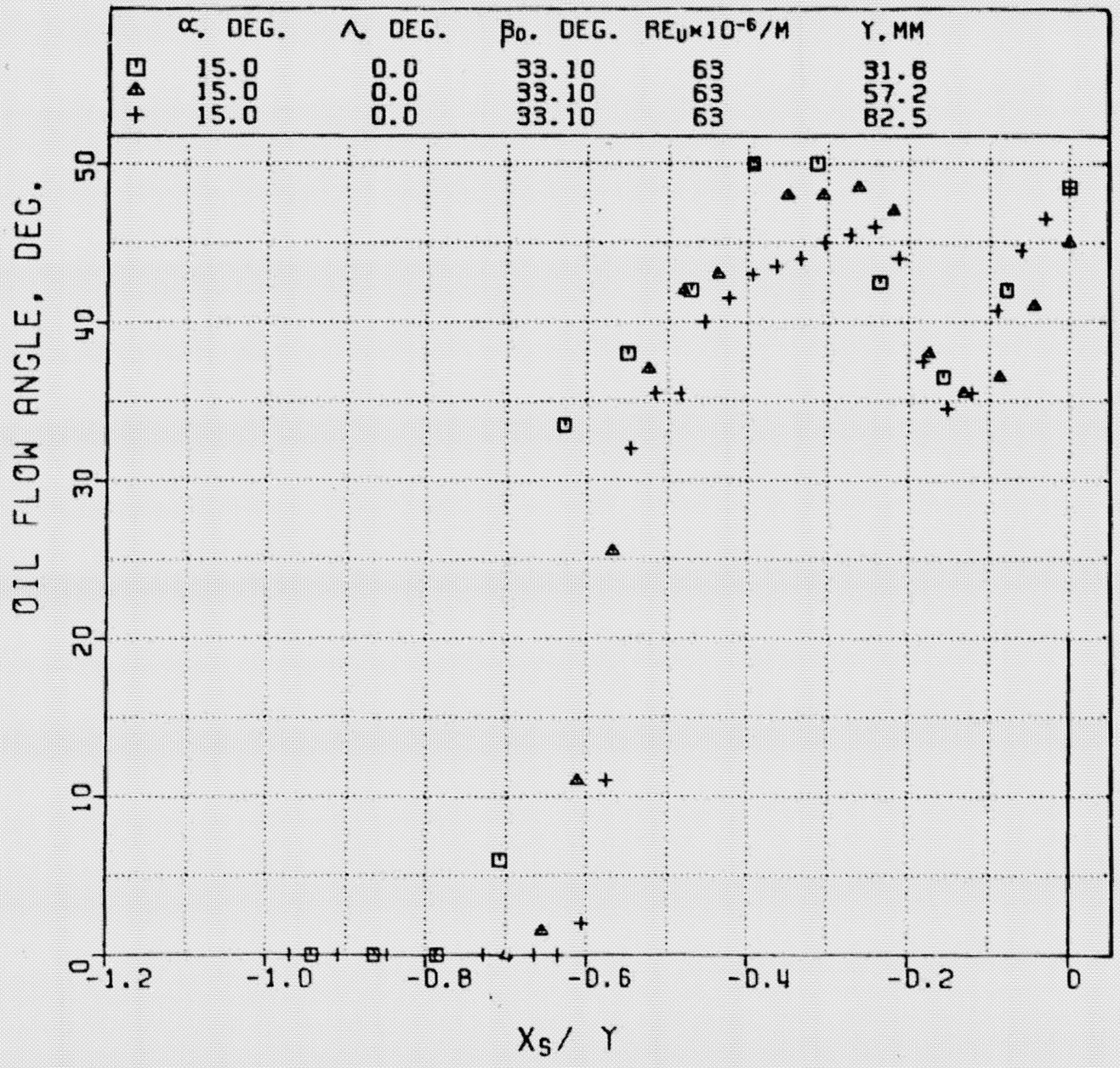

a. Flat plate, $\alpha_f = 15^\circ$, $\lambda_f = 0^\circ$.

Figure 37. The lampblack streak angle upstream of the shock wave against distance normalized by the span.

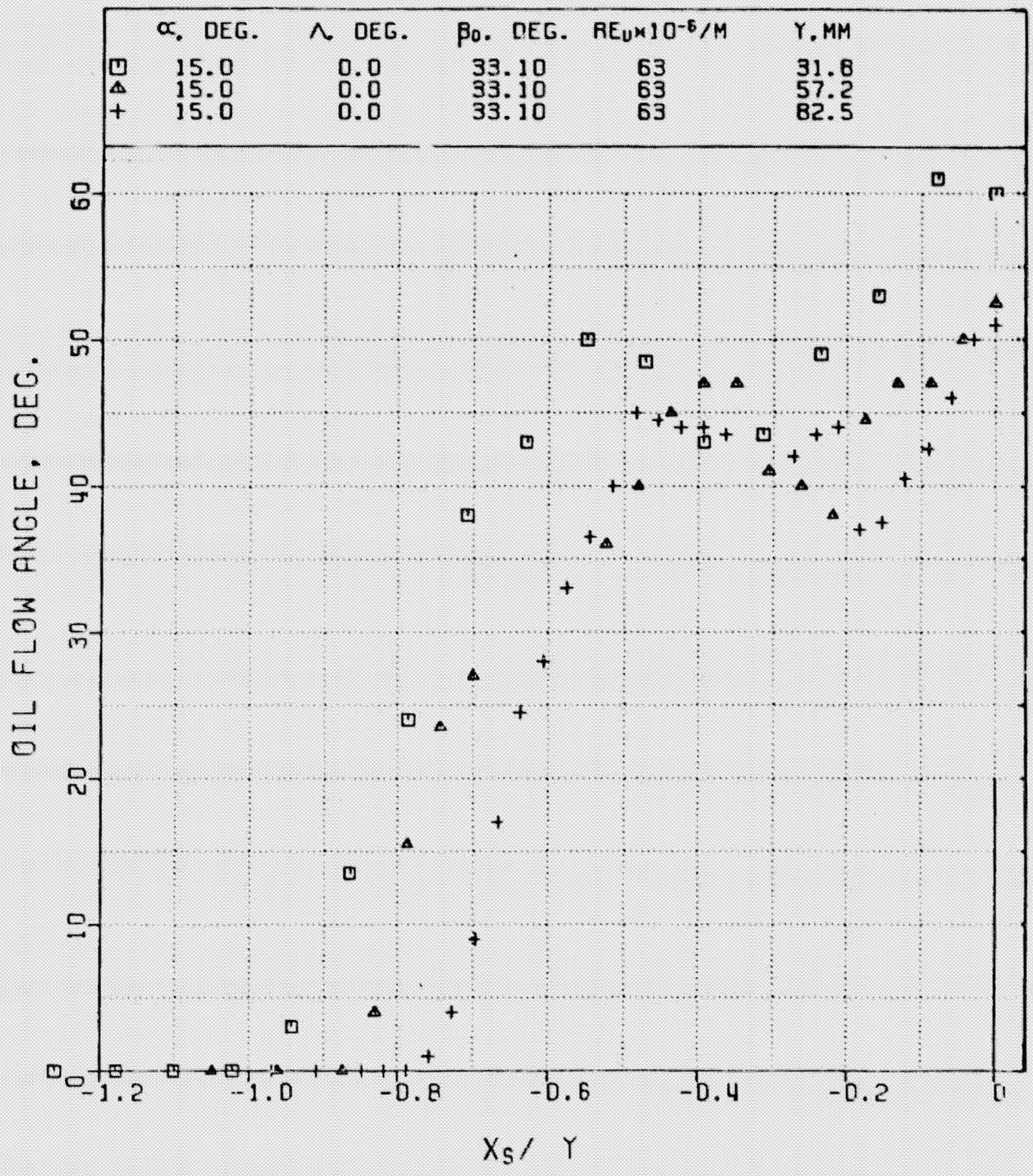

b. Tunnel floor, $\alpha_f = 15^\circ$, $\lambda_f = 0^\circ$.

Figure 37. (concluded).

ORIGINAL PAGE IS
OF POOR QUALITY

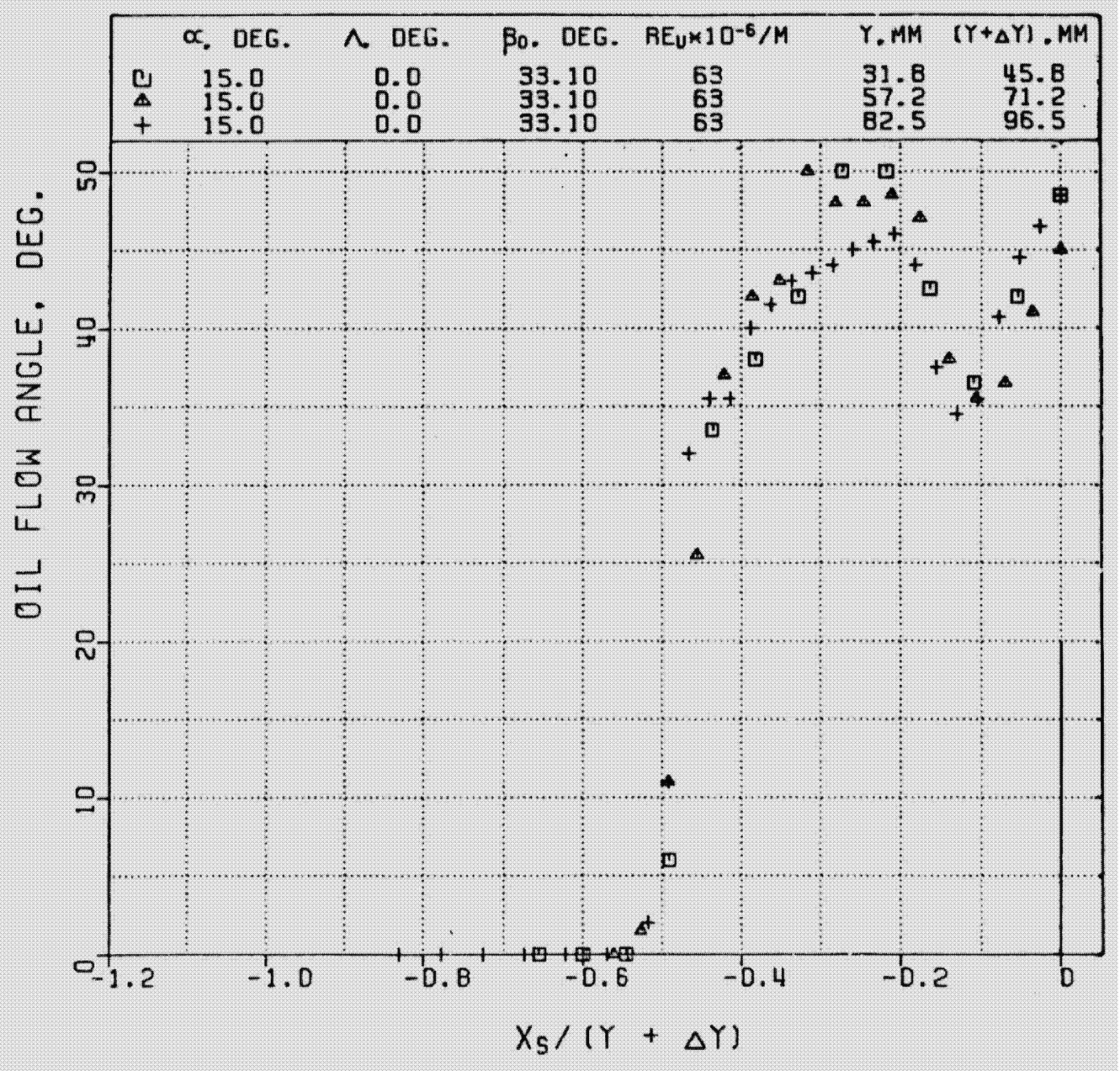

i. Flat plate.

a. $\alpha_f = 15^\circ$, $\lambda_f = 0^\circ$.

Figure 38. Quasi-conical nature of the lampblack streak angle upstream of the inviscid shock wave.

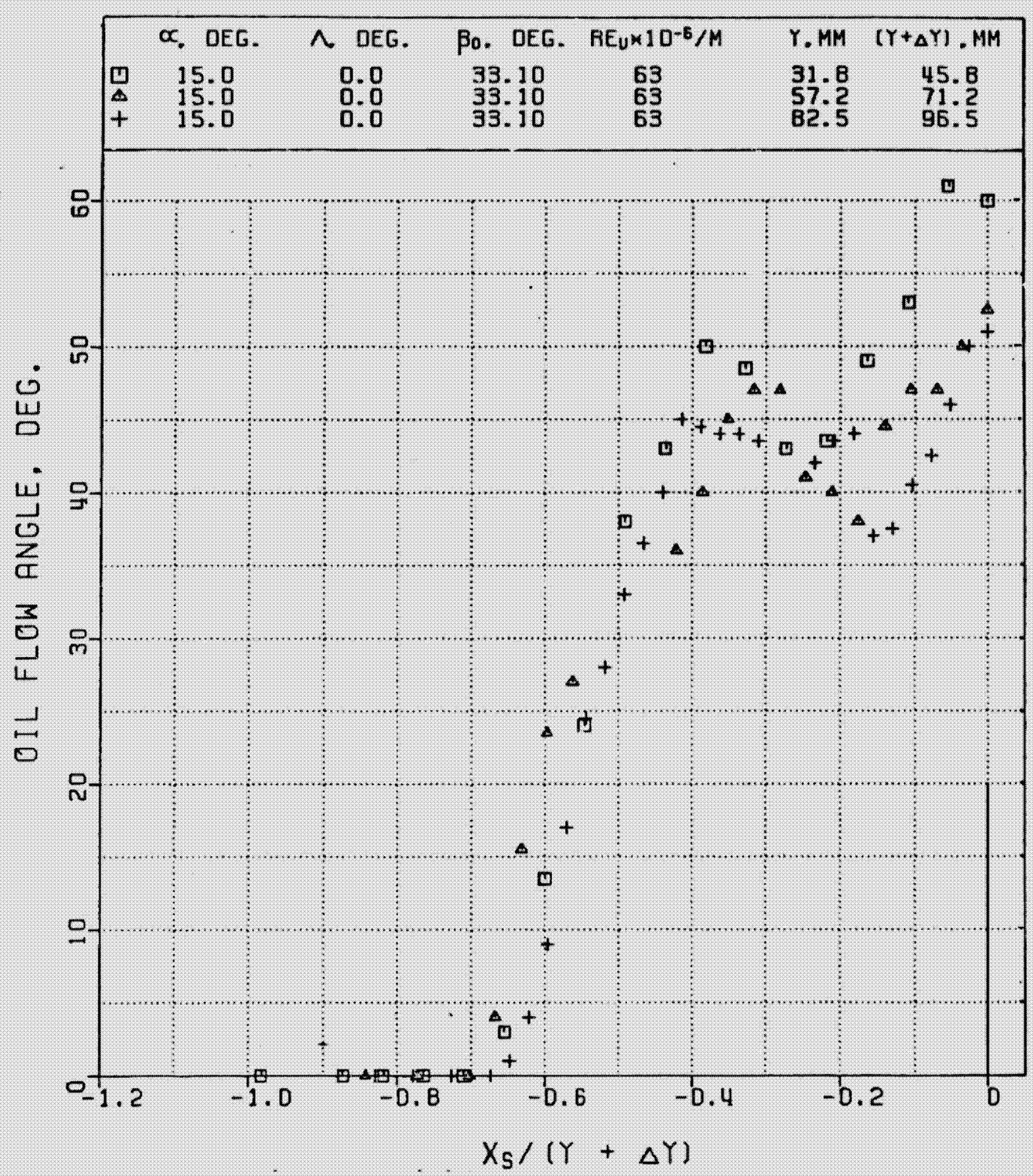

ii. Tunnel floor.

a. $\alpha_f = 15^\circ$, $\lambda_f = 0^\circ$.

Figure 38. (continued).

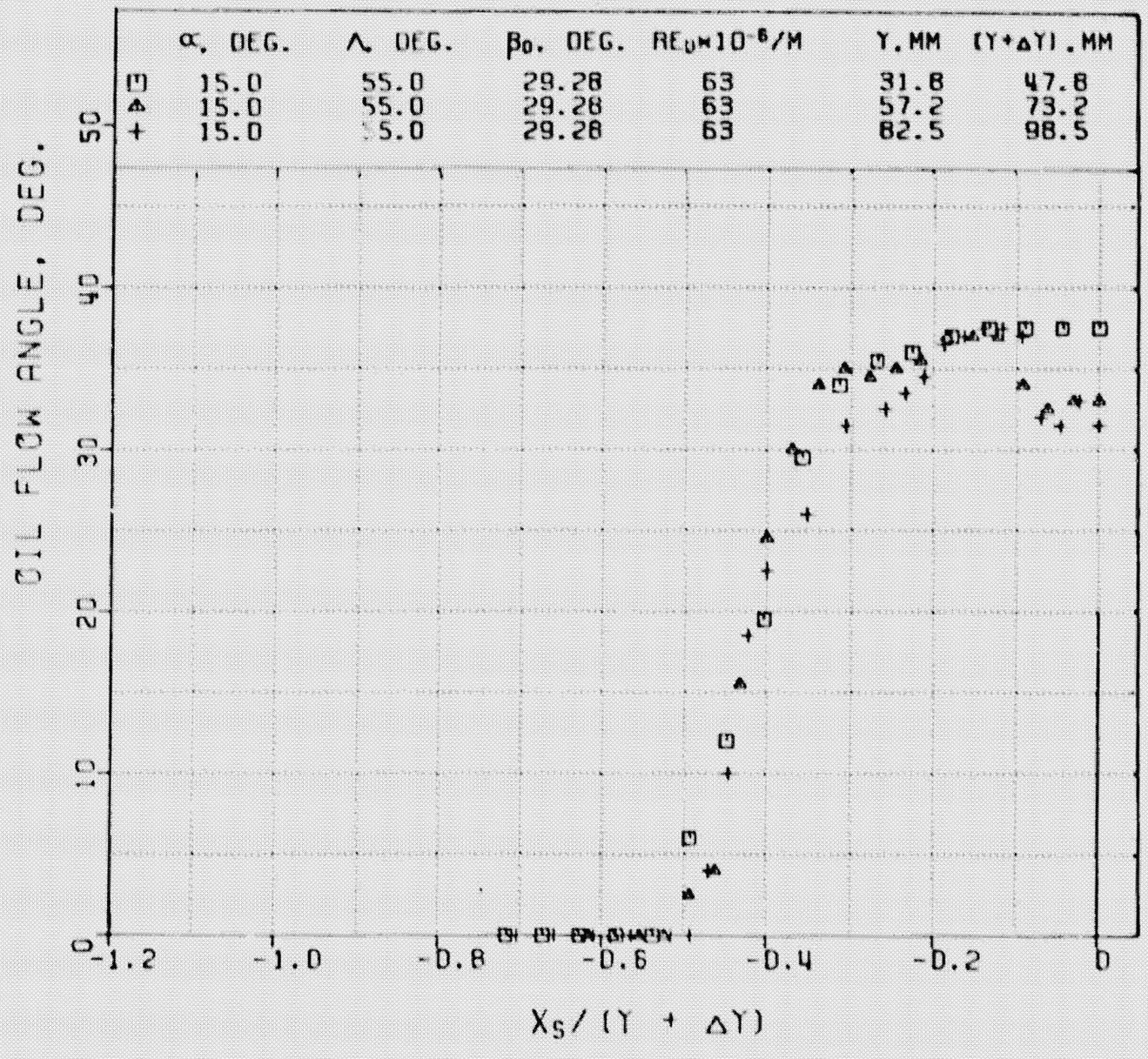

i. Flat plate.

b. $\alpha_f = 15^{\circ}$, $\Lambda_f = 55^{\circ}$.

Figure 38. (continued).

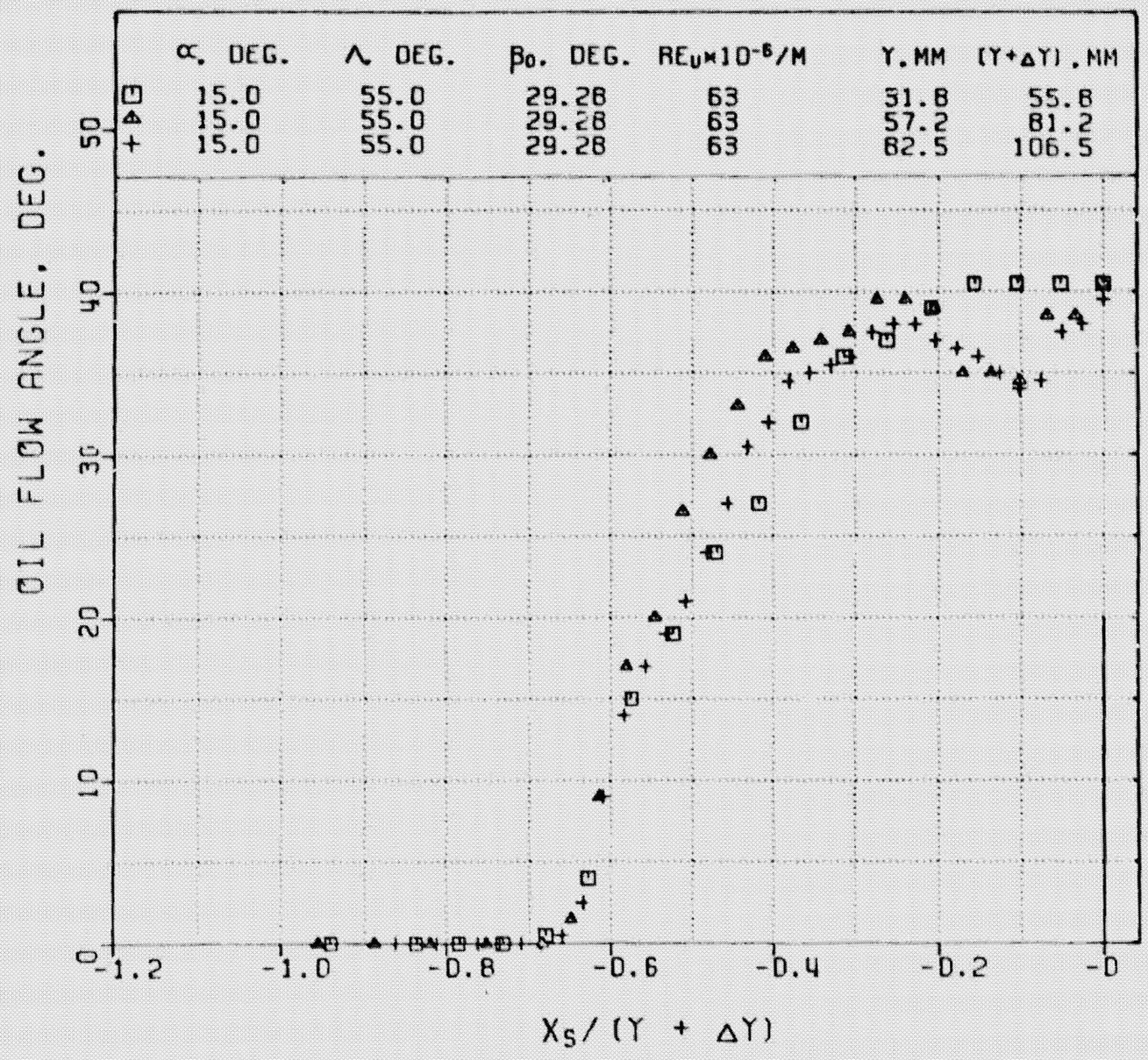

ii. Tunnel floor.

b. $\alpha_f = 15^\circ$, $\lambda_f = 55^\circ$.

Figure 38. (continued).

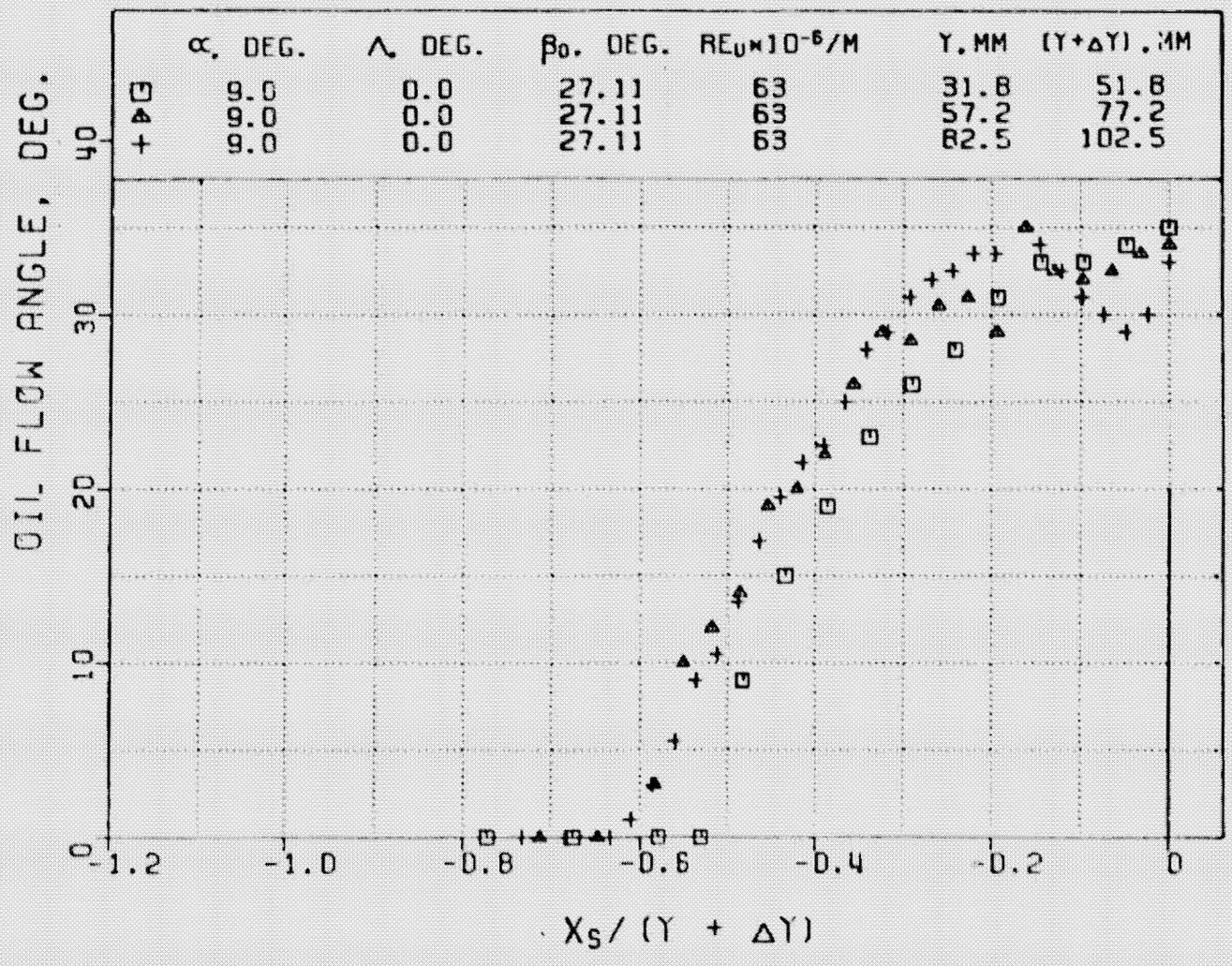

i. Flat plate.

c. $\alpha_f = 9^\circ$, $\lambda_f = 0^\circ$.

Figure 38. (continued).

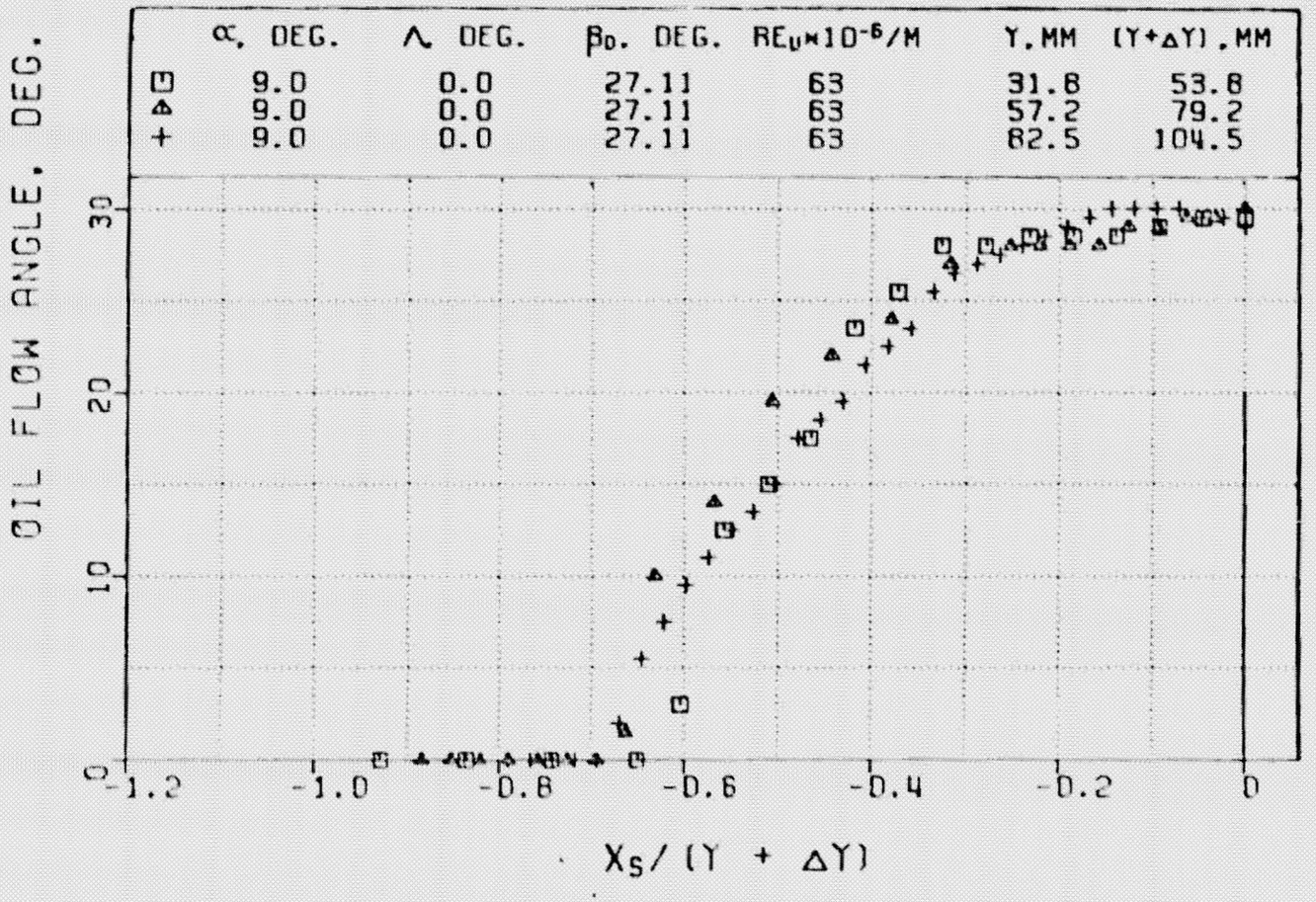

ii. Tunnel floor.

c. $\alpha_f = 9^\circ$, $\lambda_f = 0^\circ$.

Figure 38. (continued).

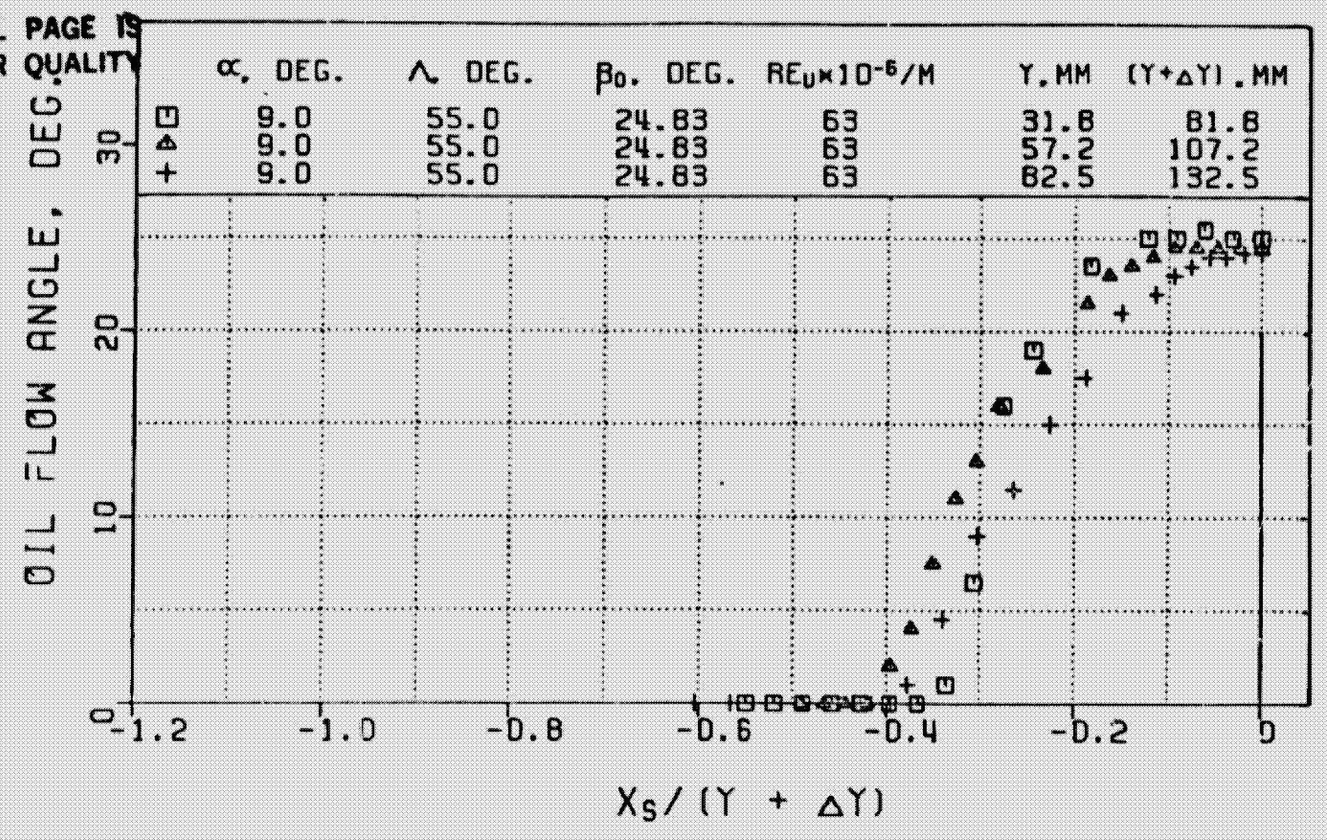

i. Flat plate.

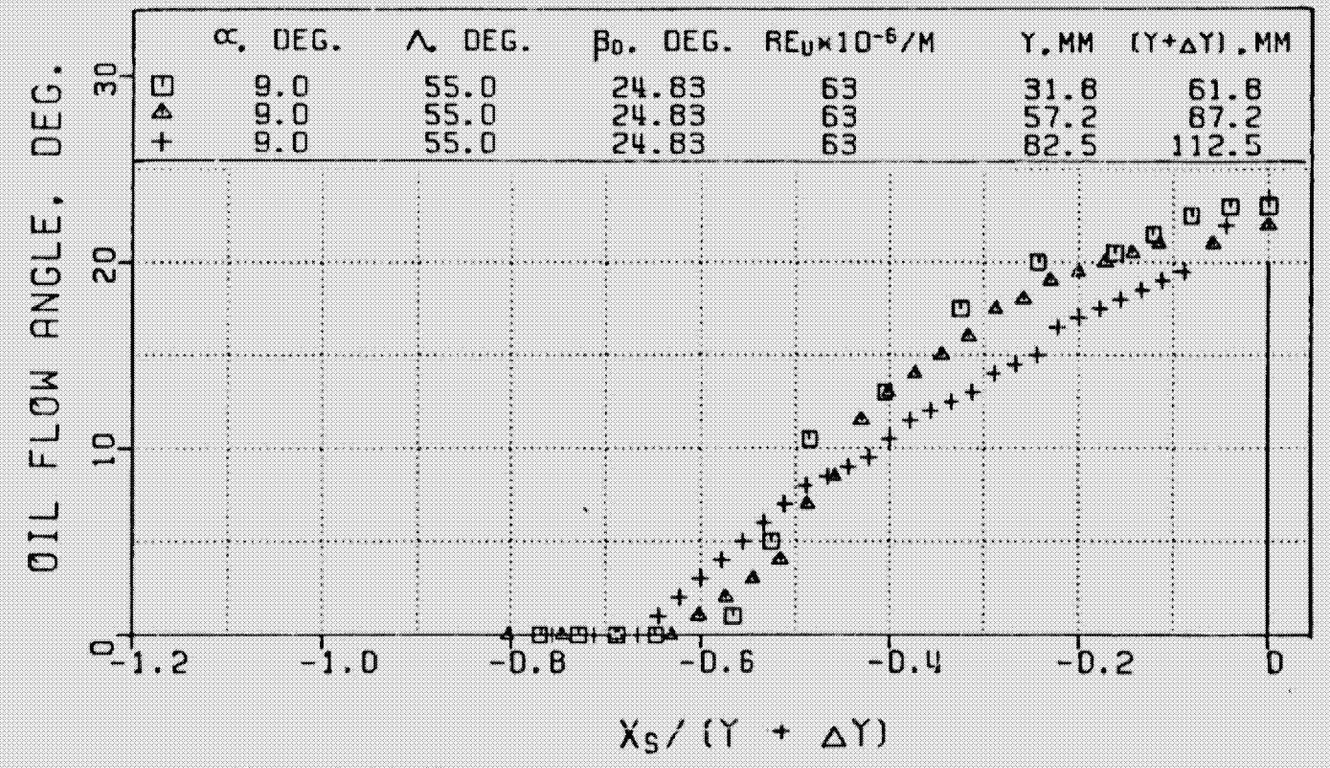

ii. Tunnel floor.

d. $\alpha_f = 9^\circ$, $\lambda_f = 55^\circ$.

Figure 38. (continued).

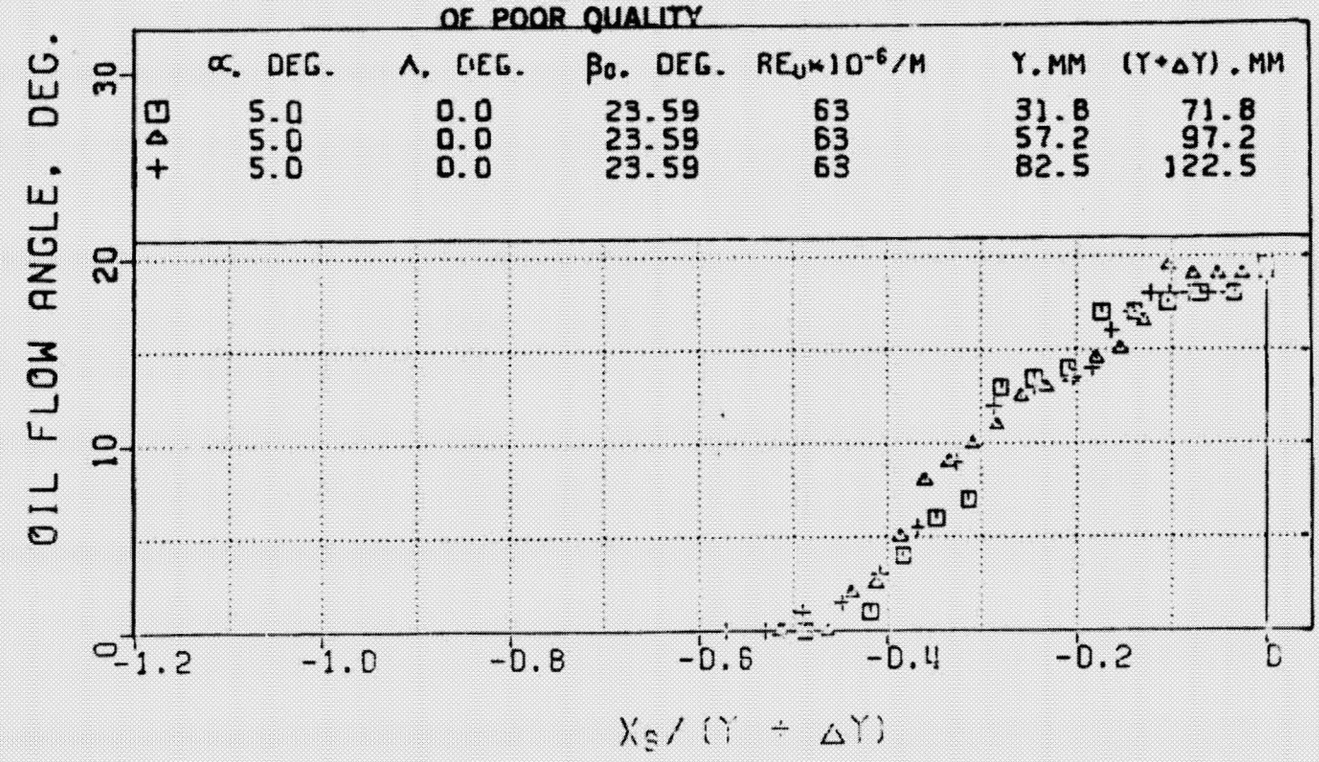

i. Flat plate.

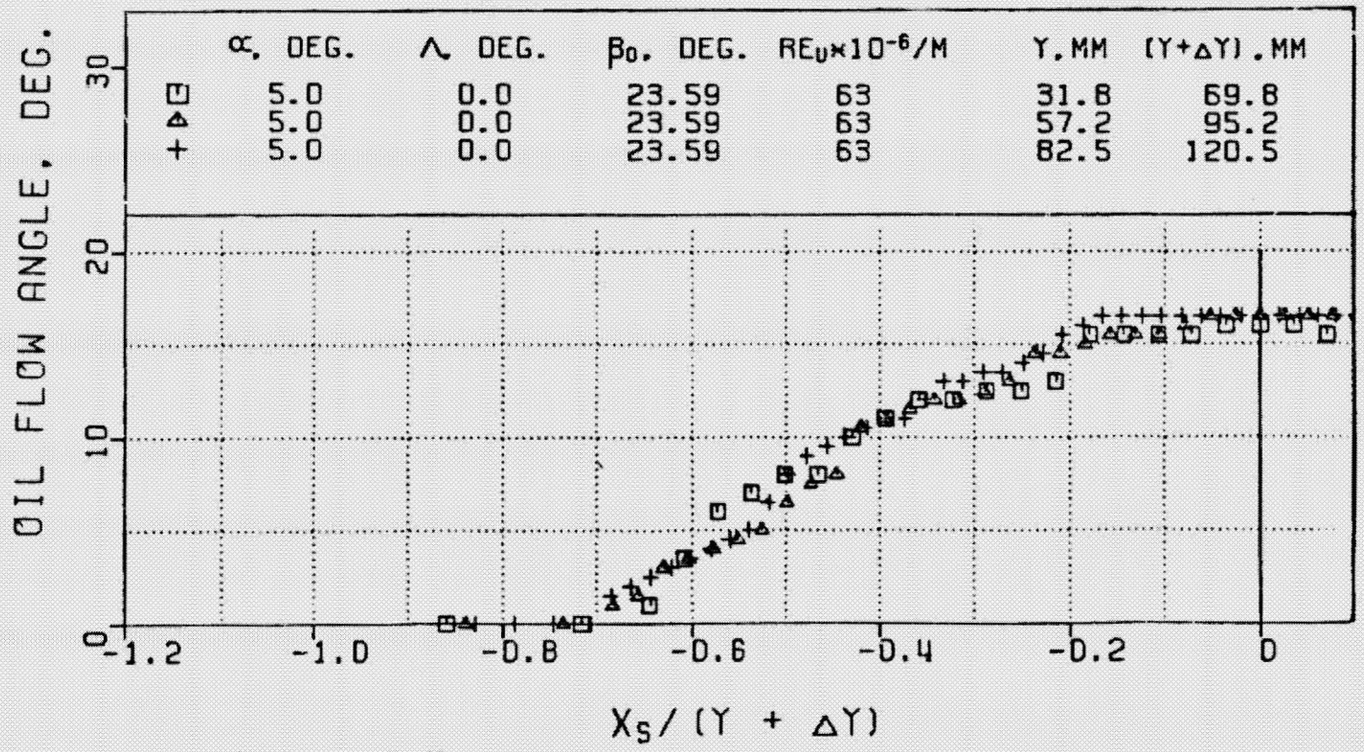

ii. Tunnel floor.

e. $\alpha_f = 5^\circ$, $\lambda_f = 0^\circ$.

Figure 38. (continued).

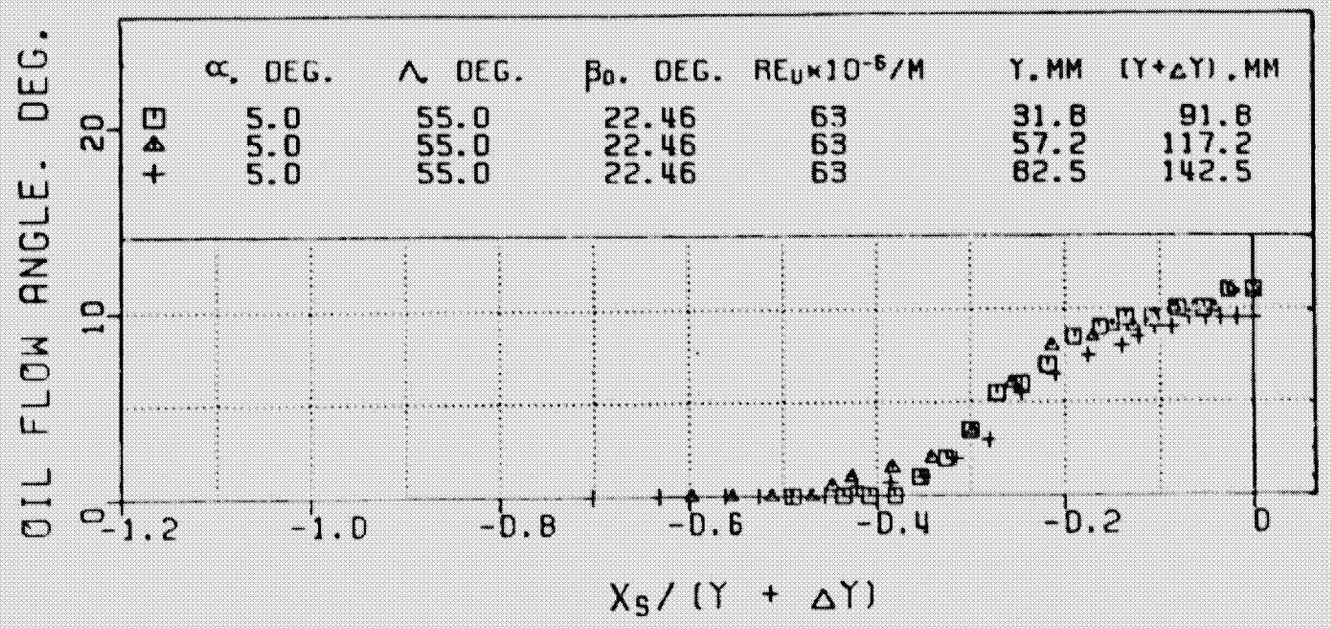

i. Flat plate.

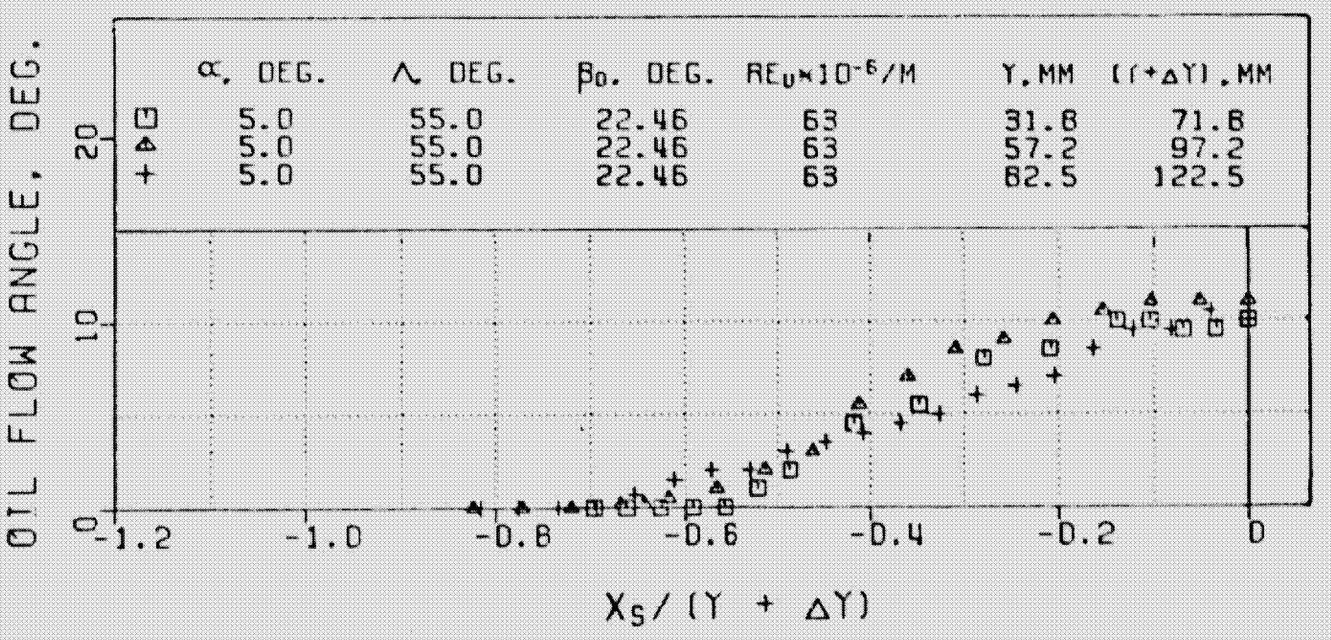

ii. Tunnel floor.

f. $\alpha_f = 5^o$, $\lambda_f = 55^o$.

Figure 38. (concluded).

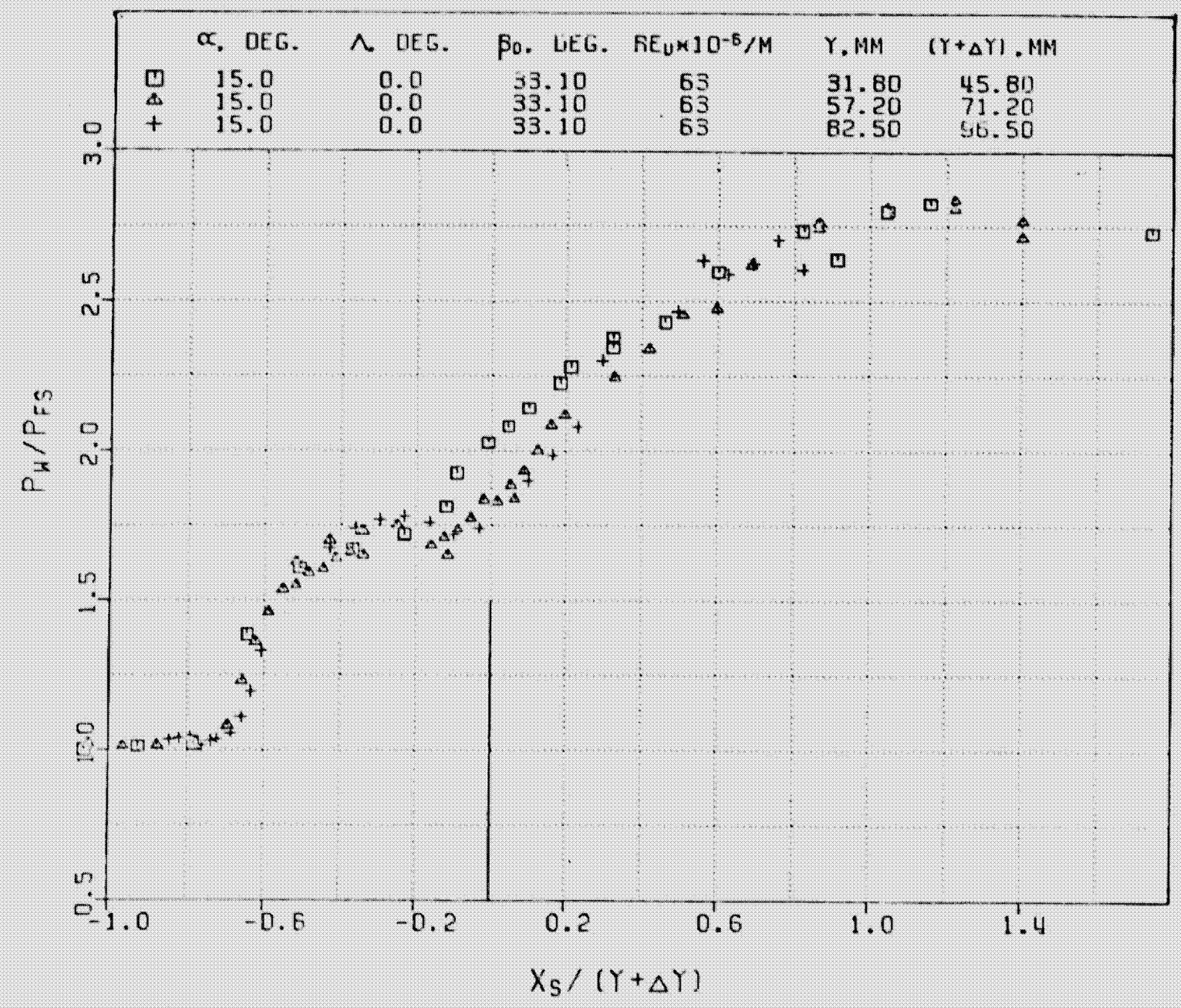

a. $\alpha_f = 15^\circ$, $\lambda_f = 0^\circ$.

Figure 39. Quasi-conical nature of the surface static pressure in the interaction region.

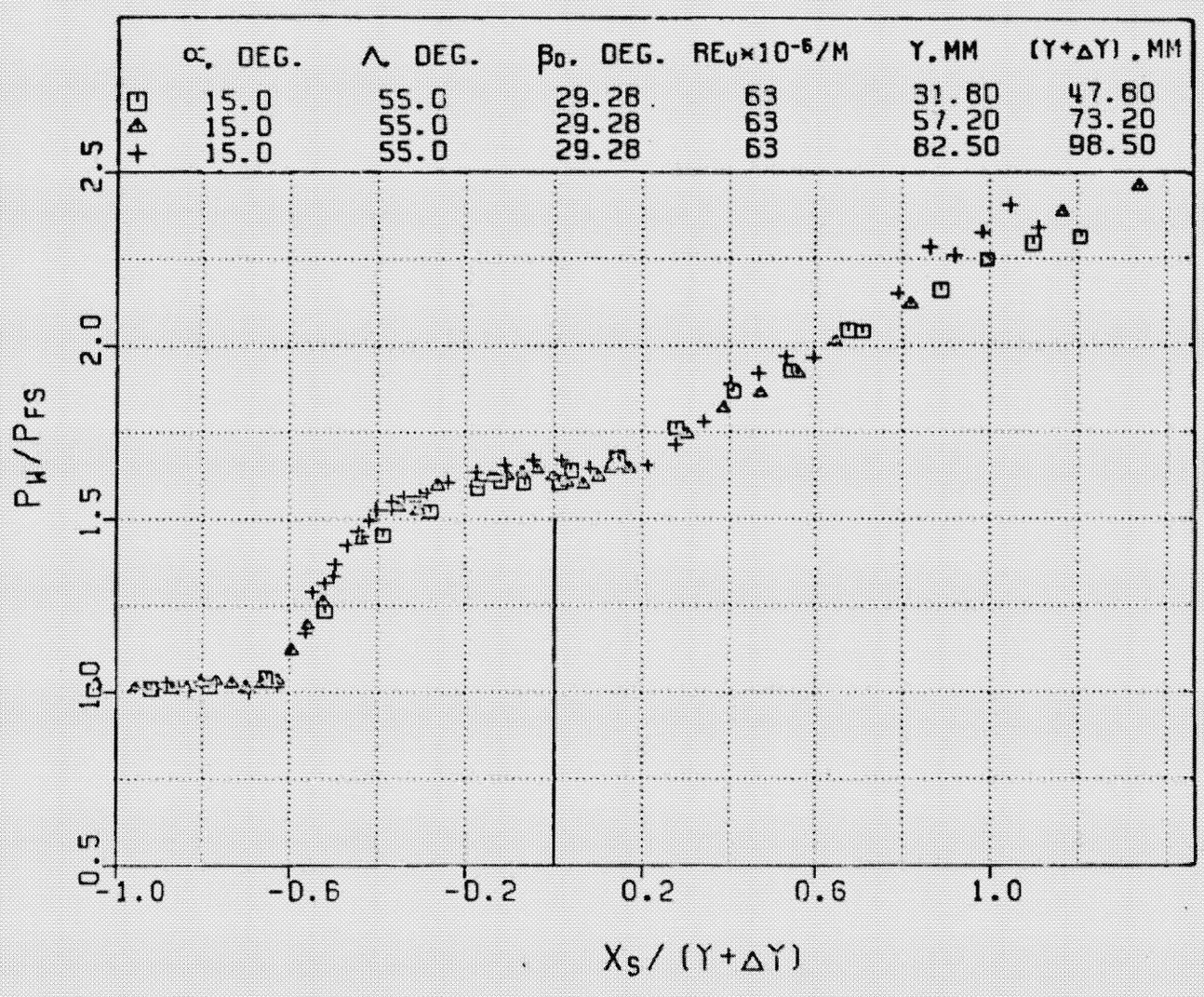

b. $\alpha_f = 15^\circ$, $\lambda_f = 55^\circ$.

Figure 39. (continued).

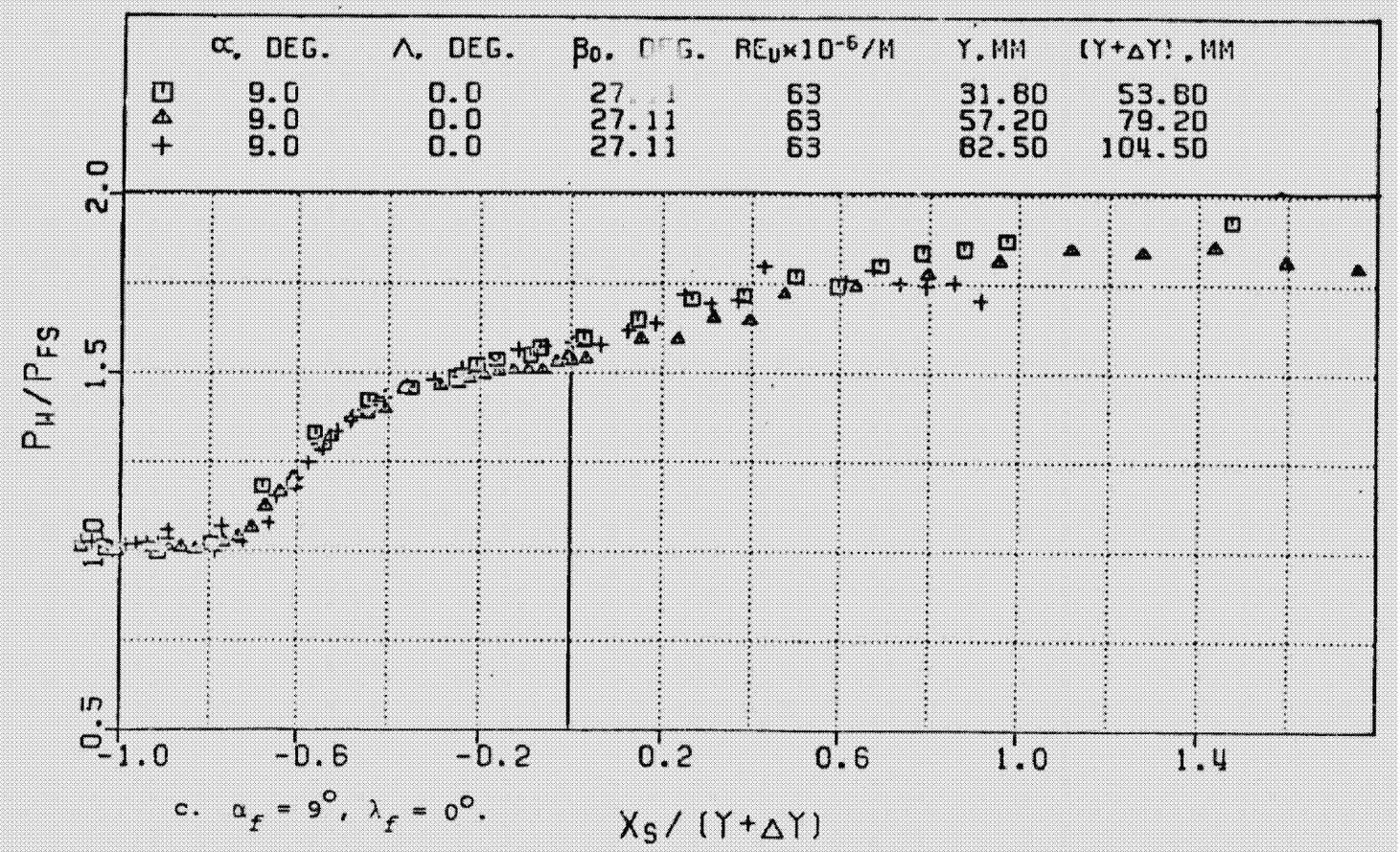

c. $\alpha_f = 9^\circ$, $\lambda_f = 0^\circ$.

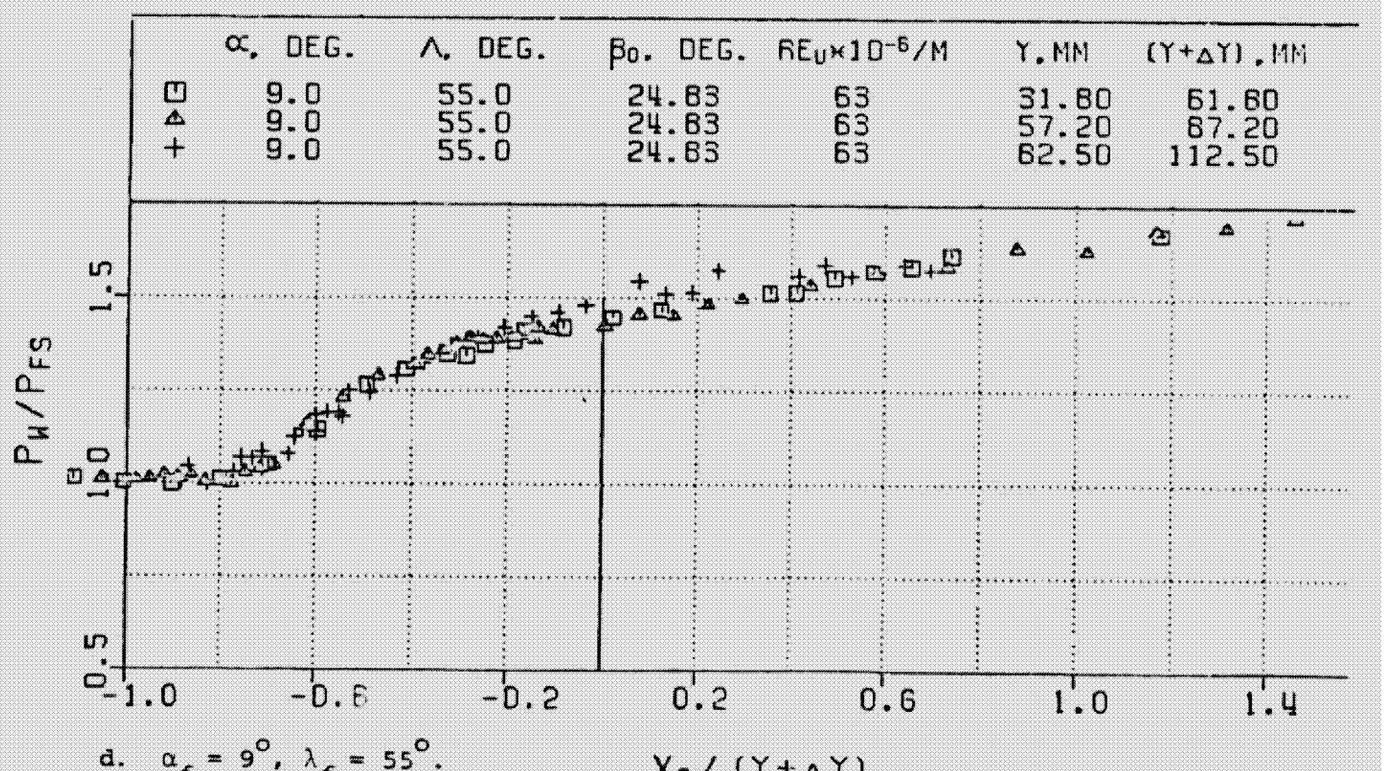

d. $\alpha_f = 9^\circ$, $\lambda_f = 55^\circ$.

Figure 39. (continued).

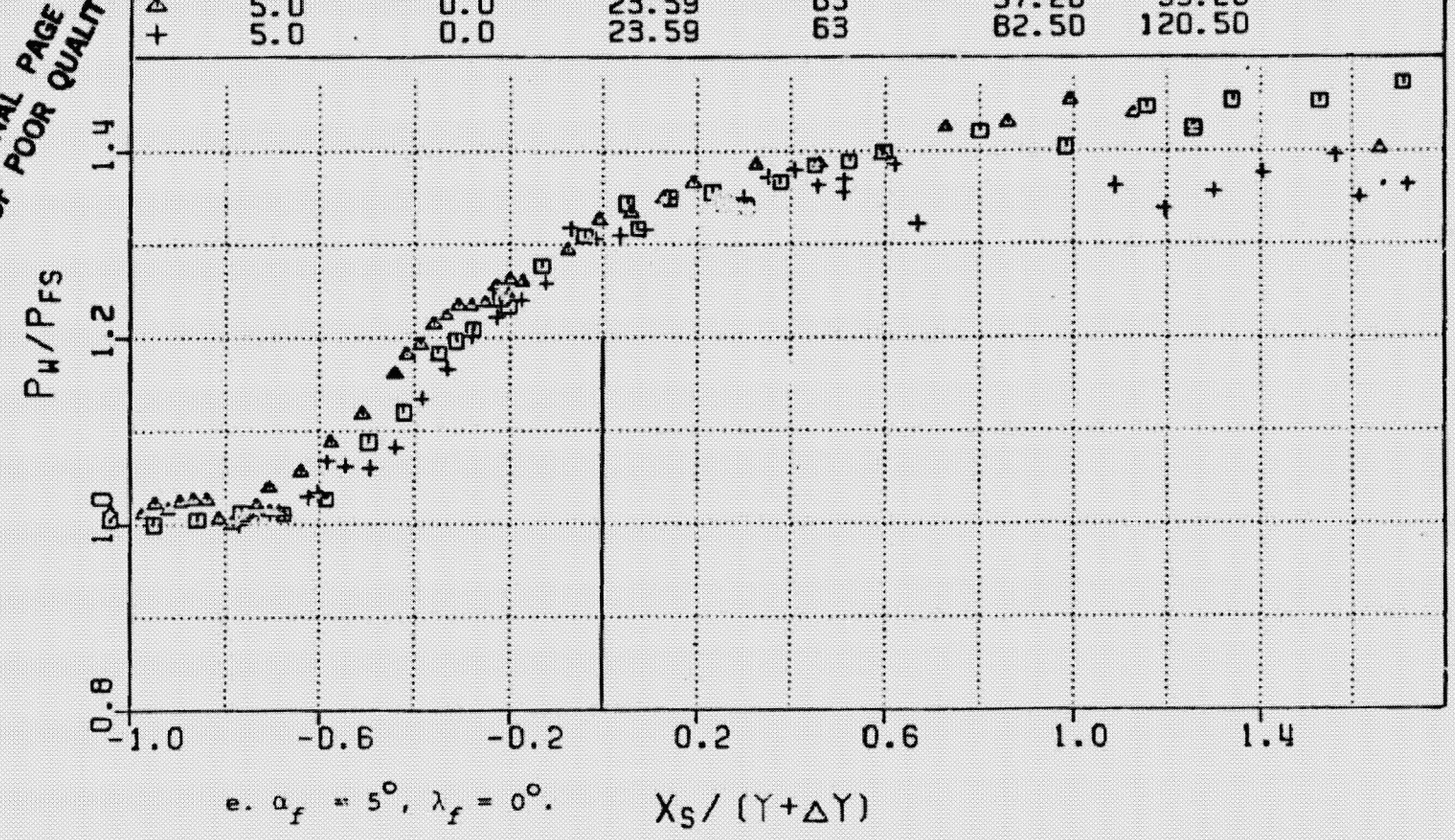

e. $\alpha_f = 5°$, $\lambda_f = 0°$.

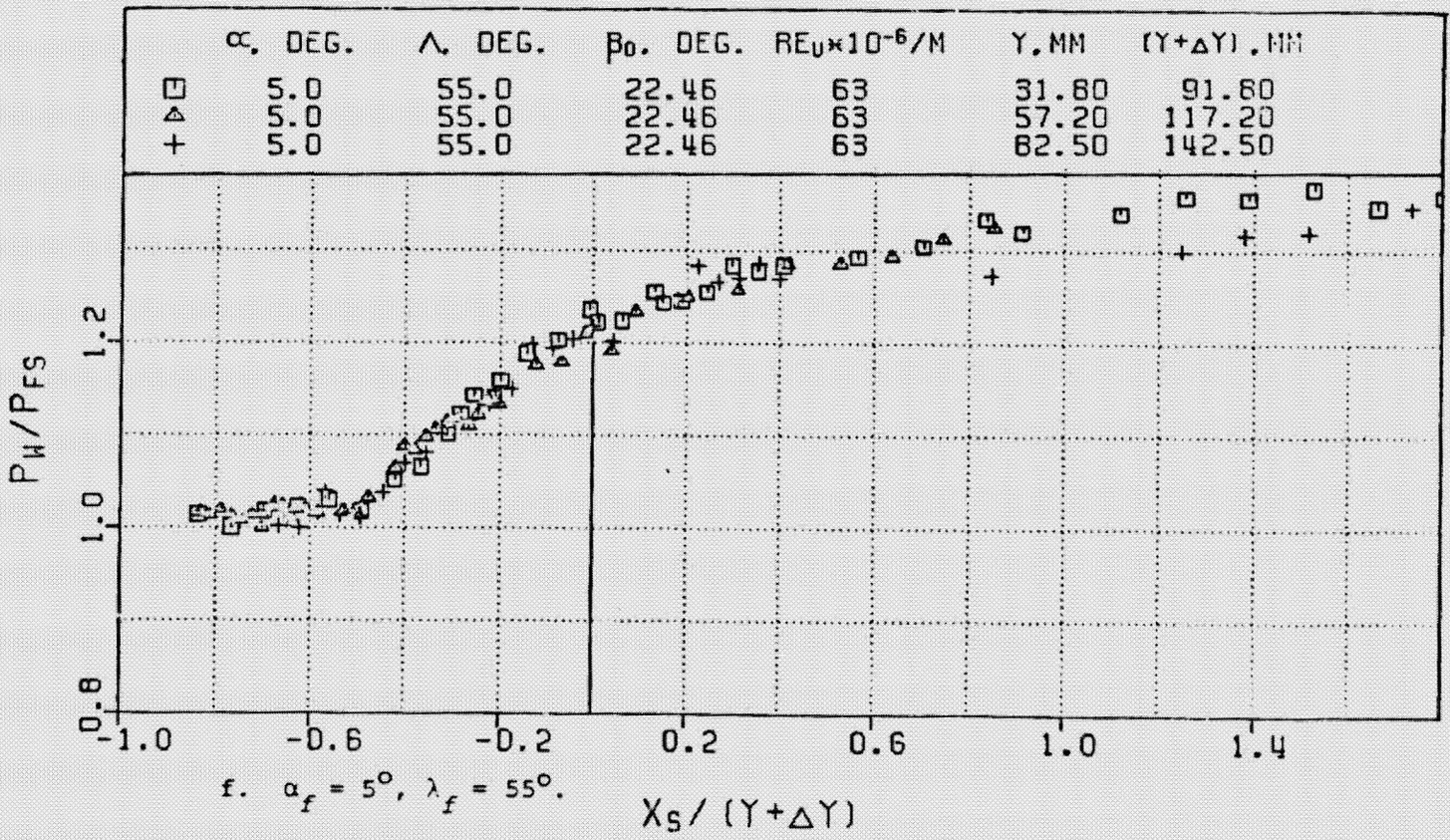

f. $\alpha_f = 5°$, $\lambda_f = 55°$.

Figure 39. (concluded).

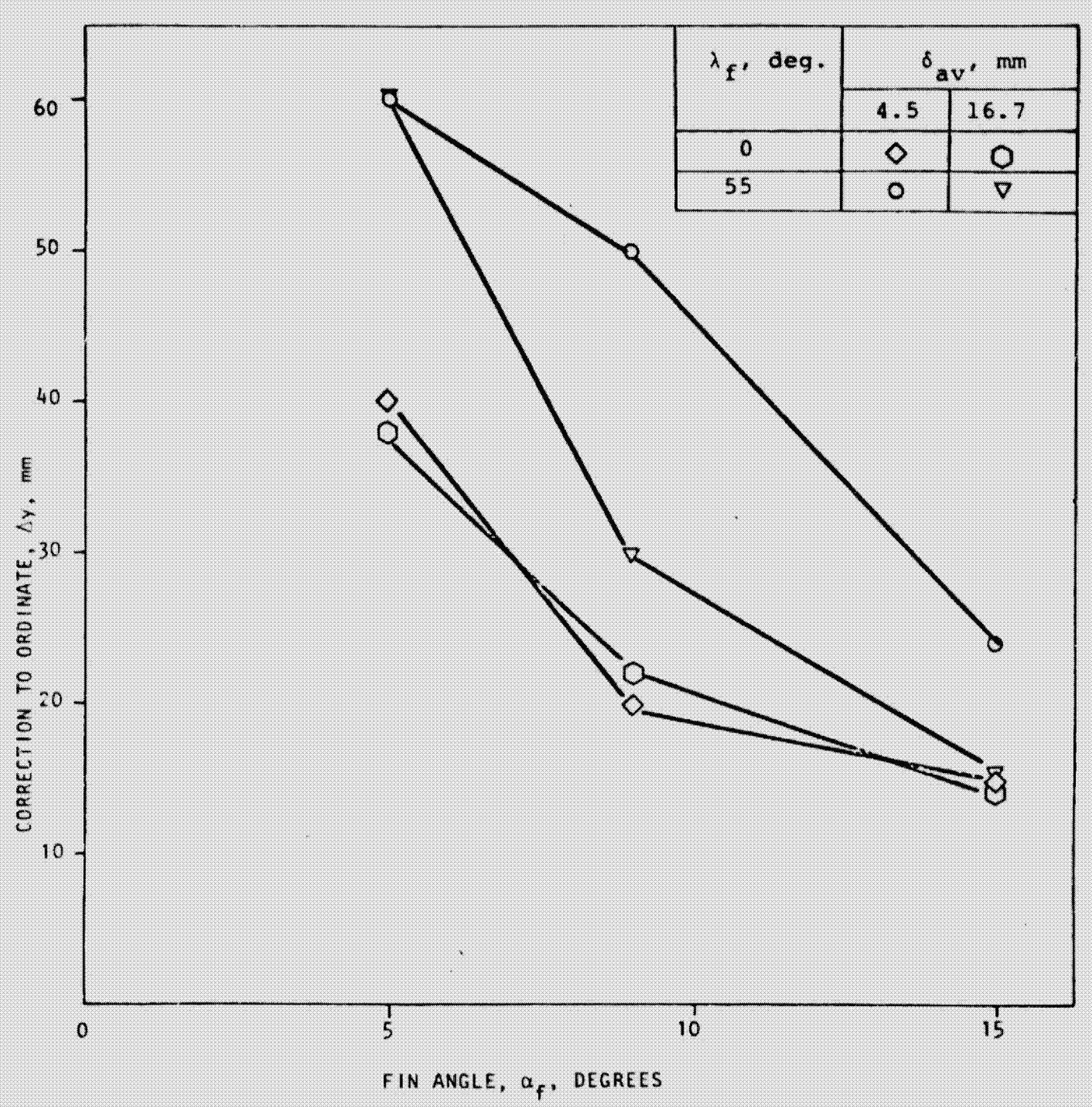

Figure 40. The correction to the spanwise distance for conical behavior of the lampblack streak angle and the surface static pressure distribution.

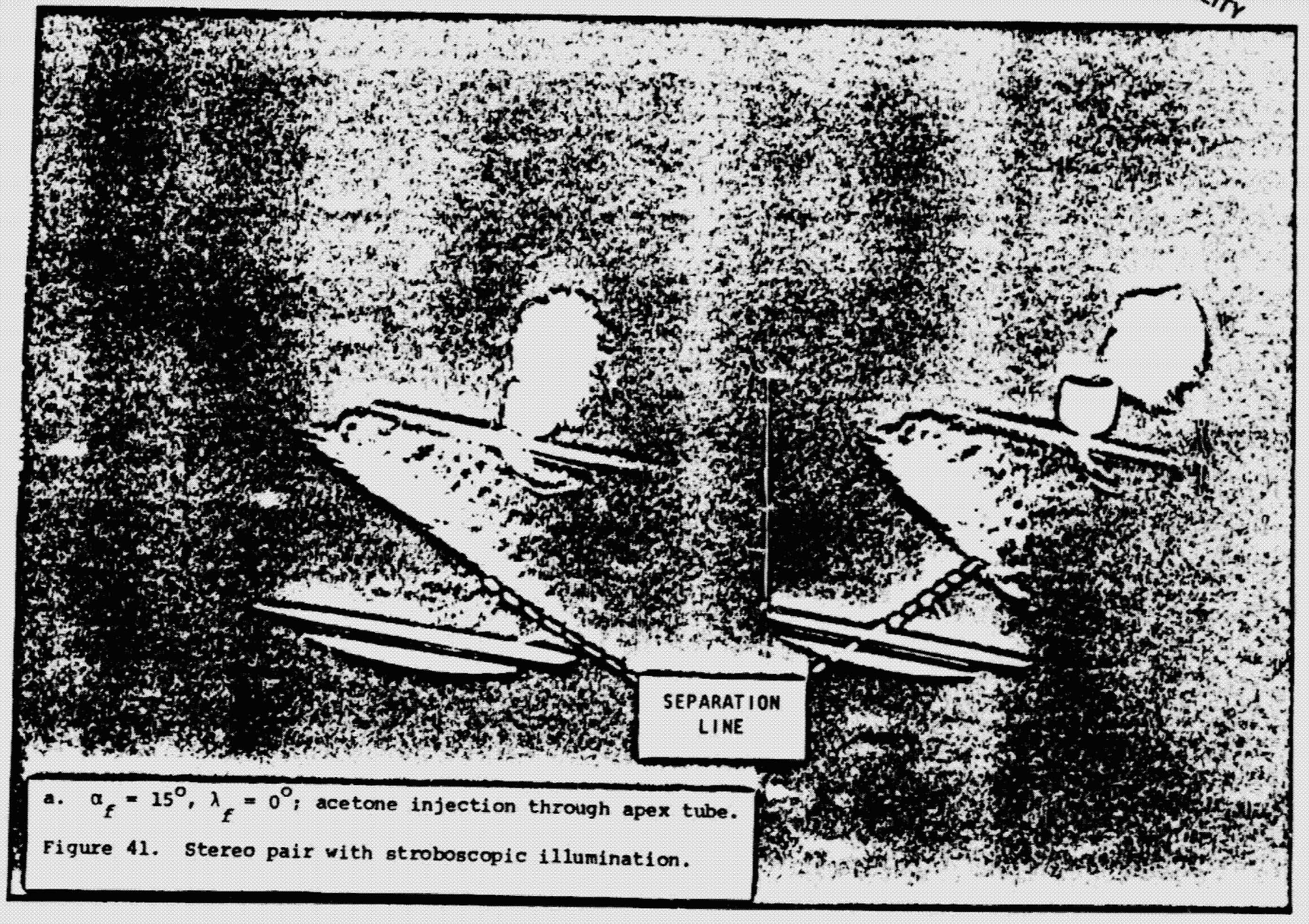

a. $\alpha_f = 15^o$, $\lambda_f = 0^o$; acetone injection through apex tube.

Figure 41. Stereo pair with stroboscopic illumination.

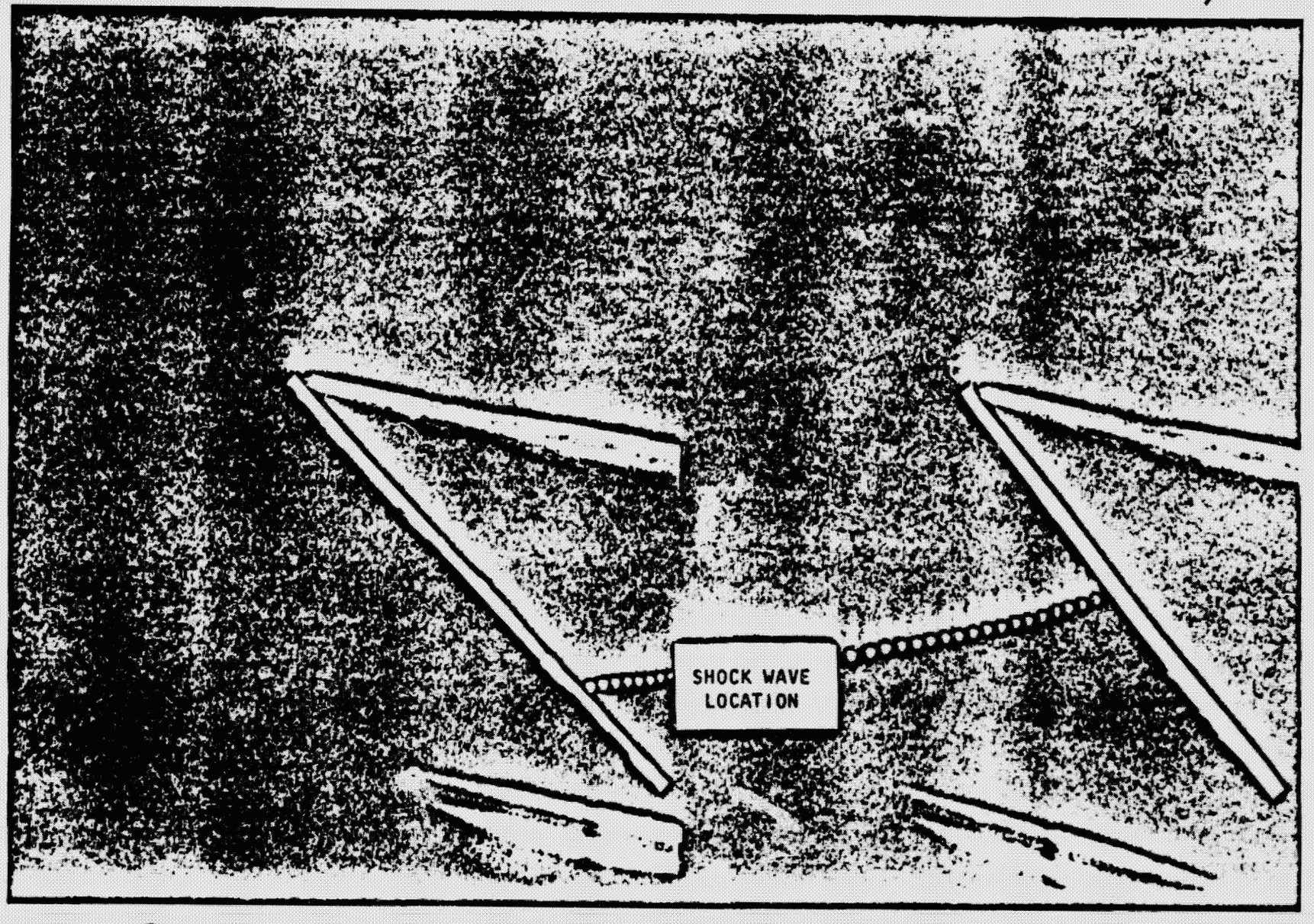

b. $\alpha_f = 5^o$, $\lambda_f = 0^o$; acetone injection through apex tube.

Figure 41. (continued).

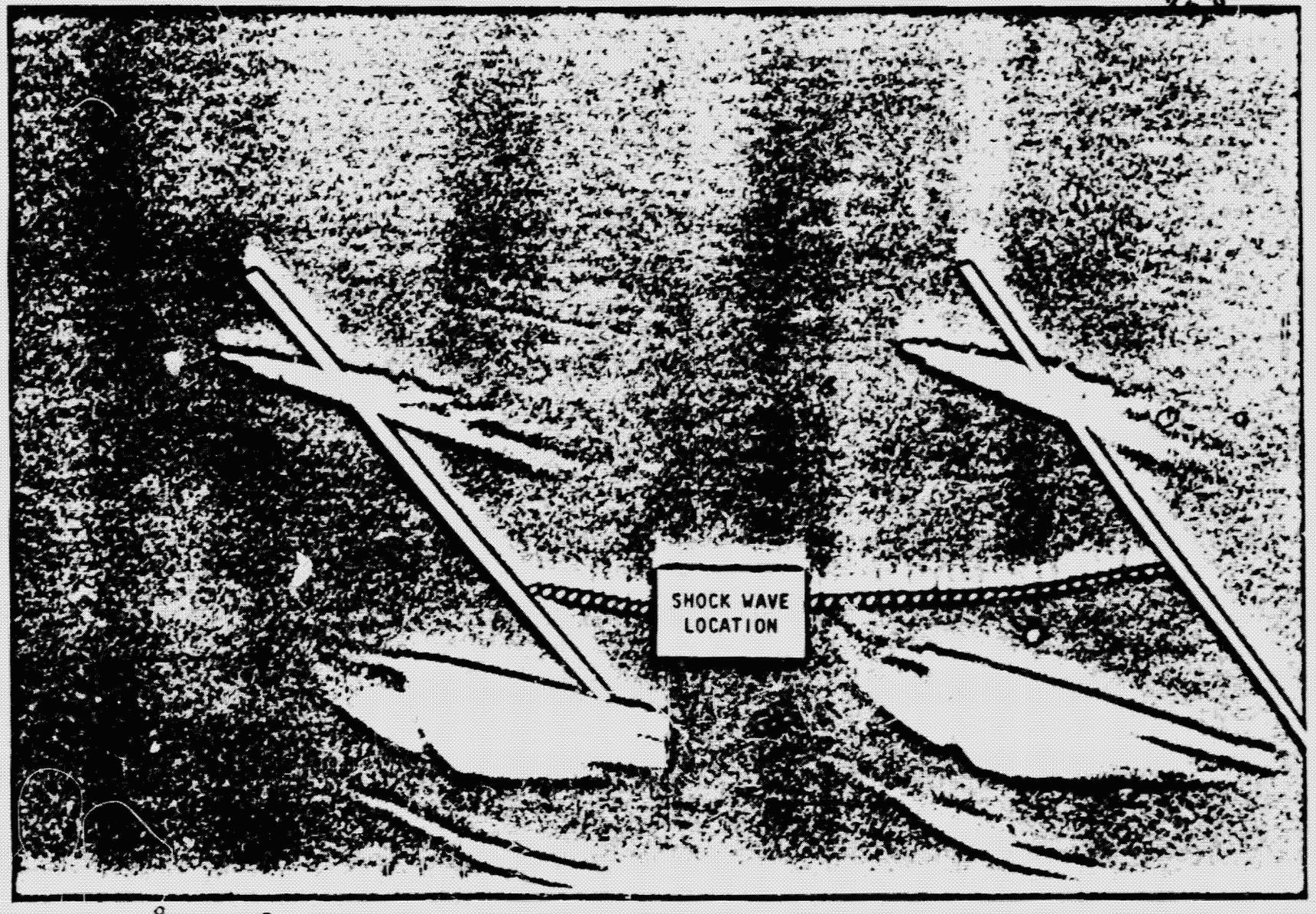

c. $\alpha_f = 5^\circ$, $\lambda_f = 0^\circ$; acetone injection through an upstream orifice.

Figure 41. (concluded).

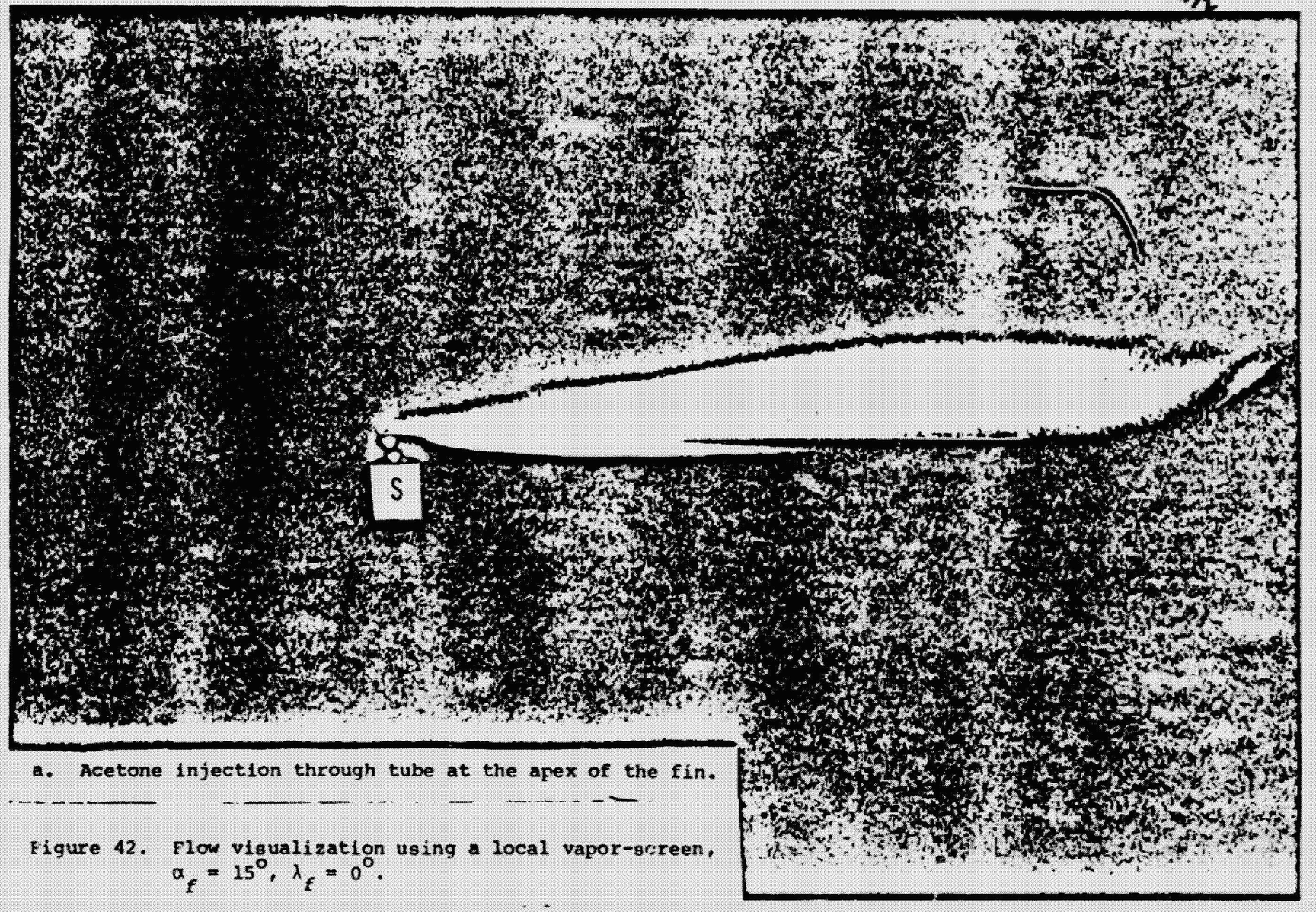

a. Acetone injection through tube at the apex of the fin.

Figure 42. Flow visualization using a local vapor-screen, $\alpha_f = 15^o$, $\lambda_f = 0^o$.

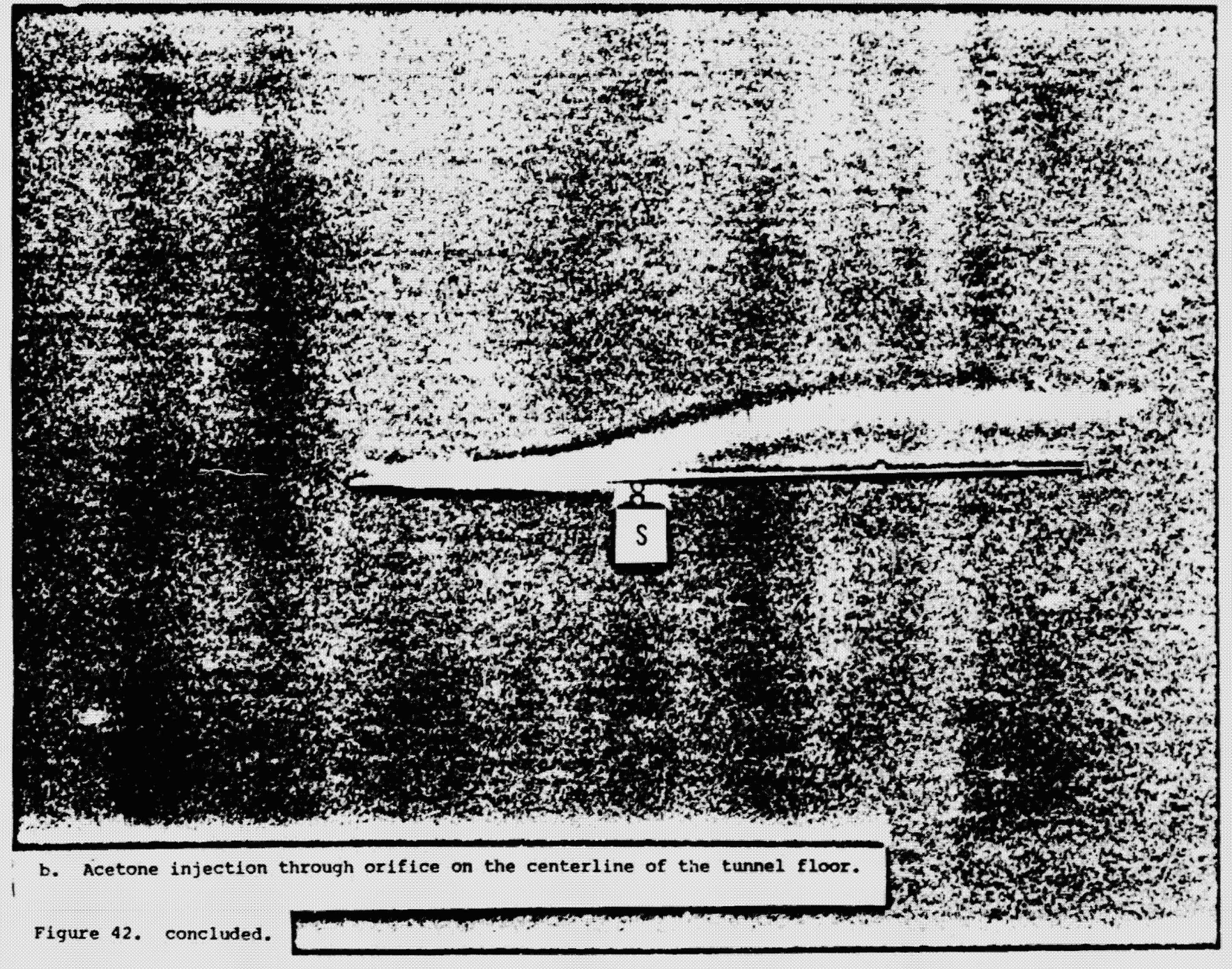

b. Acetone injection through orifice on the centerline of the tunnel floor.

Figure 42. concluded.

Figure 43. Flow visualization using a local vapor-screen, $\alpha_f = 9^\circ$, $\lambda_f = 0^\circ$.

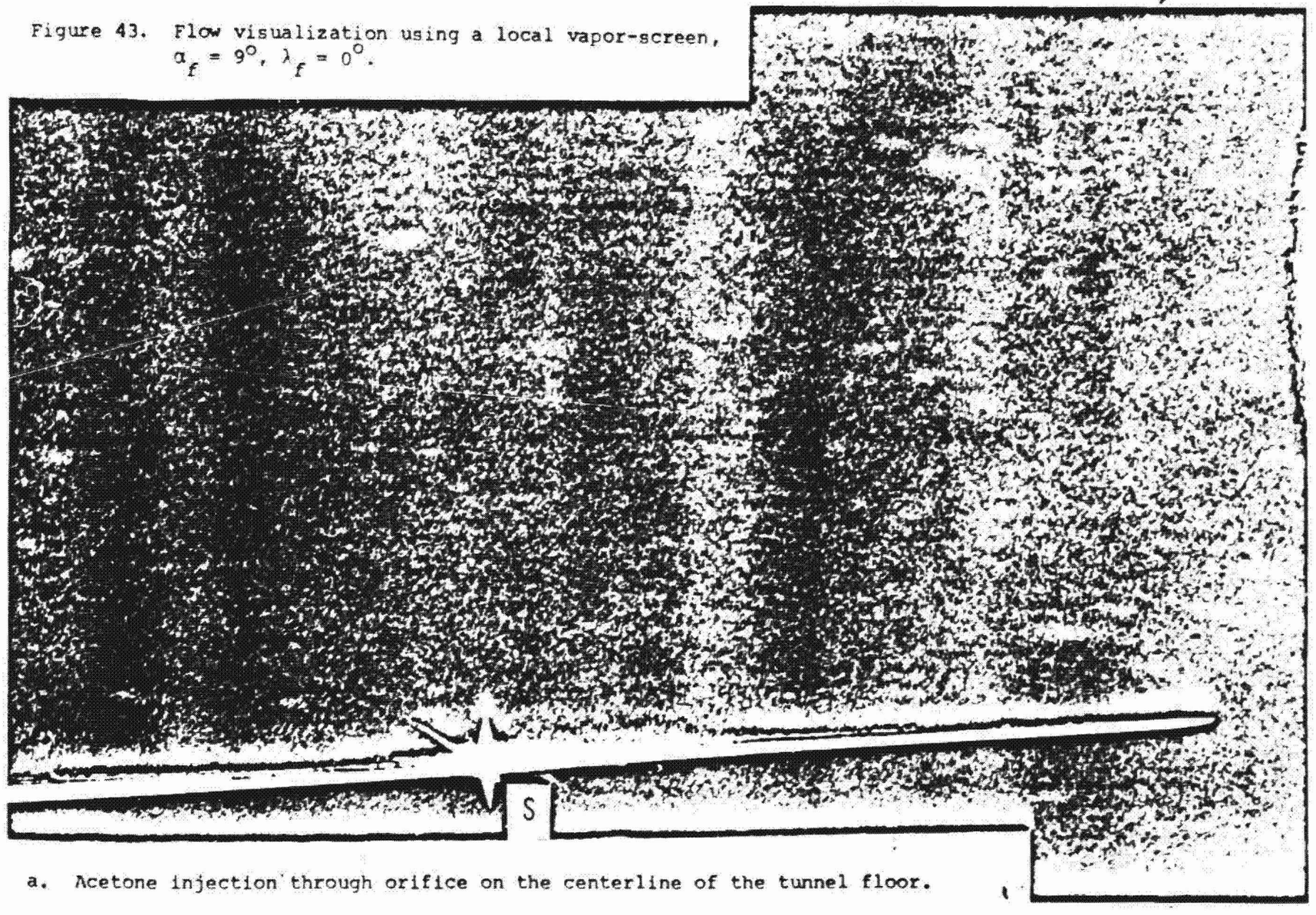

a. Acetone injection through orifice on the centerline of the tunnel floor.

Figure 43. concluded.

b. Acetone injection through tube at the apex of the fin.

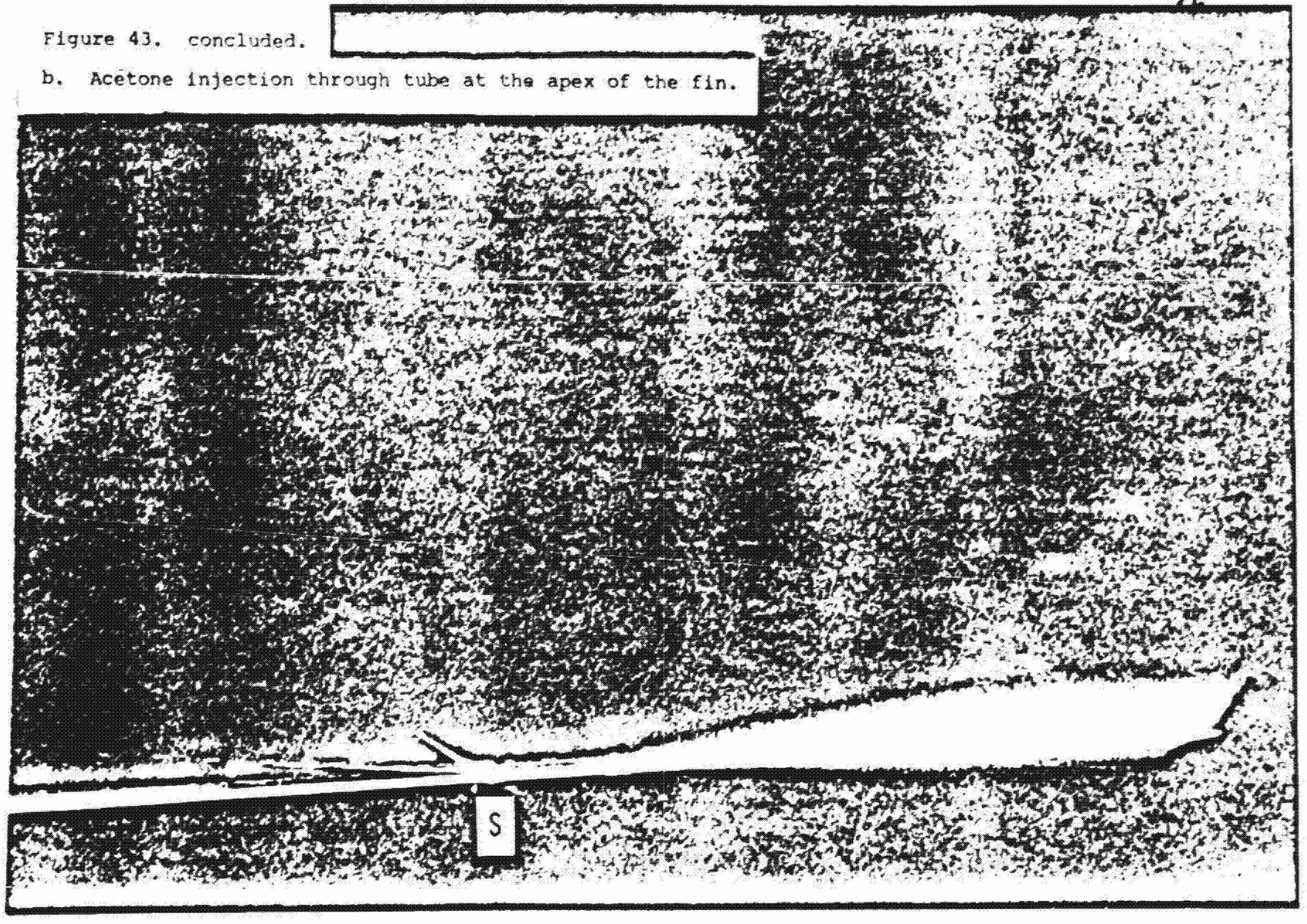

Figure 44. Flow visualization using a local vapor-screen; acetone injection through an upstream orifice, $\alpha_f = 5^o$, $\lambda_f = 0^o$.

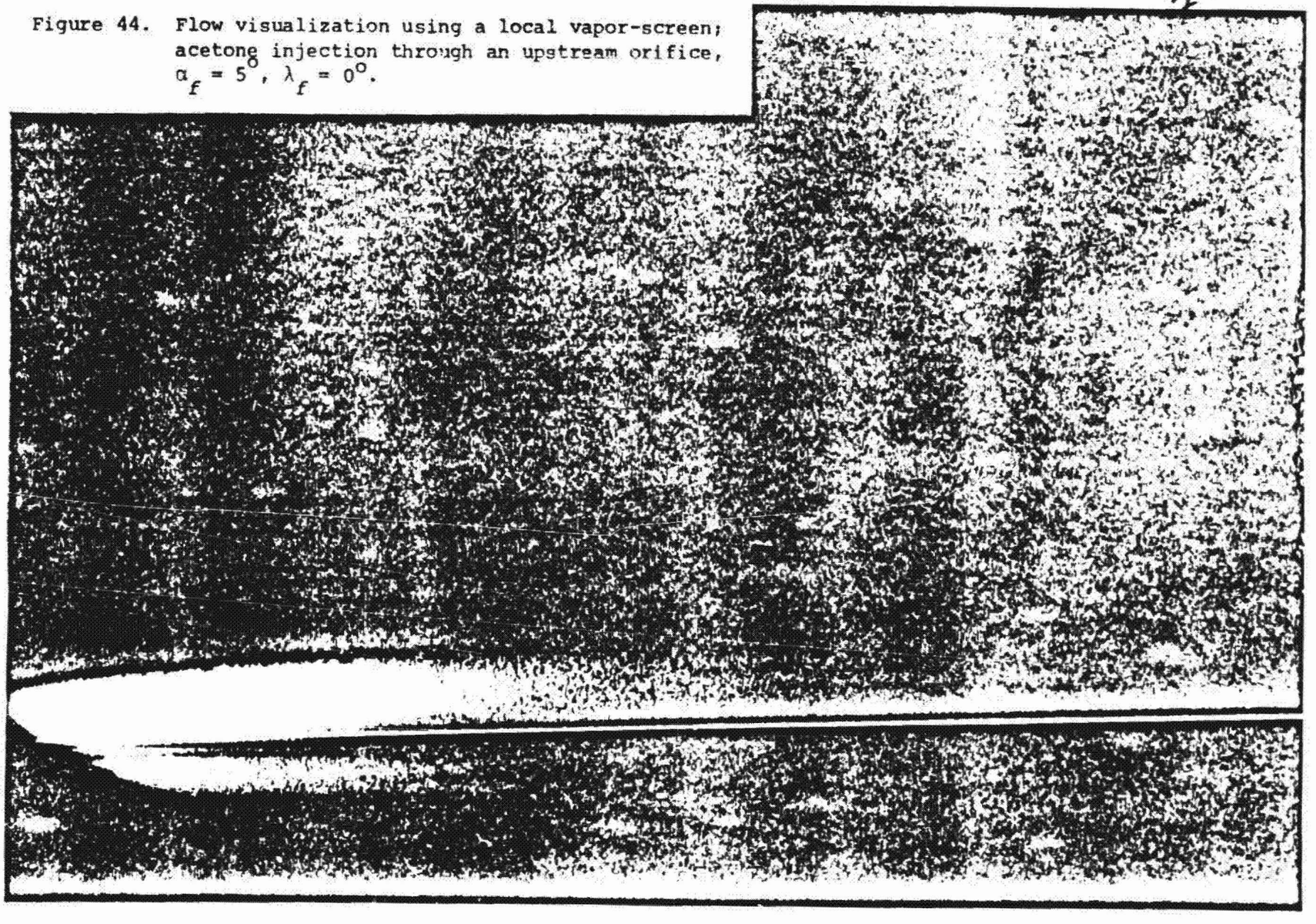

Figure 45. Flow visualization using a local vapor-screen, $\alpha_f = 9^o$, $\lambda_f = 55^o$.

a. Acetone injection through tube at the apex of the fin.

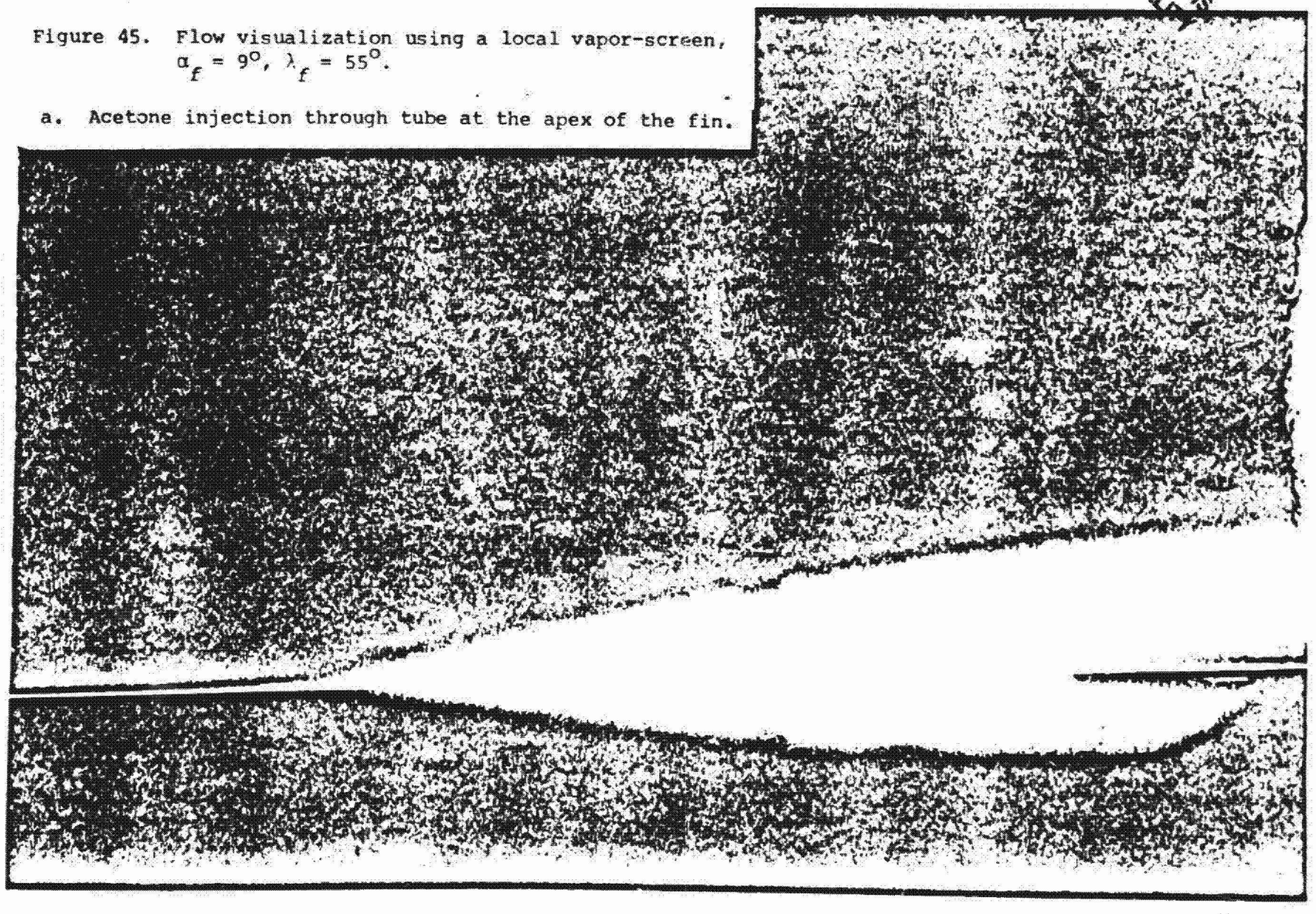

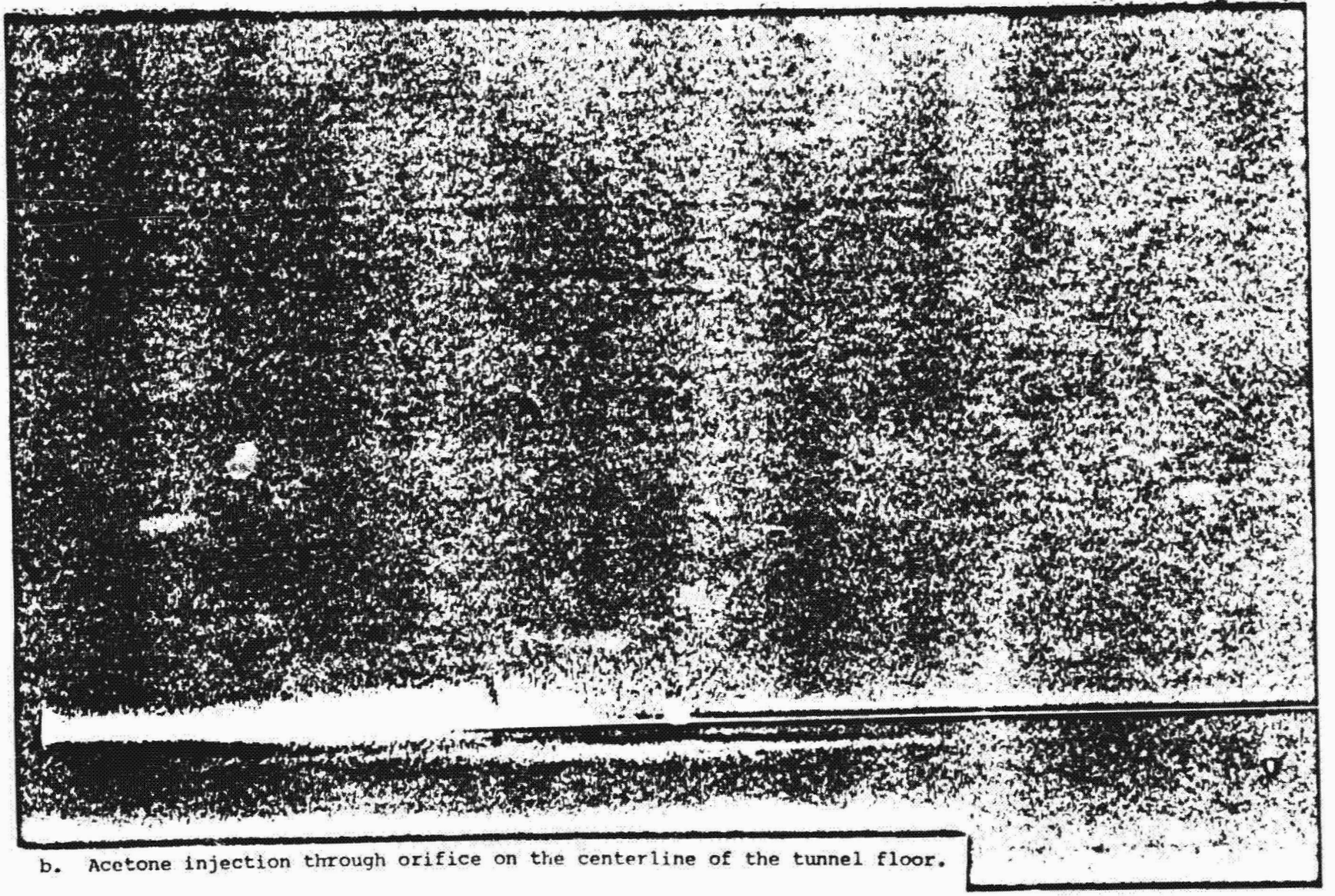

b. Acetone injection through orifice on the centerline of the tunnel floor.

Figure 45. concluded.

Figure 46. Flow visualization using a local vapor-screen, $\alpha_f = 9^{\circ}$, $\lambda_f = 30^{\circ}$.

a. Acetone injection through tube at the apex of the fin.

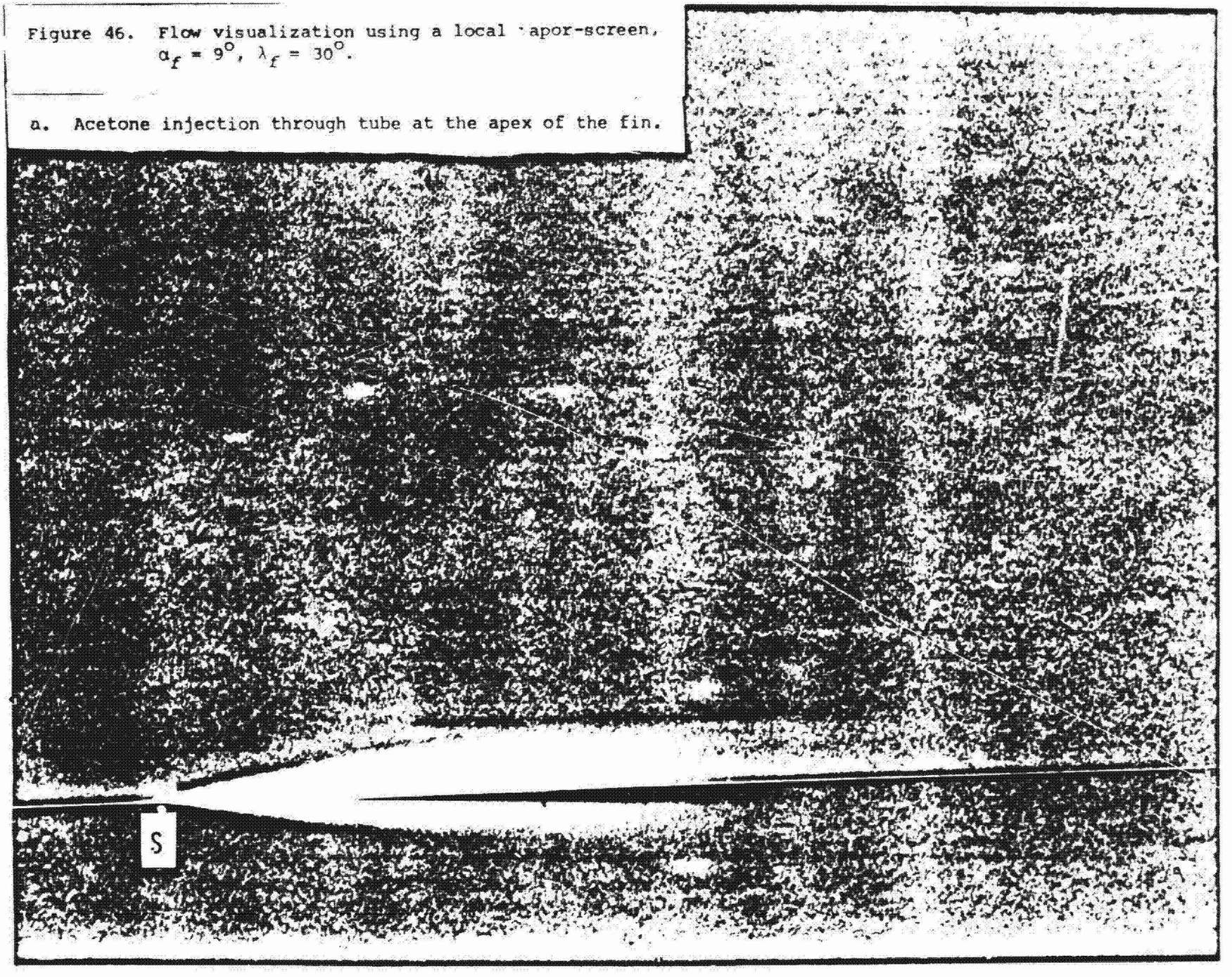

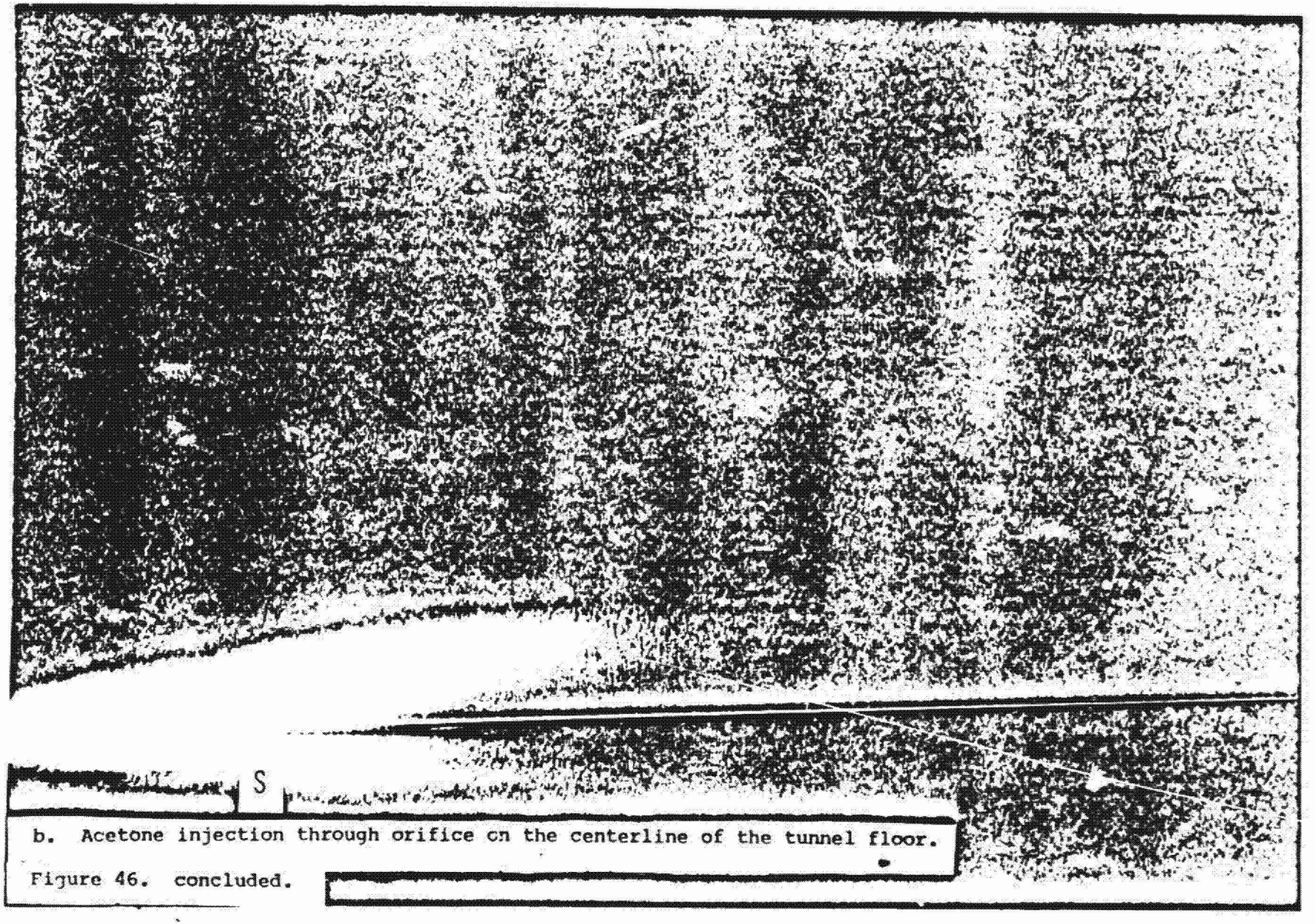

b. Acetone injection through orifice on the centerline of the tunnel floor.

Figure 46. concluded.

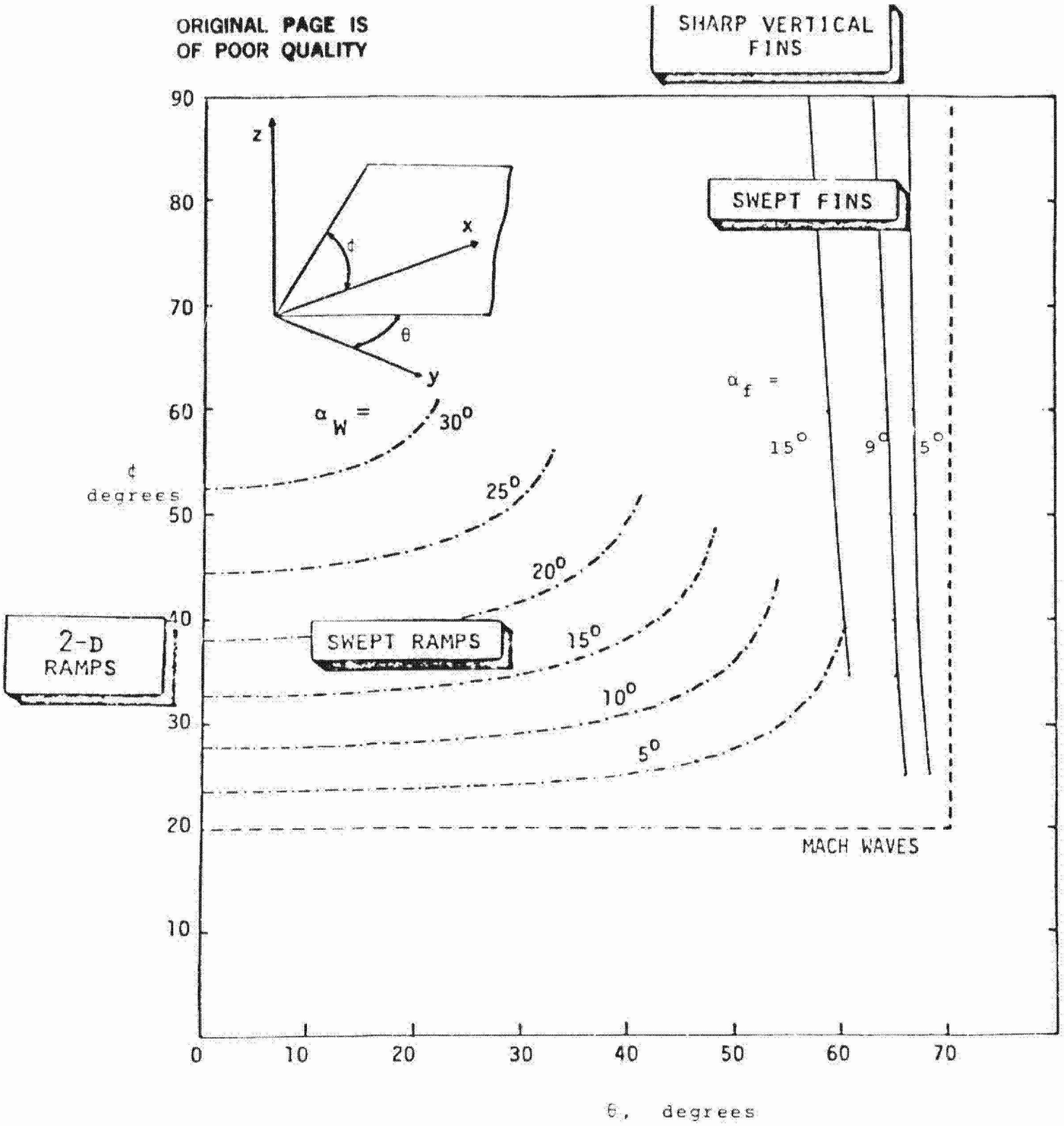

Figure 47. The inviscid shock wave orientation due to sweptback fins and ramps at M_∞ = 2.95.

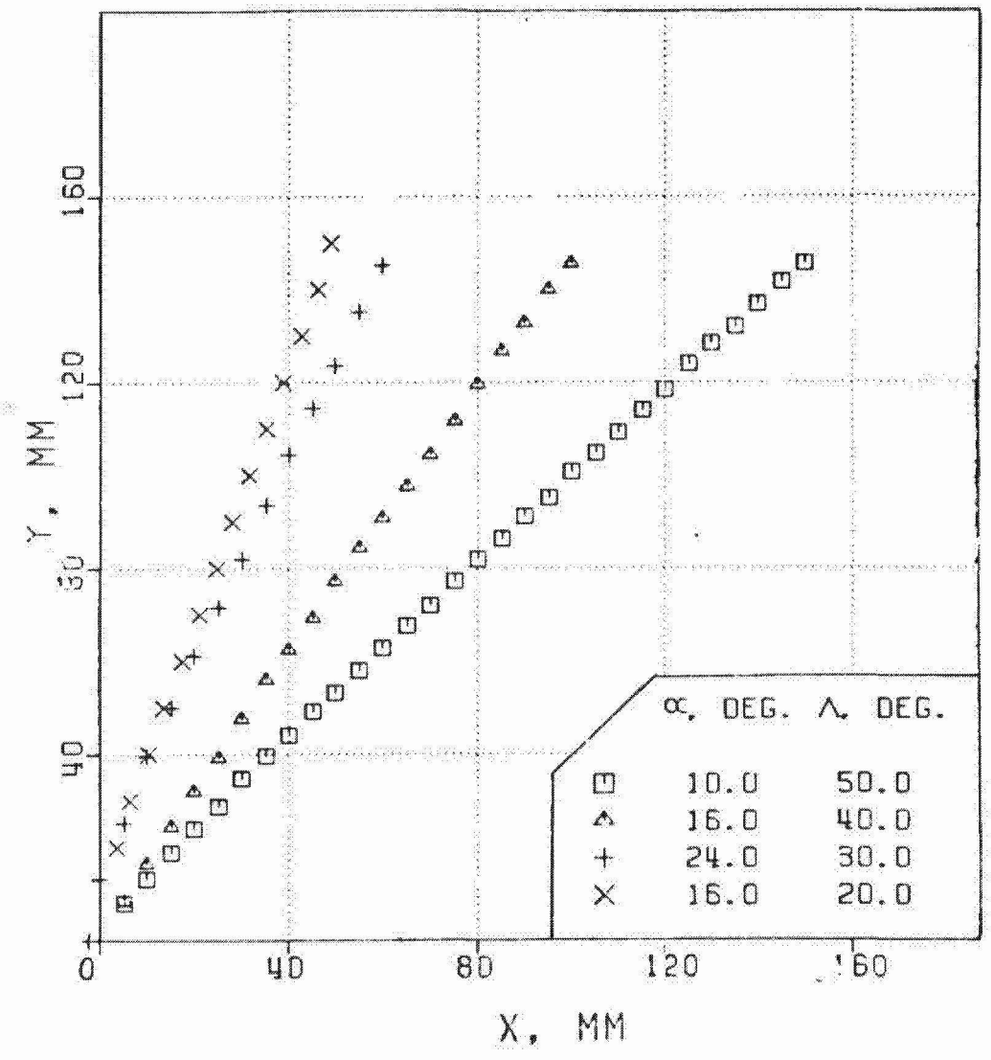

a. Measured data.

Figure 48. The upstream influence due to swept ramps.

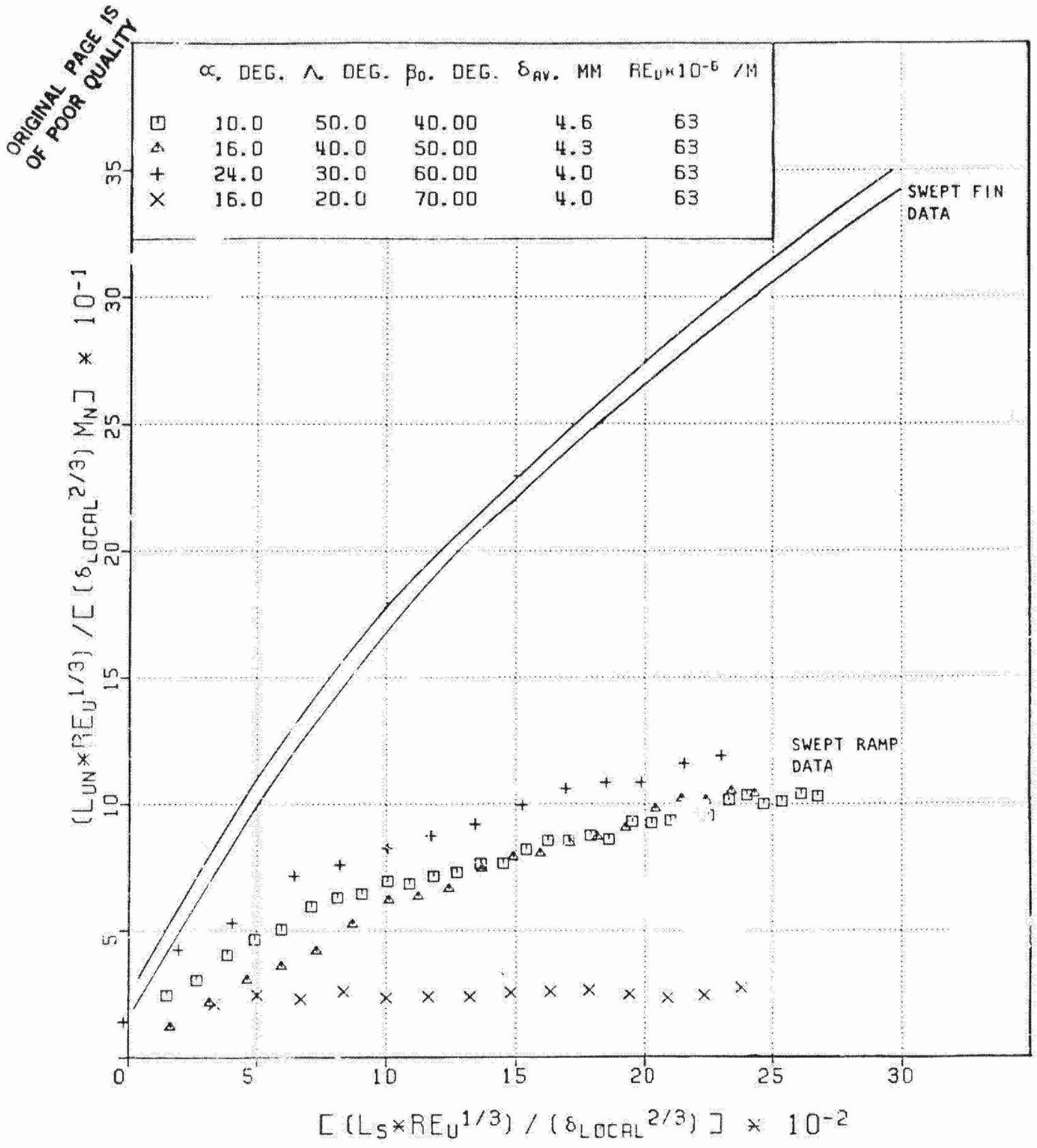

b. Correlation scheme of Dolling and Bogdonoff (1981) for swept fins and swept ramps.

Figure 48. (concluded).